Improved Hall Thruster Plume Simulation by Including Magnetic Field Effects

by

Maria Choi

A dissertation submitted in partial fulfillment
of the requirements for the degree of
Doctor of Philosophy
(Aerospace Engineering)
in The University of Michigan
2016

Doctoral Committee:

Professor Iain D. Boyd, Chair
Professor John E. Foster
Professor Alec D. Gallimore
Richard R. Hofer, Jet Propulsion Laboratory
Professor Mark J. Kushner

And let steadfastness have its full effect, that you may be
perfect and complete, lacking in nothing.
- James 1:4 -

ACKNOWLEDGEMENTS

I owe my gratitude to all those people who have made this dissertation possible and have made my graduate school experience memorable.

First, I would like to express my sincere gratitude to my advisor, Prof. Iain Boyd for his patience, guidance, and encouragement he has provided over the last five years; he helped me learn how to balance work and life and still be efficient, think critically through thought-provoking questions and discussions, and grow as an independent researcher. I cannot imagine a better advisor and mentor for this chapter of my life.

I would like to extend my gratitude to my dissertation committee members: Prof. Mark Kushner, Prof. John Foster, Prof. Alec Gallimore, and Dr. Rich Hofer for taking their time and providing insightful comments to further refine this work.

I also would like to thank all Aerospace Engineering staff members, especially Ms. Denise Phelps for all her help throughout my studies.

I am extremely grateful for the NASA Space Technology Research Fellowship (NSTRF) Program for providing me funds for four years of my graduate school, allowing me to attend conferences and work at several NASA centers to gain invaluable experiences. I would like to acknowledge that without access to use the NASA Advanced Supercomputers' Pleiades cluster and the University of Michigan's NYX and FLUX clusters, I could not have completed this work. Thanks to the Rackham Merit Fellowship for funding my final year of study.

I have been so fortunate to have such great teachers at the University of Michigan. Thanks to all the professors who taught me about aerospace engineering, plasma

physics, and technical writing. I also thank the current and past students of NGPDL, especially Dr. Ken Hara, Dr. Brandon Smith, Horatiu Dragnea, and Astrid Raisanen. Special thanks to Dr. Kelly Stephani and Dr. Yongjun Choi for helping me learn MPIC and making it more readable.

I would like to thank all my friends and colleagues for making my graduate school experience very memorable and fun. Special thanks to Steve Kast and Johann Dahm for being such a good study group for the qualifying exam and helping me learn the FEM. Thanks to the officers of the Graduate Society of Women Engineers for being such a wonderful leadership team to make my graduate career fun and for helping me with the opportunity to actively pursue my passion in STEM outreach. Thanks to Aero Ksag members, especially Dr. Jaeheon Sim and Dr. Eunji Jun who helped me adjust to Ann Arbor during my first year. Thanks to all the members of the Korean Presbyterian Church of Ann Arbor for wonderful fellowship and support.

Finally, I would like to thank my family. My deepest gratitude to my parents, without whom I could not have accomplished anything. Thanks for your boundless love and wisdom that made me who I am today. Thanks to Komo, Komobu, and Grandma for always being supportive and encouraging for whatever I do. Thanks to Sam and Zech for being such good brothers. Most importantly, thanks to my amazing husband; your sacrificial care and love for me made it possible for me to complete this work. Thank you.

TABLE OF CONTENTS

CHAPTER

LIST OF FIGURES

Figure

LIST OF TABLES

Table

CHAPTER I

Introduction

As humankind seeks to reach Mars and beyond, fast travel and affordability are key factors in our pursuit of deep-space exploration, which requires a type of propulsion system. The conventional propulsion system for space travel is chemical propulsion. However, chemical propulsion is limited by temperature of the nozzle, and the molecular mass and chemical specific energy of propellants. Even after the remarkable advances in the last 60 years, the limitations of conventional chemical rockets require high fuel consumption to reach even one of our nearest planetary neighbors—Mars [1]. Alternatively, electric propulsion (EP) technology enables affordable and distant missions by having reduced propellant mass and achieving high exhaust velocity. EP devices use acceleration mechanisms (electrostatic and electromagnetic) that do not rely on the conversion of heat to kinetic energy and can provide high delta-v (Δv). While exhaust velocities of gas jets or chemical rockets are generally 3,000 to 4,000 m/s, electric propulsion devices have exhaust velocities of up to 10^5 m/s for heavy propellants (e.g. xenon) and 10^6 m/s for light propellants (e.g. helium) [2].

Development of EP has been relatively slow due to the long history of chemical propulsion, but there have been EP missions that proved the potential of EP thrusters for future space missions. In 1998, the Jet Propulsion Laboratory (JPL) flew the Deep Space 1 (DS1) spacecraft as the first solar electric propulsion (SEP)-driven deep space mission using the NSTAR (ion) thruster [3]. After the successful demonstration of ion propulsion capability by the DS1 mission, this innovative technology was implemented on the Dawn spacecraft to explore the two heaviest main-belt asteroids: Vesta and Ceres [4]. Dawn is the only spacecraft to ever orbit two destinations beyond Earth and the only to orbit an object in the main asteroid belt between Mars and Jupiter. Dawn's on-going nearly-ten-year journey to gain insights into the beginning of our solar system is made possible only by the implementation of EP.

Among EP devices, Hall-effect thrusters (HETs) can provide the high-specific impulse (I_{sp}) and the high-power propulsion required to enable long-range missions. A HET can produce higher thrust at a given power, requires fewer power supplies, and is a much simpler device than ion thrusters [2]. The actual physical processes occurring in a HET, however, are complex. The detailed physics of plasma processes, such as the anomalous electron transport and the erosion mechanism of a cathode due to impacts of anomalously high-energy ions, are not yet well understood.

Fully understanding the physical processes in the plume of a HET is critical from both the thruster performance perspective and spacecraft integration purposes. Detailed knowledge of electron transport across magnetic field lines will help improve the performance of the thruster. Furthermore, accurate prediction of collision dynamics between propellant neutrals and ions in the plume will help us better understand the interaction between the plume and the host spacecraft, and ensure long life of both the thruster and spacecraft.

In order to better understand and predict fundamental physical processes in a HET plume, it is necessary to develop a reliable numerical model that can capture the collision and plasma dynamics accurately, validated with experimental data. Various numerical models have been used to simulate the partially-ionized plasma in the plume of a HET, which will be reviewed in more detail in Section 1.2. In general, Hall thruster plume simulations do not include the effect of a magnetic field because modeling the magnetic field is complicated due to the cross partial derivative term (i.e., $\frac{\partial}{\partial x}(\frac{\partial}{\partial y})$). Another reason for neglecting magnetic field effects in the plume is that the magnetic field strength in the plume is also relatively weaker than the strength of the field inside or near the exit of the discharge chamber of the HET. However, experiments [5, 6] show that magnetic field lines leak into the plume of HETs. Characterizing the magnetic field effect is thus necessary to examine the assumption of neglecting magnetic field in plume modeling, especially in the near-field plume. Although the magnetic field strength is relatively weak in the plume, its effect needs to be included in order to model the transport of electrons correctly, which is one of the main factors driving the performance of a HET.

This study is concerned with developing an accurate physics-based model to simulate the plume of a Hall thruster using a hybrid particle-fluid approach. As Chapter III will discuss in more detail, the previous model [7] makes a number of assumptions, including neglecting magnetic field effects from the construction of a physical model. In the present study, a new electron model is developed to include the magnetic field and assess its effects on plasma properties. The new model has the ability to simulate any magnetic field shapes, which is important because magnetic field topologies vary from one thruster to another and may change often to improve thruster performance. In addition to the new electron model, a sputter model is implemented to extend the capability of the HET plume simulation. The sputter model can be used to estimate an erosion rate on a solid surface, including the surface of a thruster or any other components of the host satellite. Accurate predictions of the plume characteristics and associated erosion rate are key to successful spacecraft integration from a systems engineering perspective. The new model can predict plasma plume properties that can be used to improve thruster performance and reduce harmful interaction of the plume with a spacecraft.

Section 1.1 of this chapter describes the basic principles on the operation of a

HET and its cathode. The background on Hall thruster plume modeling is reviewed in Section 1.2. The objectives of present study and outline of the dissertation are in Sections 1.3 and 1.4.

1.1 Basic Principles of Hall Thruster Operation

The Hall-effect thruster is an electrostatic device that creates an ion beam to generate thrust by using a cross-field discharge described by the Hall effect. The three main components of a HET consist of an annular anode inside the discharge chamber, an externally- or centrally-mounted cathode, and a magnetic circuit (Fig. 1.1). Electrons in a HET are magnetized, and their gyrating motion around a magnetic field line is described by the gyrofrequency, or cyclotron frequency:

$$\omega_g = \frac{e|B|}{m_e} \tag{1.1}$$

where e is the elementary charge, $|B|$ is the magnetic field strength and m_e is the electron mass. In a HET, the cathode emits electrons to serve two purposes: to ionize the xenon propellant inside the discharge chamber and to neutralize the ion beam downstream of the thruster. Some fraction of the emitted electrons enter the thruster channel due to the positive potential of the anode relative to the cathode. These electrons are confined to the azimuthal drift, or $\mathbf{E} \times \mathbf{B}$ drift, which is generated by the axial electric field, $\mathbf{E}$, and the radial magnetic field, $\mathbf{B}$. These electrons ionize the neutral propellant, typically xenon, that is fed into the annular discharge chamber through the anode. The ionized xenon, mainly Xe^{+} and Xe^{2+}, are then accelerated by the electric field, exiting the thruster as a beam. This ion beam is neutralized as a quasi-neutral plasma by the other fraction of the electrons emitted by the cathode.

Figure 1.2 shows the main parts of the cathode: the insert emitter, the orifice, and the keeper. When the cathode is heated, electrons are emitted from the insert

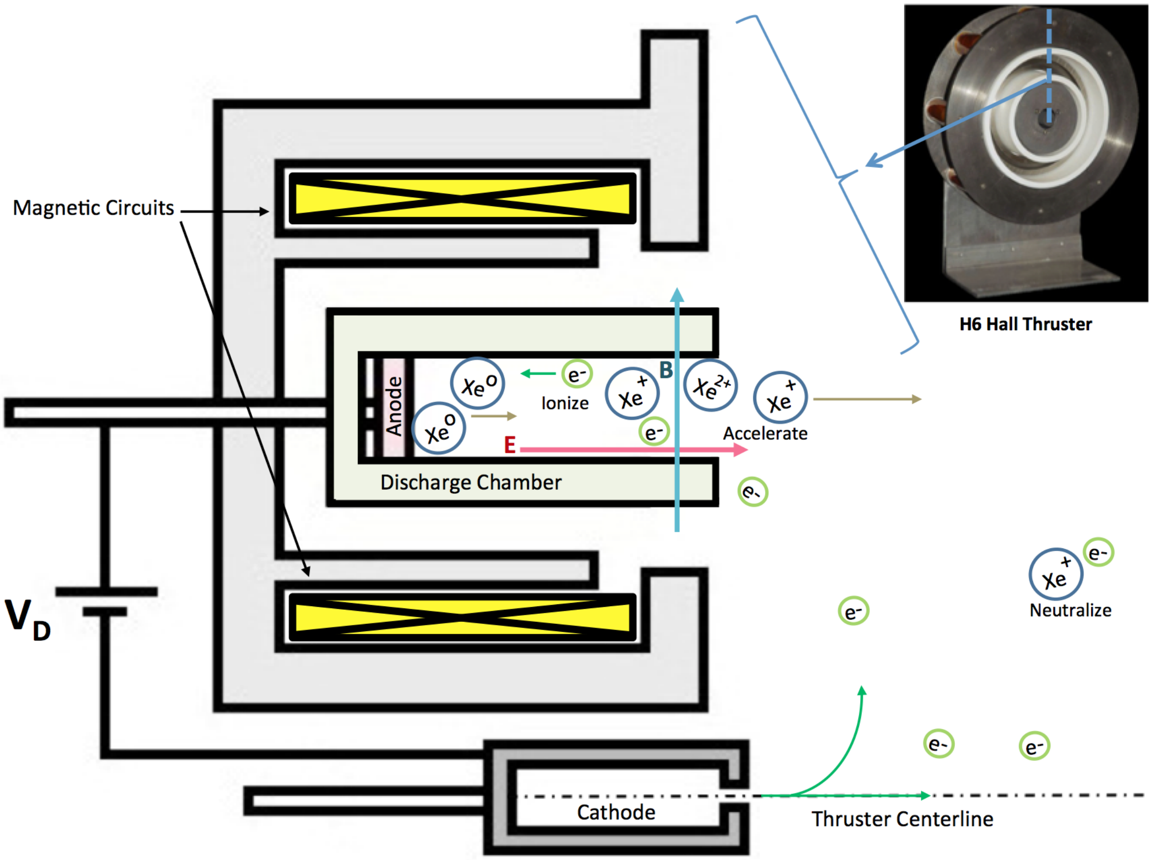

Figure 1.1: Schematic of HET operation with a centrally-mounted cathode. Propellant gas (i.e., Xe) is fed into the anode and undergoes electron-impact ionization inside the discharge chamber. These ions are then accelerated into the plume as a beam. The electrons emitted by the cathode are used to ionize Xe in the discharge chamber and to neutralize the ion beam in the plume.

through thermionic emission. These electrons ionize the neutral gas injected through the cathode tube, flowing from the left side of Fig. 1.2. Ionization produces more electrons, some of which are extracted through the orifice into the plume, where some fraction of electrons move towards the anode and some move along the main beam, neutralizing the flow. In order to protect the cathode orifice from ion bombardment that might limit cathode lifetime, a keeper is used. In addition to the purpose of protecting the cathode, the keeper is used both to start the cathode discharge and to maintain cathode temperature and operation in the event of temporary interruption of the beam current [2]. Therefore, the life of the keeper is very important to the life of the cathode and thruster.

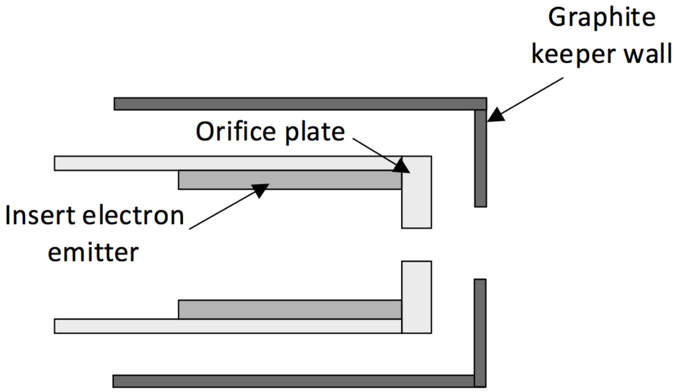

Figure 1.2: Schematic of the main components of cathode: the insert, the orifice, and the keeper.

The Hall thruster used in this study is a 6-kW (H6) laboratory Hall thruster (Fig. 1.3), which was jointly developed between the Air Force Research Laboratory (AFRL), JPL, and the University of Michigan [8]. The H6 Hall thruster has a nominal operating power level of 6-kW, discharge current of 20 A, thrust of 397 mN, and anode specific impulse of 2000 s. The cathode used in the H6 thruster is a central-mounted LaB_6 hollow cathode [9].

1.2 Hall Thruster Plume Modeling

The region where the plasma beam expands outside of the thruster is called the thruster plume. The plume of a Hall thruster contains low-temperature partially-ionized plasma (i.e., neutrals, ions, and electrons) of various energies. Energetic ions in the main beam are the major source of thrust to propel the spacecraft. The accelerating potential for these ions are only a few hundreds volts, so the plume can be significantly broaden [2]. With a typical divergence angle of HETs being approx-

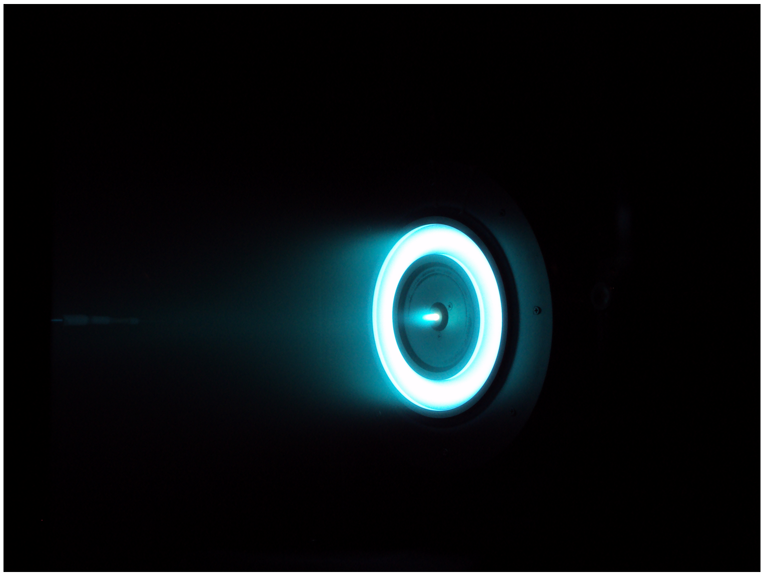

Figure 1.3: The 6-kW (H6) Hall thruster during operation with xenon propellant. Photo taken at JPL by author.

imately 60 deg. from the centerline of the thruster [10], energetic ions in the main ion beam can impinge directly on spacecraft surfaces as backflow, especially if the plume divergence angle is large (Fig. 1.4). These ions can damage and sputter materials from various surfaces of the thruster and spacecraft. Moreover, the sputtered materials can deposit on or contaminate other spacecraft surfaces. In addition to the high-energy ions, the HET plume also contains low-energy ions that are results of charge-exchange collisions, which are important collision mechanisms in a Hall thruster plume. During a charge-exchange collision, an electron is transferred from a fast-moving ion to a slow-moving neutral, resulting in a slow ion and a fast neutral. These charge-exchanged ions have low energy and thus are susceptible to the local electric field. Thus, they can also sputter the thruster and spacecraft, because they can move at large angles with respect to the main beam. Lastly, neutrals—especially the charge-exchanged neutrals—can also sputter the thruster or spacecraft. Because neutrals do not respond to either the electric or magnetic field, their trajectories cannot be changed.

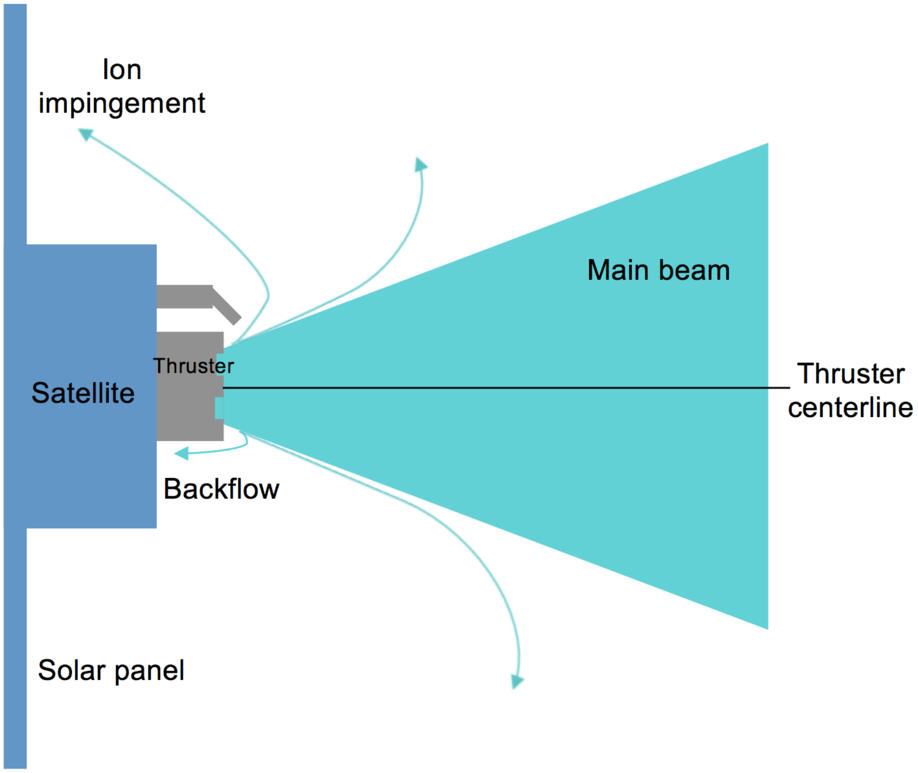

Figure 1.4: Schematic of thruster plume, showing the main plasma beam produced by the thruster and some backflow as a result of large divergence angle and/or charge-exchange phenomena.

Therefore, the detailed collision and plasma dynamics in the plume need to be predicted using an accurate numerical model to reduce any harmful interactions between the plume and the thruster itself or the spacecraft. A numerical simulation can also be performed to predict an erosion rate, or even a lifetime, of the thruster or any spacecraft components. When a particle hits a solid surface, if its energy is greater than the bonding energy of the surface material, then sputtering will occur. Since sputtering can reduce the lifetime of the thruster and spacecraft, the ability to model sputtering phenomena and to estimate the erosion rate is critical in a Hall thruster plume modeling. The sputter model implemented in the present study is described in Chapter V.

The flow in a HET plume is characterized as a rarefied flow, in which plasma and collision length scales are similar to or even larger than the size of the thruster [11]. Such flow requires a kinetic-based description of the system to accurately capture the physics. While the full kinetic description provides accurate results, electrons are usually simulated as a fluid for the following reason. The kinetic simulation of electrons requires significantly high computational effort to resolve the electron timescale because the magnitude of the electron thermal velocity is much greater than that of the ions. More details on choosing the appropriate type of model are discussed in Chapter II.

A popular approach used in Hall thruster modeling is a hybrid particle-fluid approach, in which heavy species (i.e., neutrals and ions) are simulated as particles and electrons are simulated as a fluid. A hybrid model can accurately capture the bulk plasma phenomena and ion kinetics with reasonable computational time. Early work by Oh [12, 5], and followed by many others [13, 14, 15, 16, 17, 7], employed the direct simulation Monte Carlo (DSMC) method [18] coupled with the particle-in-cell (PIC) method [19] for heavy species simulation. The DSMC method emulates the nonlinear Boltzmann equation by simulating the intermolecular collisions determined from the kinetic theory of a dilute gas, as will be discussed in greater detail in Section 2.1.3. While these hybrid methods employ similar approaches for the heavy species model, the main difference among them is in the choice of electron model [7]. There are various fluid electron models, ranging from the simple Boltzmann relation to more sophisticated fluid models based on conservation laws. Refs. [13, 14, 15, 17] use the simple Boltzmann relation, while Refs. [16, 7] use more detailed electron models based on mass, momentum, and energy conservation laws.

The hybrid model used in this study, MPIC [16], also uses the DSMC-PIC method for heavy species and has two different types of electron models: 1) the Boltzmann relation and 2) the detailed electron model that solves electron mass, momentum, and energy conservation equations to determine electron velocity, plasma potential, and electron temperature, respectively. In MPIC, three conservation equations are solved by using a single finite element solver for a Poisson equation (i.e., $\nabla\cdot(\sigma\nabla\phi) = f(x, y)$) by calculating the source terms ($f(x, y)$) in advance using another method. During this process, some assumptions are made that may affect the accuracy of the solution (see Section 2.2.3). In order to improve the physical and numerical accuracy of the electron model, a new finite element model is developed in this study. More details on the motivation for developing the new electron model is discussed in Section 3.1.

It is very difficult for a single hybrid code to accurately resolve physical processes of partially-ionized plasma in all regions of a Hall thruster, i.e., from the anode and the cathode into the far-field plume. The length scales and flow physics occurring in these regions are very different, and resolving the smallest scales will require significant computational time. Therefore, plume simulations typically start from the exit plane of the thruster, requiring plasma characterizations at the exits of the discharge channel and the cathode. Since the plume structure strongly depends on the plasma conditions and magnetic field configuration at the exit plane of the discharge channel, it is important to get as accurate a condition as possible. These conditions can be obtained from experiments or simulations. While having experimental measurements offers accurate properties for some parameters, not all necessary input parameters can be measured, and the spatial resolution of the measurement may be limited. Thus, an internal plasma simulation can be performed to model the plasmas in the discharge chamber and can be coupled to the plume model at the thruster exit boundary. Coupling together two codes is an approach that has been used before and was reviewed by Huismann [7].

In the work prior to the current study, Huismann used the state-of-the-art hybrid code HPHall to simulate plasmas in the discharge chamber and to provide the plasma conditions at the thruster exit plane as an inlet boundary condition to MPIC. HPHall was originally developed by Fife [20] and has been improved by others [21, 22, 7] over many years. HPHall is an axisymmetric model designed to simulate plasmas internal to Hall thrusters using a structured grid. The computational domain of a HPHall simulation is shown in Fig. 1.5. HPHall simulates the discharge plasma from the discharge chamber up to the very near-field plume of the thruster. In HPHall, the collision dynamics between heavy species are modeled using the Monte Carlo collision (MCC) method, the transport of ions are modeled using the PIC method, and the electrons are modeled using a quasi 1-D fluid method. The magnetic field effect is included in the model.

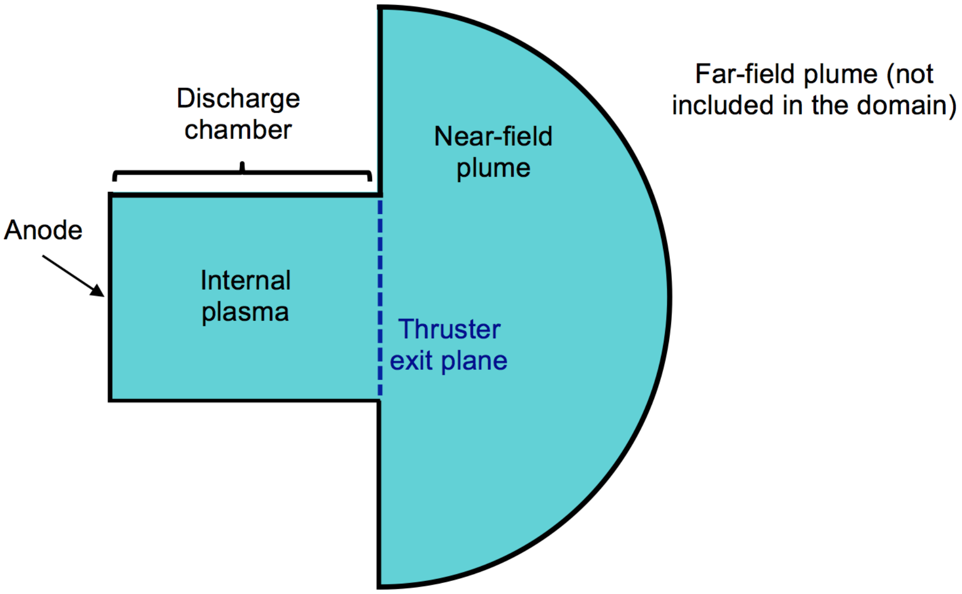

Figure 1.5: Schematic of the computational domain of HPHall, indicating the anode, the discharge chamber, internal and near-field plume plasmas, and the thruster exit plane where plasma conditions are extracted to be used as an inlet boundary condition in MPIC plume simulation.

While discharge plasma conditions at the thruster exit are provided by coupling with HPHall, the previous study by Huismann made strong assumptions about the makeup of the cathode mass flow. It was assumed that the only heavy particles injected at the cathode inflow were xenon neutrals, because there were no data available on the ion properties at the cathode outside of current density measurements. How-

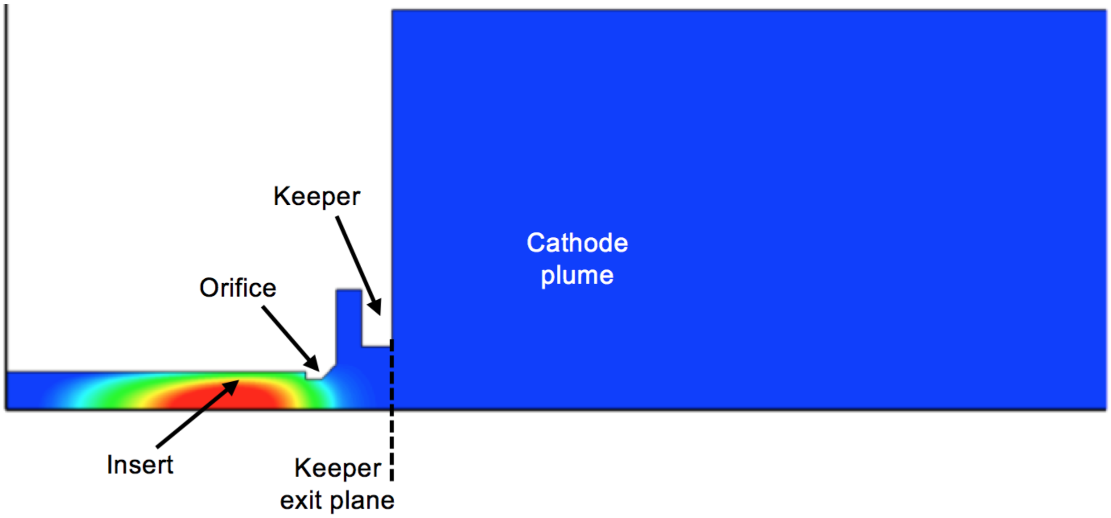

Figure 1.6: Computational domain of OrCa2D [23]. Shown are the insert, orifice, keeper, and plume regions. The keeper exit plane shown is the inlet for the current plume model domain.

ever, xenon ions clearly exist in the cathode plume [7, 2], and thus should be included in the model. In the current model, full plasma (i.e., ions and electrons) and neutral conditions are incorporated at the exit plane of the cathode keeper as an inflow condition. These conditions were extracted from results provided by a global hollow cathode code, OrCa2D developed at the Jet Propulsion Laboratory [23]. OrCa2D is a fluid model, where ions and neutrals are also modeled as fluids by solving conservation laws. Figure 1.6 shows the computational domain of OrCa2D with a contour plot of the electron density. The computational domain includes the insert, the orifice, the keeper, and the plume regions.

1.3 Objective of Research

This study has four overall objectives: 1) develop an accurate physics-based model to simulate a HET plume, 2) improve the accuracy of the plume simulation by refining cathode condition, 3) assess the accuracy of the model through comparison with available experimental data, and 4) extend the capability of the plume simulation by implementing a sputter model. Of these four, the most important objective is to improve the accuracy of the Hall thruster plume modeling.

The accuracy of plume modeling is improved mainly in two ways. First, accurate physical and numerical models for the fluid electrons are developed by including magnetic field effects. The magnetic field is neglected in the prior models, however it may play an important role in the plume, especially in the near-field plume. Including the magnetic field effect will result in a more physically accurate model and require modeling of the anomalous electron transport in the plume of a Hall thruster. Because the new model is derived from a 3-D cylindrical coordinate system without loss of generality, the model can simulate any and all complex magnetic field topologies. The new electron model is also numerically more accurate and robust than the prior model by directly applying the continuous Galerkin finite element method to the governing equation. Moreover, the electron transport coefficient tensor formed by including the magnetic field effect is easily integrated by using the quadrature rule.

The second way to improve the plume model is to apply more accurate boundary conditions at the boundaries of the discharge channel and the cathode. As demonstrated by previous studies using MPIC for Hall thruster plume simulations [24, 7], the boundary conditions at the discharge channel have a significant impact on the plume structure. By coupling the current plume model with internal Hall thruster and cathode plasma models, we can generate accurate boundary conditions and thus obtain more accurate plume simulation results. In the present study, two internal plasma codes are used to link the discharge plasma to the plume model: 1) a state-of-the-art Hall thruster model HPHall to provide inflow conditions at the discharge channel and 2) a global hollow cathode model OrCa2D to provide more accurate cathode boundary conditions.

Once the plume simulation has been performed using the new electron model and boundary conditions, the model has to be validated. An assessment of the accuracy of the new models is performed through direct comparisons between simulation results and experimental data. During this process, an electron mobility modeling is performed by adjusting the anomalous electron mobility coefficient (α) to study its effect on the plume structure.

Understanding the detailed dynamics of the plume is important to predict its interaction with a spacecraft. The final objective of the present study is to add the capability to simulate sputtering phenomena on solid surfaces. Including sputtering phenomena is essential in plume modeling from a spacecraft integration perspective. In this study, the sputtering model is applied to simulate sputtering process and to estimate the steady-state erosion rate of the cathode keeper.

1.4 Thesis Outline

The remaining chapters of the dissertation are described in this section. Chapter II reviews the background of numerical methods and governing equations used in this study. Hybrid particle-fluid approaches are discussed to simulate the HET plume—a transitional flow. Chapter III describes the prior modeling effort using MPIC and the motivation to develop a new, improved electron model. The new physical and numerical models for the electron momentum equation are reviewed in detail. The new model is verified by using the method of manufactured solutions and by comparing it with another electron model using a mock Hall thruster case simulation. Chapter IV first presents the comparison of the new model with the prior model when the magnetic field effect is neglected. Then, the new model with the magnetic field is compared to the new model without the magnetic field to study the magnetic field effects in the plume. Lastly, the validation of the new model is performed by comparing against experimental measurements. Chapter V reviews a sputtering model that is implemented in MPIC. It investigates incoming species energy and flux distributions, and estimates the steady-state erosion rate. Finally, Chapter VI summarizes the findings of the present work and makes recommendations for future work.

CHAPTER II

Numerical Methods and Governing Equations

The plume of a Hall thruster consists of low-temperature, partially-ionized gas including neutral, ion, and electron species. Each species has different transport physics due to their different masses and charges. For instance, since electrons and ions have charges, their motions are governed by electric and magnetic fields, while neutrals do not respond to these fields. Moreover, electrons move much faster than the heavy species (i.e., neutrals and ions) because electrons have much lighter mass. Thus, the nature of physics for each species determines the type of numerical approach used in a simulation. In general, there are three approaches to simulate plasma flows in a Hall thruster: 1) a fluid approach by solving conservation laws, 2) a kinetic or particle approach to track the evolution of the particles, and 3) a hybrid method where the fluid approach is used for electrons, and the particle approach is used for the heavy species.

The current study uses a 2-D axisymmetric hybrid particle-fluid model known as MPIC, or MONACO-PIC, which was first developed by Cai [16] at the University of Michigan, and has been used by many others [25, 7, 26] to simulate a non-equilibrium or rarefied flow, such as a plume of a Hall thruster. In MPIC, the transport of neutrals and the collision dynamics of heavy species are modeled using the direct simulation Monte Carlo method [18]. The transport of ions is modeled using the particle-in-cell method [19], which includes the effects of electrostatic fields. The electrons are modeled using a continuum approximation by solving fluid conservation equations. This chapter describes the detailed physical and numerical models that are used to simulate the heavy species and electrons.

2.1 Transport of Heavy Species based on Particle Approach

The gas in the plume of a Hall thruster is defined as a rarefied gas, where the continuum assumption breaks down and, instead, a molecular description of the system is necessary to accurately capture the physics. Modeling rarefied gas using a particle method tracks the motion of individual molecules, or particles, using discrete Eulerian grid points in space. The first part of this section provides background information on rarefied gas dynamics, and the second and third parts describe the two particle methods—direct simulation Monte Carlo (DSMC) and particle-in-cell (PIC)—for modeling heavy species. The next part of this section summarizes the major steps for a hybrid particle method, i.e., DSMC-PIC, and the last part describes boundary conditions for this method. In this thesis, the conventional use of the word molecule in this field is used as a generic term that includes monatomic and diatomic molecules consisting of a single atom and two atoms, respectively.

2.1.1 Background on Rarefied Gas Dynamics

A system is defined as a rarefied gas based on the mean distance traveled by particles between collisions, known as a mean free path λ_{mfp}, defined as the mean thermal speed $\bar{c}$ of the particle divided by the collision frequency ν_c, i.e., $\lambda_{mfp} = \bar{c}/\nu_c$. When the gas pressure is low, the gas deviates from the equilibrium state and follows the kinetic theory. The degree of rarefaction of a gas can be assessed by calculating the Knudsen number (Kn), which is an important non-dimensional parameter that indicates the validity of continuum approaches, defined as the following:

$$Kn = \frac{\lambda_{mfp}}{L_c} \tag{2.1}$$

where L_c is a characteristic length of the system.

Generally, the gas flow can be categorized using three regimes depending on Kn, which also determines the set of governing equations that need to be used in order to accurately capture the physics of the flow. For $Kn < 0.01$, the continuum flow assumption is valid and thus the Navier-Stokes or magnetohydrodynamic (MHD) equations can be solved. In the continuum flow regime, the velocities of particles are described by a Maxwellian velocity distribution centered at a bulk flow velocity with a variance related to the temperature of the gas. As Kn increases, however, the intermolecular effects start to become insignificant, and particles start deviating from the Maxwellian velocity distribution. For $Kn > 1$, the continuum approximation becomes invalid due to every particle moving independently from each other, and thus the problem has to be modeled using the particle or kinetic approach, i.e., solving the Boltzmann equation, to model particles at the molecular level. This flow regime is called the free-molecular, or collisionless regime. When Kn is in between the continuum and free-molecular regimes ($0.01 < Kn < 1$), the flow is defined as a transitional flow, or a rarefied flow, where the particle or kinetic approach should be used as well.

There are several different types of modeling techniques for simulating rarefied flow at the molecular level depending on what the focus of the modeling is. One approach is a direct kinetic method where the collisionless Boltzmann equation, or the Vlasov equation for charged particles is directly solved by using finite discretization methods [27]. This method is also computationally intensive because the equation is in 7 dimensions, i.e., $(\mathbf{r}, \mathbf{v}, t) = (x, y, z, v_x, v_y, v_z, t)$. Alternative methods to directly solving kinetic equations are the particle-based kinetic methods, or particle methods, that solve the Boltzmann equation using probabilistic techniques. One example of the particle method is a Monte-Carlo technique, which includes Monte-Carlo Collision and direct simulation Monte-Carlo methods, that models intermolecular collisions to track the evolution of macroparticles at each time step. These methods are effective in simulating a neutral flow and a rarefied gas [28]. Another example of a particle method is the particle-in-cell method, which simulates the transport of charged particles by calculating electrostatic or electromagnetic forces acting on the particles.

The flow of the plume of electric propulsion devices for satellites is in the transition regime [29][2]. Thus, heavy species are usually simulated using a hybrid particle method—the DSMC method coupled with the PIC method, i.e., DSMC-PIC. Generally, the DSMC method is effective in simulating dilute neutral gas flow while the PIC method is effective in simulating dilute flows with charges and electric and magnetic field effects, i.e., plasma [16]. Both the DSMC and PIC methods use a macroparticle that represents a large number of real particles to simulate gases at the microscopic level. More details of the PIC and DSMC methods are explained in Sections 2.1.2 and 2.1.3, respectively.

2.1.2 Particle-In-Cell Method for Particle Transport

The particle-in-cell (PIC) method is a particle-based kinetic method that tracks the motions of charged particles continuously in a Lagrangian frame using Eulerian grids [30]. In the current simulation, only ions are modeled using the PIC method. The force acting on charged particles is described by the Lorentz force:

$$\mathbf{F} = q\left(\mathbf{E} + \mathbf{v} \times \mathbf{B}\right) \tag{2.2}$$

where q is the elementary charge, $\mathbf{E}$ is the electric field, $\mathbf{v}$ is the velocity, and $\mathbf{B}$ is the magnetic field. In a Hall thruster, the magnetic field is not strong enough to magnetize ions. Neglecting the magnetic field effect, the motion of each ion is governed by Newton's second law:

$$\begin{aligned} \frac{d\mathbf{x}}{dt} &= \mathbf{v} \\ \frac{d\mathbf{v}}{dt} &= \frac{q}{m}\mathbf{E} \end{aligned} \tag{2.3}$$

In the PIC method, as the name suggests, the charge density (ρ) at each grid point is calculated from the distribution of particles in each cell. From this charge density, we can calculate the electric potential (ϕ) by solving the Poisson equation $\nabla^2\phi = -\rho/\epsilon_0$, where $\rho = q(n_i - n_e)$ and ϵ_0 is the vacuum permittivity. In this study, however, quasi-neutrality ($n_i \approx n_e$) is assumed, and an electron fluid momentum conservation equation is solved to calculate the electric potential on each node. By differentiating the electric potential, the electric field $\mathbf{E}_j = (E_x, E_y)_j$ is computed at each node j. To calculate the derivatives of the potentials on nodes, a least-squares method is used [16]. In this method, if the current node j has N nodes connected with potential gradients $d\phi_i/d\mathbf{x}_i$, then the N nodes form $N \times 2$ relations which are overdetermined using the following:

$$\underline{M}\mathbf{E} = d\phi \tag{2.4}$$

where $\underline{M}$ is an $N \times 2$ matrix, E is a 2×1 vector, and $d\phi$ is an $N \times 1$ vector. By multiplying this equation by a transposed matrix $\underline{M}^T$ on both sides, this overdetermined matrix becomes a 2×2 matrix that can be solved. More details can be found in Ref. [16].

After the electric field is calculated, it is then converted into electrostatic force, which accelerates on particles as in Eq. (2.3). Finally, the velocities and positions of the particles are calculated at each time step using the electric field at the particle position by integrating Eq. (2.3). Once particles are moved using their trajectories, collisions between particles are performed using the DSMC algorithm, which may adjust their trajectories again if determined to collide (see Section 2.1.3).

The PIC method requires a weighting scheme to compute charge and neutral densities on discrete spatial grids from particle positions. The same weighting scheme is also used to interpolate the electric field from the grids to particles. One method to accurately calculate the charge density on a grid point j is to sum all particle charges inside a volume or cell V_j enclosing the grid, and then divide the sum by the total volume or area surrounding the grid point, as in the following:

$$n_j = \left(\sum_{j=0}^{N} N_j \right) / \left(\sum_{j=0}^{N} V_j \right) = \left(\sum_{j=0}^{N} N_j \right) / V_k \tag{2.5}$$

where V_k is the corrected cell-centered volume that is the sum of volumes of all cells surrounding the node. To calculate V_k, we need to use the reference coordinates, as shown in Ref. [31]. However, this type of weighting scheme requires much cross-node transportation on a parallel machine, which would be quite inefficient [16]. While various other weighting schemes are discussed in Ref. [16], the weighting scheme for the charge and neutral allocations adopted in this study is a simple and accurate one described as follows. After the cell-average values are calculated, they are averaged onto the nodes in each processor. The charge density n on a node in one computer processor, where N cells are connected to the node, is calculated as in the following:

$$n = \left(\sum_{j=0}^{N} n_j \right) / N \tag{2.6}$$

where the j^{th} cell has an average charge density n_j. This scheme does not require a complete list of cell-average values for all cells physically connected to a node, but only the cells in the same computer processor. Therefore, this weighting scheme is efficient on a parallel machine without significant loss of accuracy.

Additionally, in order to reduce statistical scatter in the density-weighting calculations, MPIC uses a relaxation technique in ion and neutral number densities on each node:

$$n_{new} = w n_{allocate} + (1 - w) n_{old} \tag{2.7}$$

where w is a weighting factor, n_{new} is the current ion or neutral number density, $n_{allocate}$ is the density obtained from MPIC's cell-averaged weighting function, n_{old} is the density from the previous time step, and a value of $w = 0.1$ is employed in the current work. This treatment is effective at suppressing statistical scatter in steady-state flow simulations [16].

2.1.3 Direct Simulation Monte-Carlo Method for Collision Dynamics

When particles collide, they do not physically touch each other, however their force fields interact with each other. When modeling these intermolecular collisions, however, the calculation of force-fields of every collision pair is almost impossible due to the extremely large number of collisions that occur at almost all times in a rarefied gas. Therefore, instead of solving the actual intermolecular forces, we use a probabilistic method that computes collision probability from collision cross-sections and molecular diameters. Such probabilistic methods include the Monte Carlo Collisions (MCC) method and the direct simulation Monte Carlo (DSMC) method. The current study uses the DSMC method because it conserves both the momentum and energy, while the MCC method does not conserve energy. The DSMC method can directly simulate particles at the molecular-level instead of solving fluid conservation equations. In the DSMC method, the intermolecular collision in a rarefied gas is modeled as a binary collision, where one particle collides with only one other particle, because the mean molecular spacing is larger than the effective molecular diameter [18].

A number of different types of collisions can occur between particles in an ionized gas, such as elastic (e.g., momentum-exchange), inelastic (e.g., excitation and ionization), superelastic, radiative, and charge-reactive (e.g., charge-exchange). In the case of electric propulsion and plasma processing applications, the most important collisions that must be considered in modeling are the elastic momentum-exchange (MEX) and charge-exchange (CEX) collisions. Collision mechanisms implemented in the current model are the MEX collision between neutral-neutral and neutral-ion pairs, and the CEX collision between neutral-ion pairs.

During a CEX collision between a slow-moving neutral and fast-moving ion, an electron is transferred from a slow neutral to a high-energy ion, exchanging a charge. Since the CEX interaction is a long-range reaction, the post-collision velocities and trajectories of the colliding particles are assumed not to be affected by the collision. Charge-exchange collision is an important mechanism in Hall thruster plumes because at the thruster exit plane, the atoms and ions have velocities that differ by almost two orders of magnitude as a result of CEX collisions [15].

The DSMC method simulates collisions between macroparticles, each of which represents a large number of real particles. The ratio between the real number of particles and the macroparticles is defined as W_{ref}. In the DSMC module, a list of colliding particle pairs in each cell is selected at random, regardless of their relative positions and velocities, to perform binary collisions. Since checking for collision pairs between all particles would be inefficient (about $N^2/2$ pairs), Bird's No-Time-Counter (NTC) scheme [18] is used to calculate the total number of possible collision candidate pairs in each cell for each time step $\triangle t$:

$$N_{total\,pairs} = \frac{1}{2} N_p \bar{N}_p (\sigma g)_{max} \triangle t \tag{2.8}$$

where N_p is the instantaneous number of macroparticles, $\bar{N}_p$ is a time or ensemble averaged number density in each cell, g is the relative velocity between colliding particles, and σ is the total cross-section. Whether these candidate pairs actually undergo collisions depends on the collision probability of each pair. The collision probability of each candidate pair is calculated at each time step, and is proportional to the product of the relative velocity between the colliding particles and the total cross-section. The collision candidate pair will undergo a collision if the collision probability is greater than a random number, R, which is uniformly distributed in [0,1):

$$\frac{\sigma g}{(\sigma g)_{max}} > R \tag{2.9}$$

The simplest cross section model is the hard-sphere approximation, where the total collision cross-section is:

$$\sigma_{HS} = \pi d^2 \tag{2.10}$$

where d is the effective molecular diameter. While the hard-sphere approximation is simple, it is not realistic and is independent of the relative translational energy $E_t = 1/2\, m_r g^2$ where m_r is the reduced mass. In most cases, the effective cross-section of real molecules decreases as E_t increases [32]. In 1981, Bird [32] introduced the variable hard sphere (VHS) model, in which the cross section can vary with the relative speed of the two colliding particles, g, as the following:

$$\frac{\sigma}{\sigma_r} = \frac{g^{-2\omega}}{\overline{g}_r^{-2\omega}} \tag{2.11}$$

where σ_r is the reference cross-section ($\sigma_r = \pi d_r^2$), $\overline{g}_r$ is the relative collision velocity at the reference temperature T_r, and ω is the viscosity temperature exponent ranging from 0 to 0.5 with 0 being a hard-sphere model. Assuming $T_r = 273K$, ω and d_r values can be found for several major species in Ref. [18].

The collision dynamics modeled in the current DSMC method include MEX collisions between neutral atoms (Xe-Xe) and both MEX and CEX collisions between the neutral and ion (Xe^+-Xe and Xe^{2+}-Xe). The collision algorithms employed in the DSMC method is summarized in Figure 2.1. When Xe-Xe pairs are selected to collide, the collision probability is determined by using the variable hard sphere (VHS) cross-section. If neutral-ion pairs are selected to collide, they have an equal chance of having MEX and CEX collisions, because the MEX collision cross-section for neutral-ion elastic collisions is equivalent to the CEX collision cross-section, which is demonstrated by Boyd and Dressler [15] as shown in Figure 2.2. The CEX cross-section between neutral and ion was measured by Miller et al. [33], which is parameterized as the following semi-empirical formulas:

$$\begin{aligned} \sigma_{CEX}\left(Xe, Xe^{+}\right) &= 10^{-20}\left[87.3 - 13.6\log_{10}(E)\right] \quad m^2 \\ \sigma_{CEX}\left(Xe, Xe^{2+}\right) &= 10^{-20}\left[45.7 - 8.9\log_{10}(E)\right] \quad m^2 \end{aligned} \tag{2.12}$$

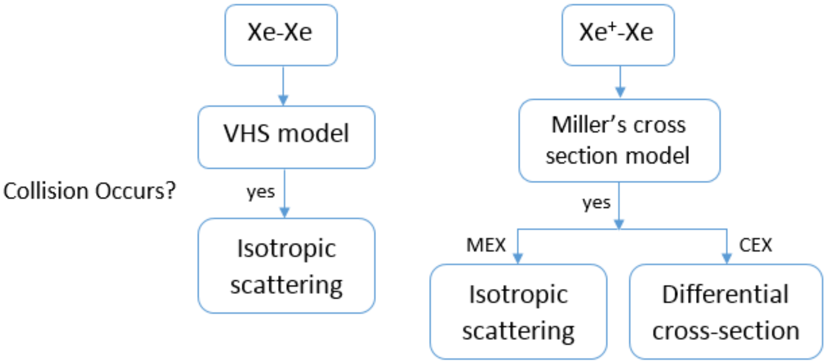

Figure 2.1: Flow chart of collision dynamics in the DSMC model

If the collision candidate pair is determined to collide, its post-collision velocities and deflection, or scattering, angles must be calculated. The post-collision velocities are calculated using the conservation of linear momentum and energy. For all MEX collisions in the current model, the post-collision scattering angle is isotropic—equally probable in all direction.When the collision between Xe^+-Xe results in a CEX collision, a differential cross-section is used to calculate the deflection angle, which is calculated

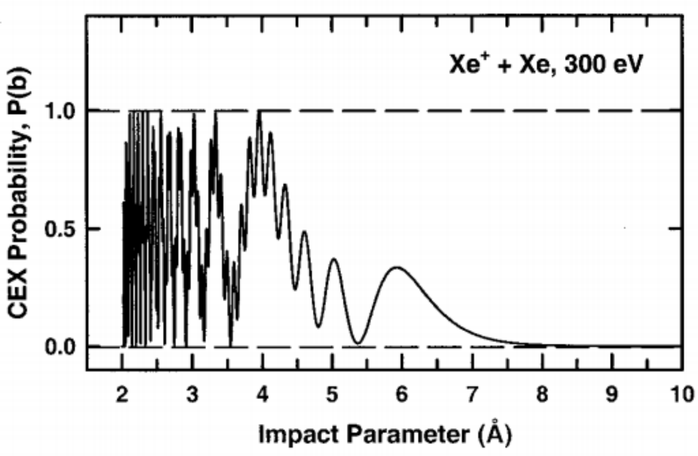

Figure 2.2: Impact parameter dependence of the Xe^{+}-Xe charge-exchange probability at an ion energy of 300 eV [15]

from Ref. [15] for xenon Hall thruster plume modeling. For the DSMC method, we need to have enough particles in each cell to represent the velocity distribution adequately. The rule of thumb is to have at least 20 (preferably, >30) macroparticles per each cell.

2.1.4 Background Pressure Treatment

Although Hall thrusters are designed to operate in space where the background pressure and density are extremely low, Hall thrusters must be tested in a vacuum chamber facility that contains a finite background pressure. Having a finite background pressure affects thruster performance as described in Ref. [34], which includes artificially increased thrust due to the ingestion of background species by the thruster. Therefore, the effect of background pressure in the vacuum chamber should be included when numerically simulating a thruster plume. For valid comparisons with experimental data, a matching backpressure is applied to the current model.

In the current study, a finite background pressure is maintained by having static particles in the background of the simulation domain. Each cell in the domain contains a pre-set number of macroparticles with their velocities sampled from a zero-centered Maxwellian velocity distribution function. When an inflow particle collides with a static background particle, the same collision algorithm is used to calculate the collision probability. If they are determined to collide, the velocity and position of the background particle remains unchanged, while the collision influences the post-collision trajectories of the inflow just as regular collisions. As a result, the finite background pressure can remain constant, while the plume structure changes according to the law of rarefied gas dynamics.

2.1.5 Boundary Conditions for DSMC-PIC Methods

MPIC has four types of boundary conditions: inflow, outflow, symmetry, and wall. The DSMC-PIC methods require number densities, velocities, and temperatures for each heavy species at inlet boundaries, i.e., discharge channel and cathode inlets. The prior MPIC simulation by Huismann assumed that the only heavy particles injected at the cathode inflow were xenon neutrals for simplicity, because there was no data available on the ion properties at the cathode outside of current density measurements [7]. In the current model, full plasma conditions, i.e., ions and electron fluid, as well as neutrals are implemented at the cathode keeper exit as an inflow condition. These conditions were extracted from simulation results provided by a global hollow cathode code OrCa2De developed at the Jet Propulsion Laboratory (JPL) [35].

When a neutral particle hits a wall, the particle will reflect off the wall with a reflecting velocity distribution that varies with the type of the wall. Two main types of wall conditions are considered in the DSMC-PIC methods: specular and diffuse walls. A specular reflection is a reflection off of perfectly smooth surfaces, where the particle's tangential velocity component c_t to the wall remains the same and the normal component c_n changes its sign, with the incidence angle equal to the reflection angle. On the other hand, when a particle bounces diffusely back from a rough surface with the wall temperature T_w, its velocity components tangential to the wall are sampled from the standard Maxwellian distribution as follows:

$$f(c_t)\, dc_t = \frac{1}{\sqrt{2\pi R T_w}} \exp\left(\frac{c_t^2}{2RT_w}\right) dc_t \tag{2.13}$$

And, its normal component is sampled from the biased-Maxwellian distribution:

$$f(c_n)\, dc_n = \frac{c_n}{RT_w} \exp\left(\frac{c_n^2}{2RT_w}\right) dc_n \tag{2.14}$$

where R is the gas constant.

An accommodation coefficient (α) represents the fraction of particles colliding with the wall and is thermalized by the wall. The accomodation coefficient varies from 0 to 1. The remaining fraction ($1 - \alpha$) of the particles is specularly reflected by the wall. In this thesis, a full accommodation coefficient ($\alpha = 1$) is used in all simulations. The internal energy of a reflecting particle can be handled in the same manner. However, for atomic xenon, which is exclusively used in all simulations in the thesis, no internal energy is considered.

When an ion crosses a wall boundary, it loses its charge and reflect as a neutral, following the same physics described above. When particles cross the outflow boundaries, they are subsequently removed from the simulation.

2.2 Transport of Electrons based on Fluid Approach

An understanding of the electron physics is important in the study of Hall thrusters because electrons determine the efficiency and performance of thrusters. For instance, electrons affect the current utilization efficiency by maximizing the ion yield, the ionization efficiency through their average temperature, and the acceleration efficiency by establishing the self-consistent electric field [36].

Since electrons have a mass several orders of magnitude smaller than ions, they move much faster and adjust their velocities more quickly than ions. Thus, this study simulates electrons as a fluid by solving conservation laws. The detailed model in MPIC solves the continuity, momentum, and energy conservation equations that describe the electron fluid at steady-state, and is capable of representing detailed descriptions for electron temperature, velocities, and plasma potential. The following sections describe governing equations and numerical methods for the prior electron fluid model, which neglects the magnetic field. The new electron model that includes the magnetic field effect will be described in Chapter III.

2.2.1 Conservation Laws

MPIC consists of two types of electron models: 1) Boltzmann relation model, and 2) detailed model. The Boltzmann relation, in Eq. (2.15), is one of the most widely used electron models in plasma simulation:

$$\phi = \phi_r + T_e \ln\left(\frac{n_e}{n_r}\right) \tag{2.15}$$

where ϕ is electric potential, T_e is electron temperature in eV, n_e is electron density, and the subscript r indicates the reference values. The Boltzmann relation is the simplest form of a momentum equation derived using the following assumptions: the electron fluid flow is isothermal and collisionless, electron pressure obeys the ideal gas law, and magnetic field effects can be neglected. However, these assumptions are not valid in Hall thruster plume, because the gradients of electron number density, temperature, and potential are large. This is true especially near the channel exit, where magnetic field is still strong.

In order to increase the level of physics as compared to the Boltzmann relation model, a detailed electron fluid model was proposed [37]. The detailed model solves the continuity, momentum, and energy conservation equations that describe the electron fluid at steady state, and is capable of representing more detailed descriptions for electron velocities, temperature, and plasma potential. The electron mass conservation, or the continuity, equation is the following:

$$\frac{\partial n_e}{\partial t} + \nabla \cdot (n_e \mathbf{v}_e) = n_e n_n C_i \tag{2.16}$$

where n_e is the electron number density, $\mathbf{v}_e$ is the electron velocity, n_n is the neutral number density, and C_i is the ionization rate coefficient expressed as a function of electron temperature by Ahedo's model [38]:

$$C_i = \sigma_{i0} c_e \left[1 + \frac{T_e \varepsilon_i}{(T_e + \varepsilon_i)} \right] \exp\left(-\frac{\varepsilon_i}{T_e} \right) \tag{2.17}$$

where ε_i is the energy for primary ionization, $\sigma_{i0} = 5 \times 10^{-20}\, m^2$ is a reference cross section for xenon, c_e is the electron thermal speed, and T_e is in electron volts. By assuming steady-state and introducing a stream-function ψ, such that $\nabla\psi = n_e \mathbf{v}_e = \mathbf{j}_e/e$, we obtain the following equation:

$$\nabla^2 \psi = n_e n_n C_i \tag{2.18}$$

The momentum equation of the detailed electron model is derived from a generalized Ohm's law:

$$\mathbf{J}_e = \sigma_e \left(\mathbf{E} + \mathbf{v_e} \times \mathbf{B} + \frac{1}{e n_e} \nabla P_e \right) \tag{2.19}$$

where σ_e is the electric conductivity defined as:

$$\sigma_e = \frac{e^2 n_e}{m_e \nu_e} \tag{2.20}$$

where the classical electron collision frequency (ν_c) is the sum of the electron-ion collision frequency (ν_{ei}), and the electron-neutral collision frequency (ν_{en}):

$$\nu_c = \nu_{ei} + \nu_e \tag{2.21}$$

By assuming that the magnetic field is negligible in the plume and that the fluid follows the ideal gas law, Eq. 2.19 reduces to the following:

$$\mathbf{J}_e = \sigma_e \left[-\nabla\phi + \frac{1}{en_e}\nabla(n_e k_B T_e) \right] \tag{2.22}$$

The charge continuity equation is the following:

$$\nabla \cdot \mathbf{J}_e = -\frac{\partial \rho_e}{\partial t} \tag{2.23}$$

Assuming steady state, we acquire the following form of the momentum equation by substituting Eq. (2.22) into (2.23):

$$-\nabla \cdot (\sigma_e \nabla\phi) + \nabla \cdot \left[\frac{k_B}{e}\frac{\sigma_e}{n_e}\nabla(n_e k_B T_e) \right] = 0 \tag{2.24}$$

The second term is expanded by using vector identities and by assuming that $\nabla(1/n_e)$ is so small that it is negligible, resulting in the following equation:

$$\begin{aligned} \nabla \cdot (\sigma_e \nabla\phi) = \frac{k_B}{e} \{ & \sigma_e \nabla^2 T_e + \sigma_e T_e \nabla^2 \ln(n_e) \\ & + \sigma_e \nabla \ln(n_e) \cdot \nabla T_e + T_e \nabla\sigma_e \cdot \nabla \ln(n_e) + \nabla\sigma_e \cdot \nabla T_e \} \end{aligned} \tag{2.25}$$

which can then be solved for plasma potential ϕ using a general Poisson's equation solver discussed in Section 2.2.3.

The energy conservation equation for electron fluid is as follows:

$$\frac{D}{Dt}\left(n_e\frac{3}{2}k_BT_e\right) = -p_e\nabla\cdot\mathbf{v}_e - \nabla\cdot\mathbf{q}_e + \mathbf{J}_e\cdot\mathbf{E} - \sum_{h=1}^{N_h}\left[\frac{2m_e}{m_h}\bar{\nu}_{eh}n_e\frac{3}{2}k_B\left(T_e - T_h\right)\right] - \dot{N} \quad (2.26)$$

where subscript h indicates heavy species, $\bar{\nu}_{eh}$ is the electron collision frequency with heavy species, N_h is the number of heavy species, $\dot{N}$ is the net rate per unit volume of nonelastic energy loss from the electrons, the $-p_e\nabla\cdot\mathbf{v}_e$ term is net flux of heat into the element due to pressure, the $\mathbf{J}_e\cdot\mathbf{E}$ term is the rate of increase of electron thermal energy per unit volume by electromagnetic fields, and $\mathbf{q}_e$ is the electron heat flux, which is defined as the product of thermal conductivity, κ_e and negative of the local temperature gradient, $-\nabla T_e$, using Fourier's law. The electron thermal conductivity is defined as [39]:

$$\kappa_e = \frac{2.4}{1+\frac{\nu_{ei}}{\sqrt{2}\nu_e}}\frac{k_B^2n_eT_e}{m_e\nu_e} \quad (2.27)$$

Assuming uniform and steady plasma conditions, and the only inelastic energy loss is due to ionization of neutral xenon, this equation reduces to the following equation:

$$\begin{aligned}\frac{3}{2}n_e(\mathbf{v}_e\cdot\nabla)k_BT_e = &-p_e\nabla\cdot\mathbf{v}_e + \nabla\cdot\kappa_e\nabla T_e + \mathbf{J}_e\cdot\mathbf{E}\\ &-\sum_{h=1}^{N_h}\left[\frac{2m_e}{m_h}\bar{\nu}_{eh}n_e\frac{3}{2}k_B\left(T_e - T_h\right)\right] - \sum_{h=1}^{N_h}\left(n_en_h\varepsilon_iC_i\right)\end{aligned} \quad (2.28)$$

$$\begin{aligned}\nabla^2T_e = &-\nabla\ln(\kappa_e)\cdot\nabla T_e + \frac{1}{\kappa_e}\left[-\mathbf{J}_e\cdot\mathbf{E} + \frac{3}{2}n_e(\mathbf{v}_e\cdot\nabla)k_BT_e + p_e\nabla\cdot\mathbf{v}_e\right]\\ &+\frac{1}{\kappa_e}\left[\frac{3m_e}{m_h}\bar{\nu}_{eh}n_ek_B\left(T_e - T_h\right) + n_en_h\varepsilon_iC_i\right]\end{aligned} \quad (2.29)$$

The current continuity, momentum, and energy equations, in Eqs. (2.18), (2.25), and (2.29), for electron fluid can now be expressed as the following form of a generalized Poisson's equation:

$$-\nabla \cdot [G(x, y)\nabla U(x, y)] = F(x, y) \tag{2.30}$$

where $G(x, y)$ represents a space-dependent coefficient, $U(x, y)$ is the primary variable to be solved, and $F(x, y)$ is a known forcing function. The continuity and energy equations are in the form of $-\nabla^2 U(x, y) = F$, which is identical to Eq. 2.30 when $G(x, y) = 1$. In order to solve all three equations using a single finite element solver conveniently, the quantities on the right-hand side (RHS) should be known and be expressed as a single term forcing function $F(x, y)$. In the current model, the RHS of all three equations have been reduced to one $F(x, y)$ by calculating the derivatives using the least-squares method as described in Ref. [16]. This procedure will be further described in Section 2.2.3.

2.2.2 Background on Continuous Galerkin Finite Element Formulation

In many science and engineering fields, solutions of partial differential equations (PDEs) are required. Since solving PDEs analytically is not always possible, equations are solved numerically in discrete phase space, by using discretization methods such as finite difference, finite volume, and finite element methods. These methods solve sets of algebraic system of linear or nonlinear equations derived as discrete approximations of a problem to obtain numerical solutions. The form of discrete equations solved and the complexity of numerical algorithms used in finite element methods (FEMs) are not very different from finite difference (FD) or finite volume (FV) methods. However, while the FD and FV methods solve for an approximate state at the nodes and cells, respectively, FEMs rely on a functional representation of the solution everywhere on an element by using trial basis, or basis, functions [40]. Moreover, the FEM can handle a complex geometry or vastly different length scales that require non-uniform and unstructured meshes. Because the length scale of the cathode plume and the far-field plume of a Hall thruster vary significantly, using the FEM is ideal for Hall thruster plume simulations. We can use finer mesh near the cathode plume and larger mesh in the far-field plume.

The finite element method is a weighted residual method that uses compactly-supported trial basis functions to approximate a solution on individual elements. The finite element method uses a weak formulation, which is a variational statement of the problem where a test function is integrated against. A weak formulation has the effect of relaxing the problem; instead of finding an exact solution everywhere, we are finding a solution that satisfies the strong form on average over the domain. When the same trial basis function is used for the test function, the method is called the continuous Galerkin finite element method.

In this section, the continuous Galerkin finite element formulation for a 2-D axisymmetric unstructured triangular mesh is derived using the momentum conservation equation in Eq. (2.25). This equation is multiplied by a test function φ_i and integrated over the domain Ω:

$$\int\limits_{\Omega} \varphi_i \left[-\nabla \cdot (\sigma_e \nabla \phi) + f(x,y)\right] d\Omega = 0 \tag{2.31}$$

where $f(x,y)$ is the source terms on the RHS of the momentum equation. By taking integration by parts of the divergence term, the following equation is obtained:

$$\underbrace{-\int\limits_{\partial\Omega} (\varphi_i \sigma_e \nabla \phi) \cdot \vec{n}\, dS}_{\textit{Boundary term}} + \underbrace{\int\limits_{\Omega} \nabla \varphi_i \cdot (\sigma_e \nabla \phi)\, d\Omega + \int\limits_{\Omega} \varphi_i f(x,y)\, d\Omega = 0}_{\textit{Interior elements}} \tag{2.32}$$

This equation is discretized using a trial basis function (φ_j) to approximate the solution variable $U(x,y)$ as the following:

$$U(x,y) \approx \sum_{j=1} U_j \varphi_j \tag{2.33}$$

The present study uses 2-D piecewise linear functions for both the test and trial basis functions. In the continuous Galerkin method, the test function is the same as the trial basis function, and each trial basis function is non-zero only locally over one or a few neighboring elements. To illustrate this, Fig. 2.3 shows 1-D piecewise linear basis functions, φ_k and φ_{k+1}, that are non-zero only in the elements connected to the vertex with index k and $k+1$, respectively. Because the basis functions are zero at the edge of their domain of influence, the boundary term in Eq. (2.32) is zero for all internal elements.

Applying Eq. (2.33) to Eq. (2.32), we acquire a system of linear algebraic equations as follows:

$$\sum_{j=1}^{N_j} \underbrace{\left[\int_\Omega \nabla\varphi_i \cdot (\sigma_e \nabla\varphi_j)\, d\Omega \right]}_{A_{ij}} \phi_j + \underbrace{\int_\Omega \varphi_i f(x,y)\, d\Omega}_{F_i} = 0 \tag{2.34}$$

which is an $N \times N$ matrix system, $\mathbf{AU}+\mathbf{F} = 0$, and the matrix A_{ij} is called a stiffness matrix. The stiffness matrix is assembled by looping over all elements.

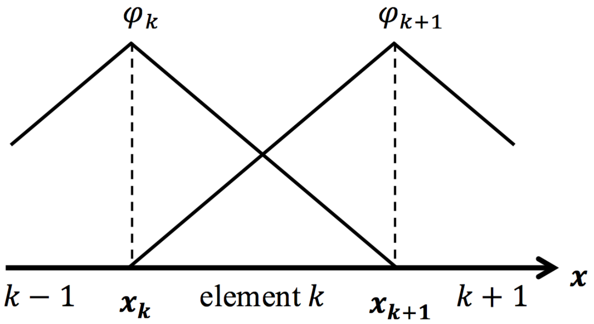

Figure 2.3: 1-D piecewise linear trial basis function, showing non-zero magnitude of trial basis functions φ_k on the node k and zero on adjacent nodes

To evaluate the integrals in Eq. (2.34), a reference coordinate system is used, mapping an arbitrary triangle to a reference triangle as shown in Figure 2.4. The global space (x, y) is transformed to the reference space (ξ, η) using Jacobian:

$$J = \frac{\partial \mathbf{x}(x, y)}{\partial \boldsymbol{\xi}(\xi, \eta)} \tag{2.35}$$

where

$$\mathbf{x}(\xi, \eta) = \mathbf{x}_1 + (\mathbf{x}_2 - \mathbf{x}_1)\xi + (\mathbf{x}_3 - \mathbf{x}_1)\eta \tag{2.36}$$

For derivatives, the chain rule is used:

$$\frac{\partial f}{\partial \mathbf{x}} = \frac{\partial f}{\partial \boldsymbol{\xi}} \frac{\partial \boldsymbol{\xi}}{\partial \mathbf{x}} = \frac{\partial f}{\partial \boldsymbol{\xi}} J^{-1} = \nabla_{\boldsymbol{\xi}} J^{-1} \tag{2.37}$$

The determinant of the Jacobian is two times the area of element k:

$$|J| = 2\Delta_k = \begin{vmatrix} 1 & x_1 & y_1 \\ 1 & x_2 & y_2 \\ 1 & x_3 & y_3 \end{vmatrix} \tag{2.38}$$

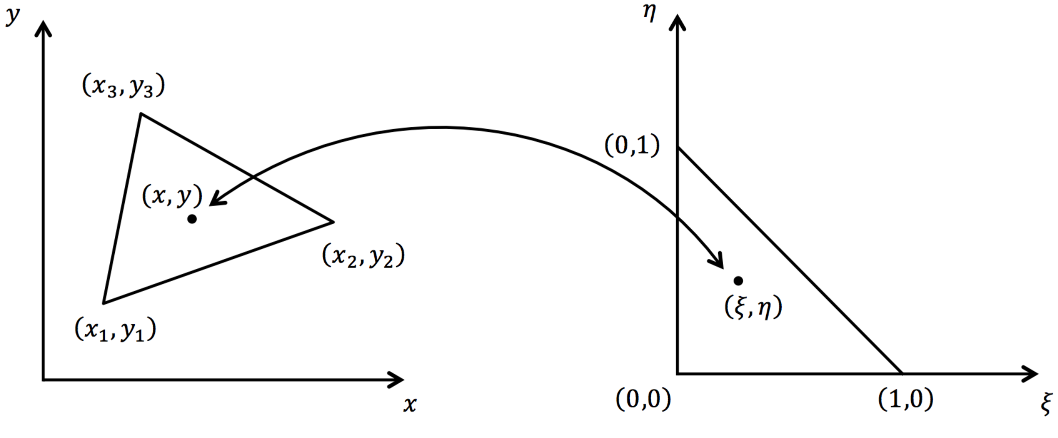

Figure 2.4: Transformation from an arbitrary triangle in the physical space (x, y) to a reference triangle in the reference space (ξ, η), and the inverse mapping.

The piecewise linear basis functions used in Eq. (2.33) are given in the following:

$$\begin{aligned} \varphi_1 &= 1 - \xi - \eta \\ \varphi_2 &= \xi \\ \varphi_3 &= \eta \end{aligned} \tag{2.39}$$

for triangular elements. The integrals over the element k should be transformed into integrals over the reference element R. Transformation of the forcing vector is shown as in the following:

$$\int_{\Omega_k} f(x,y)\, d\Omega = \int_{\Omega_R} f(x(\xi,\eta), y(\xi,\eta))\, |J| d\xi d\eta \tag{2.40}$$

Similarly, transformation of the divergence term in Eq. (2.40) becomes:

$$\int_{\Omega_k} \nabla\varphi_i \cdot (\sigma_e \nabla\varphi_j)\, d\Omega_k = \int_{\Omega_R} (\nabla_{\boldsymbol{\xi}}\varphi_i J^{-1}) \cdot (\sigma_e \nabla_{\boldsymbol{\xi}}\varphi_j J^{-1})\, |J| d\xi d\eta \tag{2.41}$$

2.2.3 Prior Generalized Poisson's Equation Solver

The prior electron model without the magnetic field effect solves all governing equations, i.e., Eqs. (2.18), (2.25), and (2.29), as a single generalized Poisson's equation (Eq. (2.30)). In order to use a single finite element solver, the derivatives in the source terms of all equations are: 1) calculated using the least-squares method described in Section 2.1.2 that is also used to calculate $\mathbf{E} = -\nabla\phi$, and 2) reduced to a single linear function $f(x, y)$. In the generalized Poisson's equation, if $G(x, y)$ and $F(x, y)$ can be represented as scalar linear functions within each element, then the integrals in the stiffness matrix and forcing function can be calculated analytically, which simplifies the FEM solver very effectively. The derivatives of the test function of Eq. (2.41) in the reference space is:

$$\nabla_\xi \varphi_i J^{-1} = \begin{bmatrix} -1 & -1 \\ 1 & 0 \\ 0 & 1 \end{bmatrix} \left(\frac{1}{|J|} \begin{bmatrix} y_2 - y_3 & x_1 - x_3 \\ y_1 - y_2 & x_2 - x_1 \end{bmatrix} \right) = \frac{1}{|J|} \begin{bmatrix} y_2 - y_3 & x_3 - x_2 \\ y_3 - y_1 & x_1 - x_3 \\ y_1 - y_2 & x_2 - x_1 \end{bmatrix} \tag{2.42}$$

where x and y are physical coordinates in 2-D space. The coefficient for the diffusion operator is assumed to be a linear function in an element such that:

$$G(x,y) \approx \frac{1}{3}(g_1 + g_2 + g_3) \tag{2.43}$$

where g_1, g_2, and g_3 are nodal values.

Similarly, Eq. (2.40) can also be computed analytically by using a linear approximation of $f(x,y) \approx f_1\varphi_1 + f_2\varphi_2 + f_3\varphi_3$ such that:

$$F_i^k = \int\limits_{\Omega_k} \varphi_i f(x,y)\, d\Omega_k \approx \int\limits_{\Omega_k} \varphi_i \left(f_1\varphi_1 + f_2\varphi_2 + f_3\varphi_3\right)\, d\Omega_k \tag{2.44}$$

Using the following theorem:

$$\int\limits_{\Omega_k} (\varphi_1)^m (\varphi_2)^n (\varphi_3)^l \, dxdy = \frac{m!n!l!}{(m+n+l+2)!} 2\Delta_k \tag{2.45}$$

Eq. (2.44) becomes:

$$\begin{aligned} F_1^k &= \int\limits_{\Omega_k} \varphi_1 \left(f_1\varphi_1 + f_2\varphi_2 + f_3\varphi_3\right)\, dxdy \approx f_1\frac{\Delta_k}{6} + f_2\frac{\Delta_k}{12} + f_3\frac{\Delta_k}{12} \\ F_2^k &= \int\limits_{\Omega_k} \varphi_2 \left(f_1\varphi_1 + f_2\varphi_2 + f_3\varphi_3\right)\, dxdy \approx f_1\frac{\Delta_k}{12} + f_2\frac{\Delta_k}{6} + f_3\frac{\Delta_k}{12} \\ F_3^k &= \int\limits_{\Omega_k} \varphi_3 \left(f_1\varphi_1 + f_2\varphi_2 + f_3\varphi_3\right)\, dxdy \approx f_1\frac{\Delta_k}{12} + f_2\frac{\Delta_k}{12} + f_3\frac{\Delta_k}{6} \end{aligned} \tag{2.46}$$

The final matrix form of the systems of linear equations is as follows:

$$\Delta_k \left[\frac{1}{3}(g_1 + g_2 + g_3)(\nabla_\xi \varphi_i J^{-1}) \cdot (\nabla_\xi \varphi_j J^{-1}) \left\{ u_k \right\} - \frac{1}{12} \begin{bmatrix} 2 & 1 & 1 \\ 1 & 2 & 1 \\ 1 & 1 & 2 \end{bmatrix} \left\{ f_k \right\} \right] = 0 \tag{2.47}$$

For the continuity and energy equations, where the coefficient $G(x, y) = 1$, the $(g_1 + g_2 + g_3)/3$ term in Eq. (2.47) becomes 1. For slightly different derivations, see Refs. [16] and [40].

Since the stiffness matrix for the current formulation is symmetric and positive-definite, the system is solved using the conjugate gradient method [16].

2.2.4 Boundary Conditions for the FEM

When assembling the stiffness matrix, we must consider boundary conditions. The following Dirichlet boundary conditions can be achieved:

$$U_{boundary} = u_{Dirichlet} \tag{2.48}$$

by replacing the forcing vector **F** with $-u_{Dirichlet}$, and the entire row of the stiffness matrix with zeros except the main diagonal, which is replaced by 1. For Neumann boundary conditions, the boundary term from Eq. (2.32) becomes the following equation by transferring over to the forcing vector while the stiffness matrix remains the same:

$$-\int_{\partial\Omega} (\varphi_i \sigma \nabla\phi) \cdot \vec{n}\, dS = \varphi_i(\sigma\nabla\phi)\Big|_{boundary} \tag{2.49}$$

In the current simulation, the gradient term in the Neumann boundary condition is always zero for the momentum equation, which is naturally satisfied by the continuous Galerkin method, not contributing to the forcing term and stiffness matrix.

2.3 Summary of MPIC Algorithms

This section summarizes the general steps of the hybrid DSMC-PIC-fluid methods in MPIC. As discussed throughout this chapter, the DSMC method simulates the transport of neutral particles and the collision dynamics between the heavy species, the PIC method simulates the transport of ions in the presence of electric fields, and the detailed model simulates the electrons as a fluid. The procedure for these methods in MPIC is as follows:

1. Calculate the charge density at grid points from the charge distribution in cells
2. Solve electron fluid conservation laws, i.e., continuity, momentum, and energy equations, to obtain electron velocity, potential field, and temperature on each grid point
3. Calculate ionization of neutrals in each cell using the following equation: $n_i = C_i n_i n_n \Delta t$, where the ionization rate C_i is computed by Eq. (2.18)
4. Calculate electric fields on each grid point by differentiating plasma potential: $\mathbf{E} = -\nabla\phi$
5. Perform intermolecular collisions
6. Inject new macroparticles at inlet boundaries
7. Compute post-collision velocities and angles
8. Interpolate the ion acceleration in a cell from the particle positions and the electric field at each grid point
9. Move particles and compute their interactions with all boundaries
10. Sample macroscopic flow information.

CHAPTER III

A New Electron Model with Magnetic Field Effects

This chapter describes the newly developed electron model that includes magnetic field effects. Section 3.1 discusses the motivation to develop the new model. A detailed description of the physical and numerical models of the new momentum equation is described in Section 3.2. Lastly, the implementation and verification of the new model are described in Section 3.3.

3.1 Motivation for Developing New Electron Model

As briefly discussed in Chapter I, many Hall thruster plume simulations [5, 13, 14, 29, 17, 41, 7, 42] have neglected the magnetic field effects because modeling the magnetic field in the plume is complicated. The magnetic field in the plume of a HET is two-dimensional (2-D) and its topology can be quite complex. Solving the full 2-D magnetic field is numerically challenging due to the cross partial derivative term (i.e., $\frac{\partial}{\partial x}(\frac{\partial}{\partial y})$). Thus, plume simulations usually neglect the magnetic field effects by assuming that the magnetic field strength in the plume is relatively weaker than the strength of the field inside the discharge chamber of a Hall thruster.

The prior Hall thruster simulations using MPIC [7, 42] also have neglected the magnetic field, which resulted in the over-estimation of the plasma potential and electron temperature compared to experimental data. Figure 3.1 shows the plasma potential calculated by Huismann using MPIC. As shown in the red curve, the plasma potential was over-predicted by more than 100 V in the very near-field plume ($Z/D_{thruster} \approx 0.1$). In order to improve the agreement between simulation results and experimental data, Huismann [7] proposed mapping the discharge chamber inflow boundary from the exit plane of the thruster discharge chamber onto an "effective inlet" for MPIC to start its simulations outside of the strong magnetic field regions. This effective inlet is the magnetic field line shown in Fig. 3.2. Using this effective inlet improves agreement of the simulation result with experimental data, which is shown in the green curve of Fig. 3.1. Huismann's study shows that the magnetic field needs to be included in plume simulations to accurately capture the electron

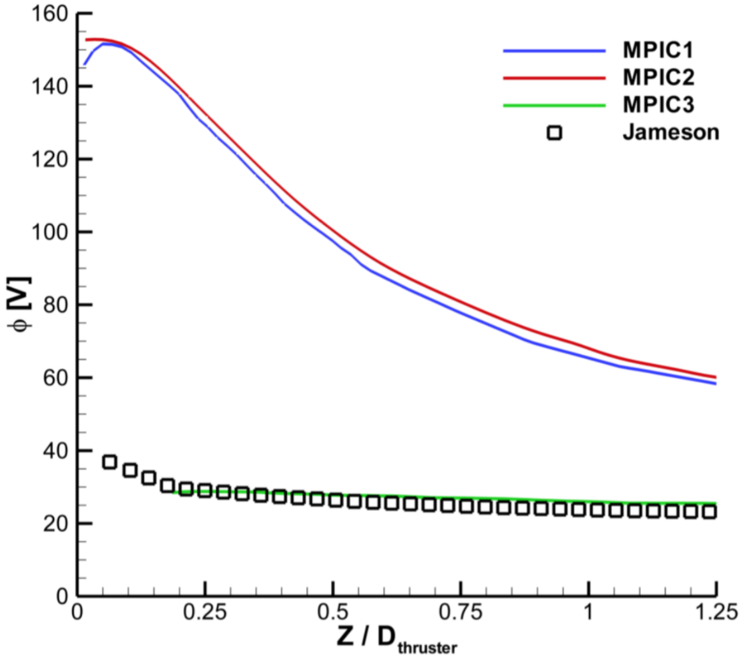

Figure 3.1: Axial profile of plasma potential comparing simulation results with experimental data measured by Jameson [43]. The red curve shows the plasma potential calculated using the standard thruster exit plane as an inflow boundary, while the green curve shows the potential calculated using the effective inlet proposed by Huismann [7].

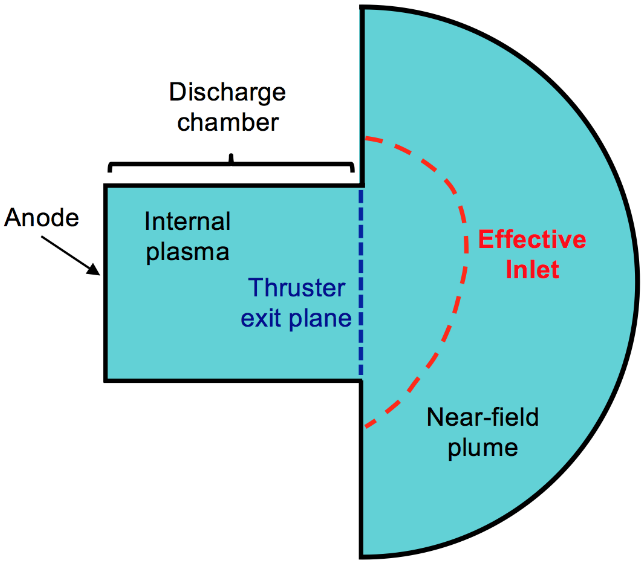

Figure 3.2: Schematic of the HPHall domain showing the “effective” inlet proposed by Huismann [7]. The regions of the strong magnetic field effect are eliminated from the computational domain by using the effective inlet to couple the discharge plasma to the plume. simulation.

physics in the plume. Moreover, experimental measurements of the near-field plume plasma from Hall thrusters have shown that the magnetic field lines indeed leak into the plume [5, 6]. This field affects electron motion in the near-field plume region, and ultimately drive the efficiency and performance of a Hall thruster.

In Fig. 3.3, the magnetic field topology in a 6-kW (H6) Hall thruster are plotted. The thruster plume contains a magnetic field separatrix, a purely axial component along the cathode centerline axis, and a purely radial component near the discharge channel exit. In Hall thrusters, the maximum magnetic field strength occurs near the exit plane of the discharge channel walls. Some thrusters, including the H6 thruster, have the maximum magnetic field strength occurring in the very near-field plume of the thruster. Figure 3.4 shows the normalized radial and axial magnetic fields along the discharge channel centerline. The peaks of these fields occur downstream of the thruster exit, which is the near-field plume. The axial magnetic field along the cathode centerline is also strong, i.e., 1.4 times stronger than the strength of the

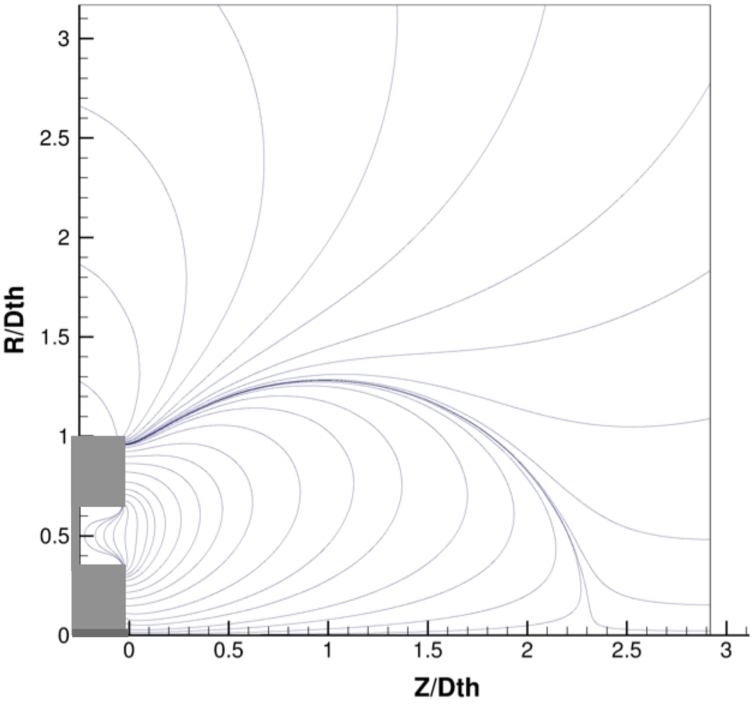

Figure 3.3: Magnetic field topology in the H6 thruster.

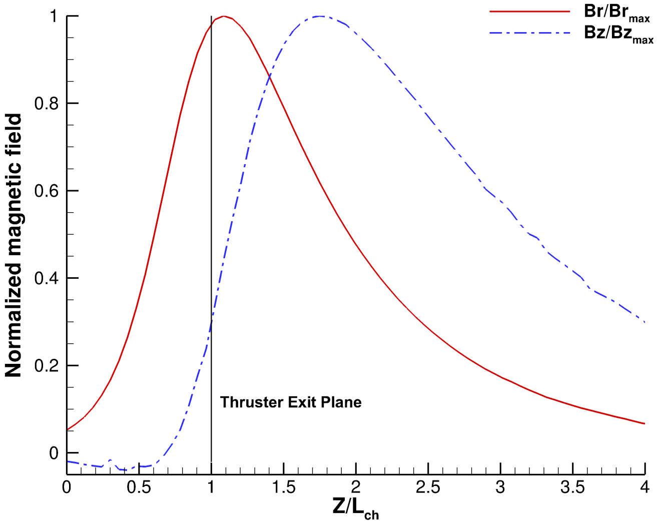

Figure 3.4: Axial profiles of normalized magnetic fields along the discharge chamber centerline. The maximum radial magnetic field (B_r) and radial magnetic field (B_z) occur in the near-field plume, downstream of the thruster exit plane.

maxim radial magnetic field along the discharge channel. Since the magnetic field is still strong in the near-field plume regions and thus can affect the plume structure, it should be included in plume simulations to model the electron transport across the field lines correctly, which is one of the main factors driving the performance of a HET.

The current study takes up Huismann's investigation of using an effective inlet to model a Hall thruster with the improved cathode boundary conditions he suggested at the end of his study [7]. Since the results using the models neglecting magnetic field effects could not accurately predict plasma properties, a new electron model has been developed with the hope of improving agreement between the simulation results and experimental data. Because electron motion is largely influenced by the topology and shape of the magnetic field, capturing electron transport across any and all magnetic field shapes is important to provide accurately predict plasma properties. Since some thrusters may have complex curvature of magnetic field lines, the magnetic field effect has to become fully two-dimensional. The new electron model has the capability to model electron transport across a complex magnetic field topology. The main equation affected by the presence of a magnetic field is the momentum conservation equation. Thus, the new momentum equation is derived and applied to the continuous Galerkin finite element formulation. The new equation now contains an electron mobility tensor coefficient, which is the main difference between the new and existing physical momentum equations. Detailed physical and numerical descriptions of the new model are explained below.

3.2 Physical and Numerical Models of the New Momentum Equation in MPIC

This section describes a second order continuous Galerkin finite element method using piecewise linear approximation in unstructured triangular meshes for the new momentum conservation equation in MPIC. During the Galerkin finite element formulation, 3-D cylindrical coordinate is used first, and 2-D axisymmetric assumption is applied later.

The new momentum conservation equation that includes the magnetic field is also derived from the generalized Ohms law, as in Eq. (2.19), with a slight modification:

$$\mathbf{J} = \mu(\mathbf{J} \times \mathbf{B}) + \sigma_e \left(\mathbf{E} + \frac{1}{en_e} \nabla P_e \right) \tag{3.1}$$

where $\mu = e/(m_e \nu_e)$ is the electron mobility. Combining the **J** term on the RHS with the **J** term on the left results in the following equation in a matrix form:

$$\underline{\underline{\mu}} \mathbf{J} = \sigma_e [\mathbf{E} + \frac{1}{en_e} \nabla \mathbf{P}] \tag{3.2}$$

in a vector form, or the following matrix form:

$$\underbrace{\begin{bmatrix} 1 & -\mu B_z & \mu B_\theta \\ \mu B_z & 1 & -\mu B_r \\ -\mu B_\theta & \mu B_r & 1 \end{bmatrix}}_{\underline{\underline{\mu}}} \begin{bmatrix} j_r \\ j_\theta \\ j_z \end{bmatrix} = \sigma_e \begin{bmatrix} E_r + \frac{1}{en_e} \nabla_r P_e \\ E_\theta + \frac{1}{en_e} \nabla_\theta P_e \\ E_z + \frac{1}{en_e} \nabla_z P_e \end{bmatrix} \tag{3.3}$$

where $\underline{\underline{\mu}}$ is a tensor form of the electron mobility coefficient. Solving for **J** results in the following equation:

$$\mathbf{J} = \underline{\underline{\mu}}^{-1} \sigma_e (\mathbf{E} + \frac{1}{en_e} \nabla P_e) \tag{3.4}$$

Substituting this equation into the steady-state charge continuity equation, we acquire a new governing equation to solve:

$$\nabla \cdot (\underline{\underline{\mu}}^{-1}\sigma_e \nabla \phi) = \nabla \cdot (\underline{\underline{\mu}}^{-1}\frac{\sigma_e}{en_e}\nabla P_e) \tag{3.5}$$

where $\underline{\underline{\mu}}^{-1}$ is the inverse of $\underline{\underline{\mu}}$:

$$\underline{\underline{\mu}}^{-1} = \frac{1}{1+\mu^2 B^2}\begin{bmatrix} 1+\mu^2 B_r^2 & \mu^2 B_r B_\theta + \mu B_z & \mu^2 B_r B_z - \mu B_\theta \\ \mu^2 B_r B_\theta - \mu B_z & 1+\mu^2 B_\theta^2 & \mu^2 B_\theta B_z + \mu B_r \\ \mu^2 B_r B_z + \mu B_\theta & \mu^2 B_\theta B_z - \mu B_r & 1+\mu^2 B_z^2 \end{bmatrix} \tag{3.6}$$

When the magnetic field effect is present in weakly-ionized plasma, electrons diffuse across magnetic field lines, which is usually taken as Bohm diffusion or anomalous diffusion in the Hall thruster community. This Bohm diffusion coefficient is much greater than the classical electron diffusion, which is commonly attributed to instabilities in the discharge. Since this anomalous electron diffusion is still poorly understood, the coefficient α_e is often used in Hall thruster simulations. The anomalous electron collision frequency ν_B is defined as:

$$\nu_B = \frac{\alpha_a}{16}\omega_c \tag{3.7}$$

The total electron collision frequency is now: $\nu_e = \nu_{ei} + \nu_{en} + \nu_B$.

3.2.1 Continuous Galerkin Method with Tensor Coefficient

Following the same procedure in Section 2.2.2, the new momentum conservation equation is multiplied by the piecewise linear test function and integrated over the domain:

$$\int\limits_{\Omega} \varphi_i \left[-\nabla \cdot (\underline{\underline{\mu}}^{-1}\sigma_e \nabla \phi) + \nabla \cdot (\underline{\underline{\mu}}^{-1}\frac{\sigma_e}{en_e}\nabla P_e) \right] d\Omega = 0 \tag{3.8}$$

Because of the Laplacian-like operator on both terms, integration by parts is performed on them once, which results in the following weak form:

$$\begin{aligned} &\int_{\partial\Omega} (\varphi_i \underline{\underline{\mu}}^{-1}\sigma_e \nabla\phi)\cdot\vec{n}\,dS - \int_{\Omega} \nabla\varphi_i\cdot(\underline{\underline{\mu}}^{-1}\sigma_e\nabla\phi)\,d\Omega \\ &\qquad - \int_{\partial\Omega} (\varphi_i \underline{\underline{\mu}}^{-1}\frac{\sigma_e}{en_e}\nabla P)\cdot\vec{n}\,dS + \int_{\Omega} \nabla\varphi_i\cdot(\underline{\underline{\mu}}^{-1}\frac{\sigma_e}{en_e}\nabla P)\,d\Omega = 0 \end{aligned} \tag{3.9}$$

The boundary terms $\int_{\partial\Omega}$ become zero because the basis function is only non-zero inside an element. Transforming coordinate systems from a 3-D cylindrical to a 2-D axisymmetric system, the integrals in the above equation become:

$$\int_{\Omega_k} d\Omega = \int_{\Omega_k} r\,drd\theta dz = \int_{\Omega_k} 2\pi r\,drdz \tag{3.10}$$

where r is the distance from the the symmetry axis to an element node.

Considering only the interior elements, a weak formulation of the above equation becomes an $\mathbf{AU}+\mathbf{F}=0$ system:

$$\begin{aligned} &-\sum_{j=1}^{N_j} \underbrace{\left[\int_{\Delta_k} 2\pi\nabla\varphi_i\cdot(\underline{\underline{\mu}}^{-1}\sigma_e\nabla\varphi_j)r\,drdz\right]}_{A_{ij}}\phi_j \\ &\qquad + \underbrace{\sum_{j=1}^{N_j}\left[\int_{\Delta_k} 2\pi\nabla\varphi_i\cdot(\underline{\underline{\mu}}^{-1}\frac{\sigma_e}{en_e}\nabla\varphi_j)r\,drdz\right]P_j}_{F_i} = 0 \end{aligned} \tag{3.11}$$

The tensor coefficient $\underline{\underline{\mu}}^{-1}$ makes the analytic integrals difficult as shown in Eqs. (2.47). Rather, the integrals are performed numerically using Dunavant's Gaussian quadrature rules [44]. For a function g, the quadrature rule is defined as:

$$\int_{\Omega_{k^*}} g(\xi, \eta)\, d\Omega_{k^*} = \sum_{q=1}^{N_q} \omega_q g(\xi_q, \eta_q) \tag{3.12}$$

where $*$ indicates the transformed coordinate (ξ, η). Using the quadrature rule makes an implementation of higher-order basis functions possible and straightforward for the future, instead of piecewise linear functions. Currently, the quadrature rules of up to the 14^{th} order are implemented, where the order of a quadrature rule is the degree of the lowest degree polynomial used to approximate the integral.

Although the new model also uses the continuous Galerkin approximation, the new model applies the forcing term $\nabla \cdot (\underline{\underline{\mu}}^{-1} \sigma_e \frac{1}{en_e} \nabla P)$ directly into a weak formulation as is without expanding or making any assumptions, while the existing model expands the term first, then computes derivatives using another method to reduce all terms into a known linear function $f(x, y)$. Even if the source terms in Eq. (2.25) and Eq. (3.5) are analytically indistinguishable except for the $\nabla 1/n_e$ terms, directly putting the governing equation into a weak formulation is more accurate than the expanded form. Since FEM solves the weak equation instead of the strong form, solving Eq. (3.11) is different from solving the existing momentum equation in Eq. (2.34) even in the case when $B = 0$. Thus, now we have the gradient of the test function, $\nabla\varphi$ instead of the test function itself φ. Another difference in the numerical approach results by approximating $\nabla\varphi_i \cdot (\underline{\underline{\mu}}^{-1} \sigma_e \nabla P_e)$ vs. $\varphi f(x, y)$ where $f(x, y)$ is calculated using a different method, i.e., the least-squares method. Using the least-squares method and approximating $f(x, y)$ made it possible to use a single Poisson's equation solver to solve all three governing equations. However, the truncation error may result in large differences if the accrued error is large enough. The current continuous Galerkin formulation should be more robust and accurate than the existing formulation. Thus, in the current electron model, we solve the momentum equation using the new FEM and solve the remaining equations using the general Poisson's equation solver.

3.2.2 Solving Matrix System

The conjugate gradient method is an algorithm to solve systems of linear equations ($\underline{A}\mathbf{x} = \mathbf{b}$) that involve a symmetric and positive-definite matrix [16]. Since the stiffness matrix of the new momentum equation is not symmetric and non-positive-definite, the conjugate gradient method no longer can be used. Therefore, the biconjugate gradient (BCG) method is used. A basic description of the BCG method can be found in Ref. [45].

3.3 Implementation and Verification

In order to verify the algorithms for solving the new momentum equation, the new FEM solver described above is first coded in MATLAB and then tested using the method of manufactured solutions. The method of manufactured solutions is a relatively simple approach to verify numerical models and their orders of accuracy. In this study, the new model is tested using various types of functions as manufactured solutions, including polynomial, sinusoidal, and exponential solutions, or some combination of these. As an example, one of the manufactured solutions is shown below:

$$u_{exact} = 25 \exp\left(-\frac{x}{2}\right) - 2xy^3 \tag{3.13}$$

This manufactured solution is substituted into the new momentum equation in Eq. (3.5) in order to analytically acquire a source term that satisfies the governing equation. In this case, the source term is:

$$f(x,y) = -\underline{\underline{\mu}}^{-1}\sigma_e \left[\frac{25}{4}\exp\left(-\frac{x}{2}\right) + 24y\right] \tag{3.14}$$

The convergence study is performed using the L_2-norm error:

$$\begin{aligned}\|e\|_{L2} &= \sqrt{\sum_{k=1}^{N_k} \int_{\Omega_k} \left(u_h - u_{exact}\right)^2 \, d\Omega_k} \\ &= \sqrt{\sum_{k=1}^{N_k} \sum_{q=1}^{N_q} w_q \left[u(x_q, y_q)_h - u_{exact}(x_q, y_q)\right]^2 |J|}\end{aligned} \tag{3.15}$$

where u_h is the numerical solution and w_q is the weight of a quadrature point (x_q, y_q). Using this formula, a grid convergence study has been performed to confirm the order of accuracy of this method, which we expect to be of 2^{nd} order for piecewise linear functions. For the domain $1m \times 1m$, four different triangular meshes are tested using the uniform right triangles with $\Delta x = 0.25, 0.145, 0.0625$, and 0.03125. The order of accuracy can be determined as the slope of the log-plot of the error vs. mesh size. This particular manufactured solution is tested using the 2^{nd} and 14^{th} orders of quadrature rules. For each mesh and quadrature rule, the error using L_2-norm is calculated and plotted against the mesh size in Figure 3.5. The slope here is approximately 2, thus confirming our expected 2^{nd} order accuracy.

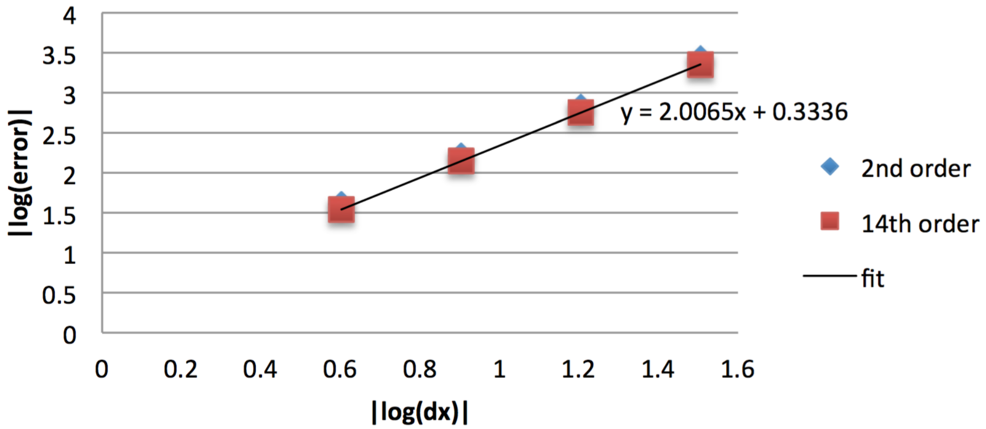

Figure 3.5: Grid convergence study using manufactured solution; two different quadrature points were used, and 2nd order was confirmed.

Next, the new model is implemented in MPIC, which is written in C/C++, as a

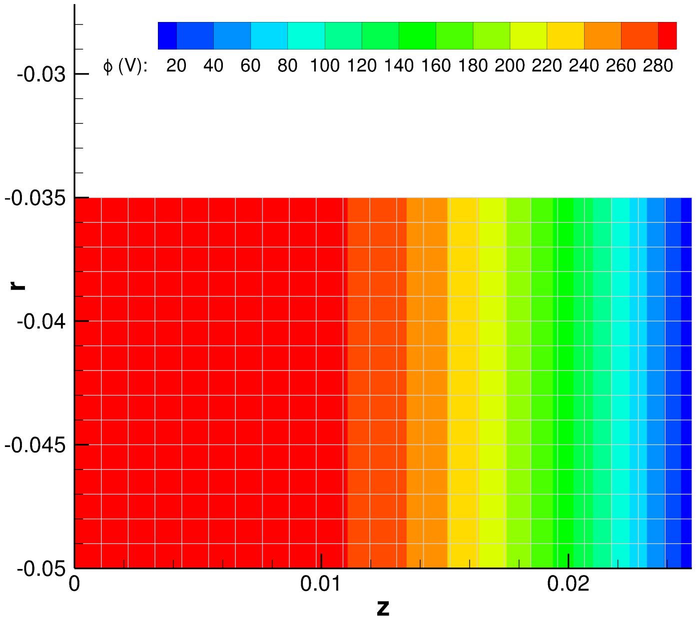

Figure 3.6: Contour plots of plasma potential calculated by a fully 2-D finite difference model by Dragnea [46].

sub-electron model. In order to verify the new model in MPIC with a Hall-thruster-like case, a mock-Hall thruster test case was simulated by Dragnea using a new 2-D axisymmetric finite-difference electron model [46], as shown in Fig. 3.6. Dirichlet boundary conditions of 300 V and 0 V are applied at the left (anode-like) and the right (cathode-like) boundaries, respectively. Neumann conditions with zero-gradient are applied at the top and the bottom boundaries, respectively, which are considered as discharge channel walls in a Hall thruster. The plasma potential is calculated in the domain and compared against Dragnea's simulation result using the matching input variables provided, including pressure, collision frequencies, magnetic field, and number densities. A contour plot of the plasma potential calculated by the new electron model is shown in Figure 3.7. Both models show similar result. A quantitative confirmation is shown in Figure 3.8 through a grid convergence study assuming the solution provided is the true solution. As a result, 2^{nd} order accuracy of the electron model is confirmed.

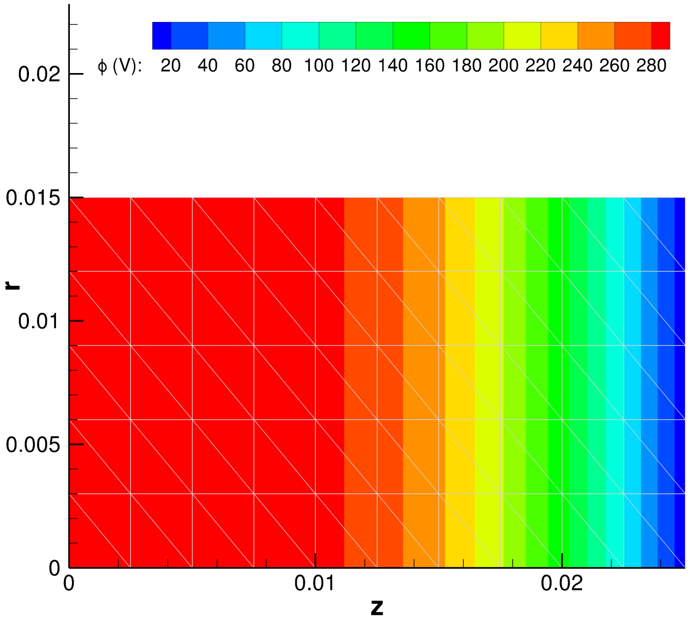

Figure 3.7: Contour plots of plasma potential calculated using the new model.

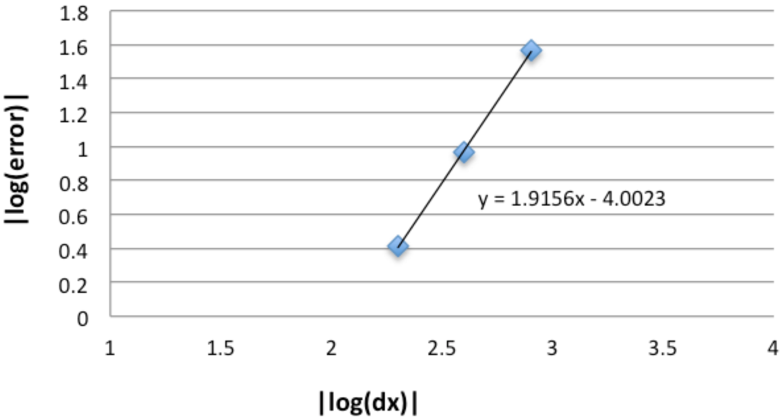

Figure 3.8: Grid convergence study using a Hall-thruster-like case.

As a final validation of the new model, the simulation results will be compared against various experimental data of the H6 Hall thruster in Chapter IV. The magnetic field data of the H6 Hall thruster is provided by the Jet Propulsion Laboratory. The magnetic field data are read in Tecplot 360, and is interpolated to the computational grid points by using inverse distance weighting.

3.4 Summary of the New Electron Model

The new fluid electron model is described in this chapter. The physical model of the new governing equation that includes the effect of the magnetic field is derived in a 3-D cylindrical coordinate system without loss of generality. The new model has the tensor transport coefficient $\underline{\underline{\mu}}^{-1}\sigma_e$ on both the LHS and the RHS of Eq. (3.5), as a result of including the magnetic field effects, while the prior model has a scalar coefficient σ_e. When the applied magnetic field is zero, the new momentum equation reduces to the prior momentum equation:

$$\nabla \cdot (\underline{\underline{\mu}}^{-1}\sigma_e \nabla \phi) = \nabla \cdot (\sigma_e \nabla \phi) \tag{3.16}$$

because $\underline{\underline{\mu}}^{-1}$ reduces to an identity matrix when $B = 0$.

The prior model had a single general Poisson equation solver that uses the least-squares method to estimate derivative terms on the forcing function. All terms are then added in order to calculate one linear forcing term. In contrast, the new continuous Galerkin finite element model solves the governing equation directly, without using the least-squares method. This new formulation minimizes any truncation errors that could be accumulated over many timesteps if derivatives are estimated using the least-squares method. Then, the sum of the derivative terms is again approximated as a linear forcing function.

To numerically integrate the discretized equation, the Dunavant quadrature rule up to the 14^{th} order is implemented. The new electron model can simulate the 2-D axisymmetric effects of the magnetic field in any shape.

CHAPTER IV

Simulation of a Hall-Effect Thruster plume using the New Electron Model

The hybrid particle-fluid plume model, MPIC, described in Chapters II and III is applied to simulate the plume of the H6 Hall thruster. A series of simulation results and experimental validation is presented throughout this chapter. Section 4.1 describes the computational domain, flow conditions, and operating conditions of the tests from which experimental data are used for model validation. Section 4.2 reports the comparisons between the prior model and the new model without the magnetic field. Then, simulation results including magnetic field effects are presented in Section 4.2. Finally, the accuracy of the new model is performed through direct comparisons with detailed experimental data (Section 4.4).

4.1 Simulation Setup for the H6 Hall Thruster Plume

In order to enable valid comparisons between simulation results and experimental data, simulations are performed to match the thruster operating conditions and background pressure of the vacuum facilities. Section 4.1.1 describes operating conditions of the H6 thruster. Section 4.1.2 describes the computational domain and boundary conditions used for the simulations.

4.1.1 Thruster Operating Condition

The Hall thruster used in this study is a 6-kW laboratory (H6) Hall thruster (Fig. 1.3), which was jointly developed by the Air Force Research Laboratory, Jet Propulsion Laboratory, and the University of Michigan [8]. A series of simulation results is compared with plasma measurements in the plume of the H6 thruster in order to validate the model. The H6 thruster experiment was conducted at the following nominal conditions: discharge voltage of 300 V, discharge current of 20 A, anode flow rate of 20 mg/s of xenon, and cathode flow rate measuring 7% of the anode flow.

At the nominal condition, plasma potential, electron temperature, and electron number density were measured by Sekerak [47] using high-speed dual Langmuir probes. The uncertainties associated with these measurements were approximately 25%. The measurement was taken in the Large Vacuum Test Facility (LVTF) of the Plasmadynamics and Electric Propulsion Laboratory (PEPL) at the University of Michigan. The background pressure during the thruster operating was $1 \pm 0.1 \times 10^{-5}$ Torr.

The ion current density measurements were performed by Reid [48] using two Faraday cup probes. The uncertainty associated with the near-field probe measurements is ±10%, whereas the far-field probe measurements have $\pm 0 - 50\%$ on the integrated beam current. The measurement also occurred in the LVTF at PEPL. The background pressure during the thruster operating was 1.5×10^{-5} Torr.

Since the difference in the background pressures between Sekerak's and Reid's experiments is very small (i.e., 5×10^{-6}), the simulation results using these two background pressures were identical. Therefore, simulations are performed using the background pressure of 1.1×10^{-5} Torr.

4.1.2 Computational Domain and Boundary Conditions

The current model simulates a 2-D axisymmetric domain with the axis of symmetry being the centerline of the H6 Hall thruster as well as the cathode. Figure 4.1 shows the H6 thruster and a schematic of the cross-sectional view of the thruster. This figure indicates the centerlines of the cathode and the discharge channel, and the thruster exit plane. The cathode centerline (CL) is aligned with the axis of symmetry. Comparisons with experimental measurements used in this study are mainly performed along the CLs of the cathode and the discharge channel, and a few radial sweeps in the plume.

This study uses two different computational domains. For the comparisons between the prior model and the new model without the applied magnetic field (Section 4.4), the "effective" inflow domain is used, as proposed by Huismann when neglecting the magnetic field. If the standard discharge channel exit is used as an inflow when the magnetic field is neglected, the model over-predicted the plasma potential by 100 V in the near-field plume (Section 3.1). When the applied magnetic field is included, however, the standard discharge channel exit is used as an inflow to compare the new model with the magnetic field and without the magnetic field (Sections 4.3 and 4.4). Because the effective inlet eliminates the significance of the magnetic field effect, which is the strongest in the very near-field plume region, the magnetic field effect cannot properly be studied using the effective inlet.

4.1.2.1 "Effective" Inflow Domain when Neglecting the Magnetic Field Effects

A schematic of the computational domain of the H6 thruster plume using the effective inlet is shown in Fig. 4.2. The four main boundaries are labeled in this figure: the inflows from the cathode and channel, outflow, symmetry axis, and walls (thruster and keeper).

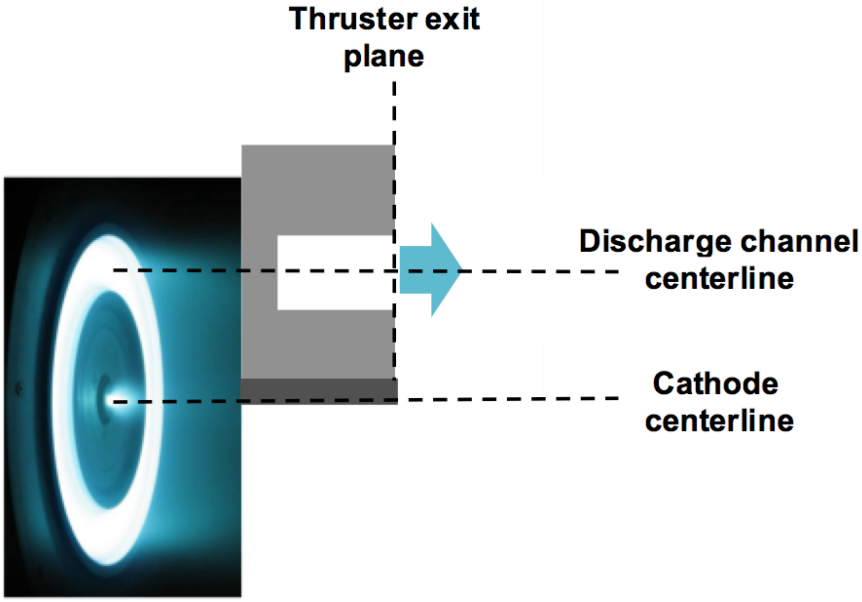

Figure 4.1: Cross-sectional view of the thruster indicating the centerlines of the cathode and discharge channel, and the thruster exit plane for the 2-D axisymmetric simulation.

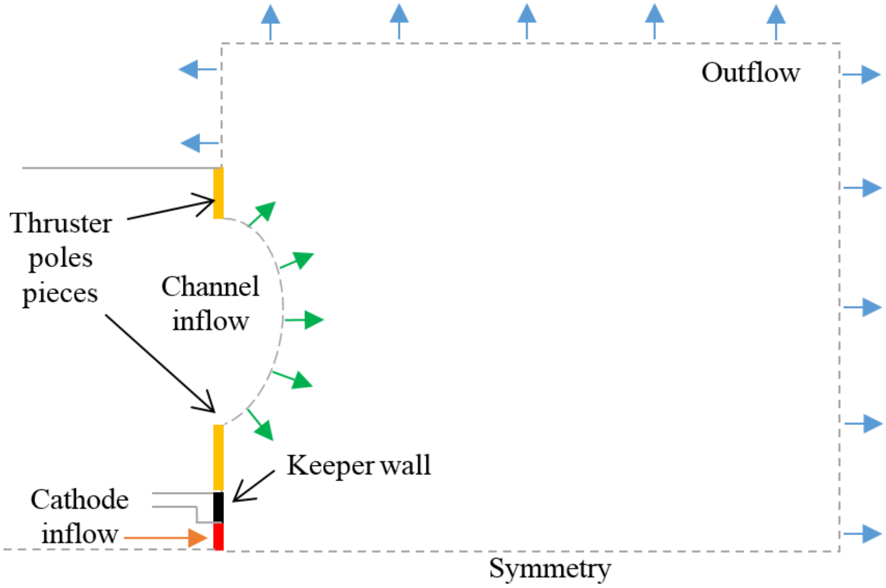

Figure 4.2: Schematic of the domain of the Hall thruster plume.

Figure 4.3 shows the HPHall computation domain, indicating both the thruster exit (TE) plane and the "B-field line," which is a magnetic field line. Although plume simulations usually start at the thruster exit plane, the B-field line was proposed to be used as an "effective" inlet by Huismann [7] to eliminate magnetic field effects from the plume simulation, because the prior version of MPIC ignores magnetic field effects. The magnetic field effects are strongest near the thruster exit plane, especially in the near-field plume of the discharge channel, and diminish rapidly away from the thruster exit plane.

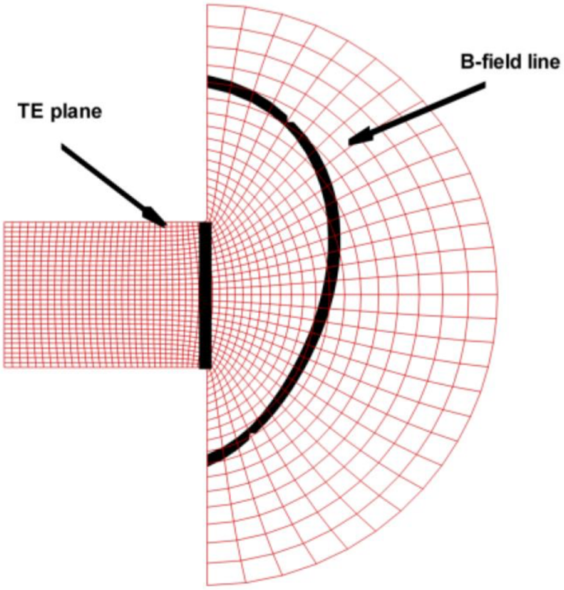

Figure 4.3: Magnetic field line in HPHall that is chosen as an "effective" inlet boundary for the plume simulation of the H6 Hall thruster.

The mesh used in the computational domain is shown in Fig. 4.4, where the domain spans 10 times the thruster diameter (D_{th}) in the axial (z) direction and 6 times the D_{th} in the radial (r) direction. The domain consists of a total of 1,996 triangular cells. The plume simulation runs for 450,000 timesteps to reach a steady state and then for another 200,000 timesteps to sample macroscopic data. The timestep size used is 4.0×10^{-8} s. In order to ensure a sufficient number of particles to reduce statistical noise, approximately 4.7 million particles are simulated.

Hall thruster plume simulations using the current model require boundary conditions to be specified at the inflow boundaries (i.e., cathode keeper exit and discharge

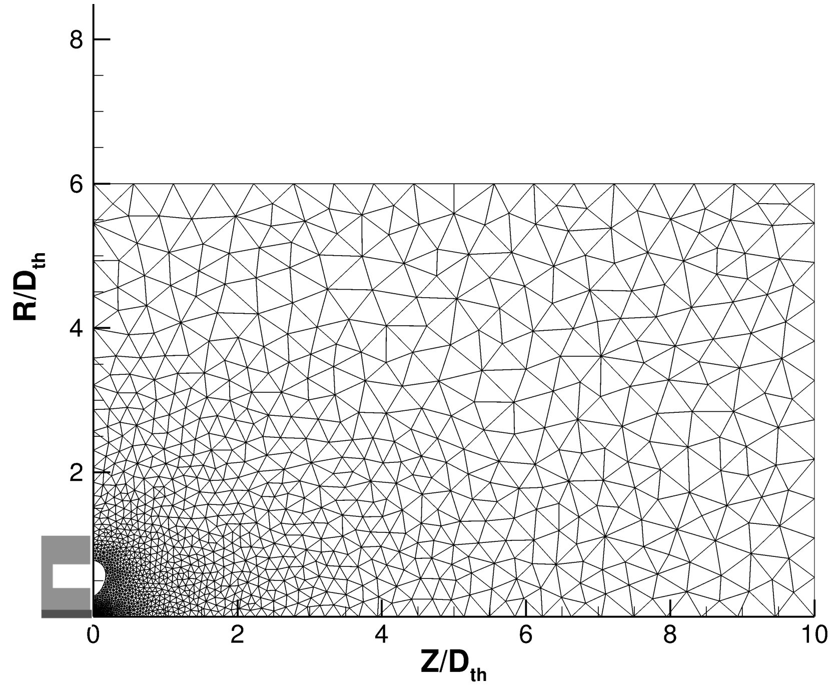

Figure 4.4: Computational domain of MPIC using the "effective" inlet and unstructured mesh.

channel exit), along the outer edges of, and along all walls in the computational domain. For the heavy species model (DSMC-PIC), the following parameters are required: velocities in z- and r-directions ($v_{z,i}, v_{r,i}$), species temperature (T_i) and species number density (n_i), where i ranges over each species that is modeled. For the electron model, plasma potential (ϕ), electron velocity stream function ($\nabla\psi$), and electron temperature (T_e) are necessary, where $\nabla\psi$ is calculated from electron current density (j_e) by using $\nabla\psi = -j_e/e$.

Since the plume structure strongly depends on the plasma conditions at the inflow boundary, it is important to get as accurate a condition as possible. In order to provide accurate boundary conditions at the channel and cathode inflows, the plasma simulation results from HPHall and OrCa2D are used. The inflow conditions at the effective inlet are provided by Huismann using HPHall (Tables 4.1 to 4.4 [7]). The effective inflow boundary is constituted by 15 line segments, S_1-S_{15}, in order to closely map onto the magnetic field line extracted from HPHall (Fig. 4.5).

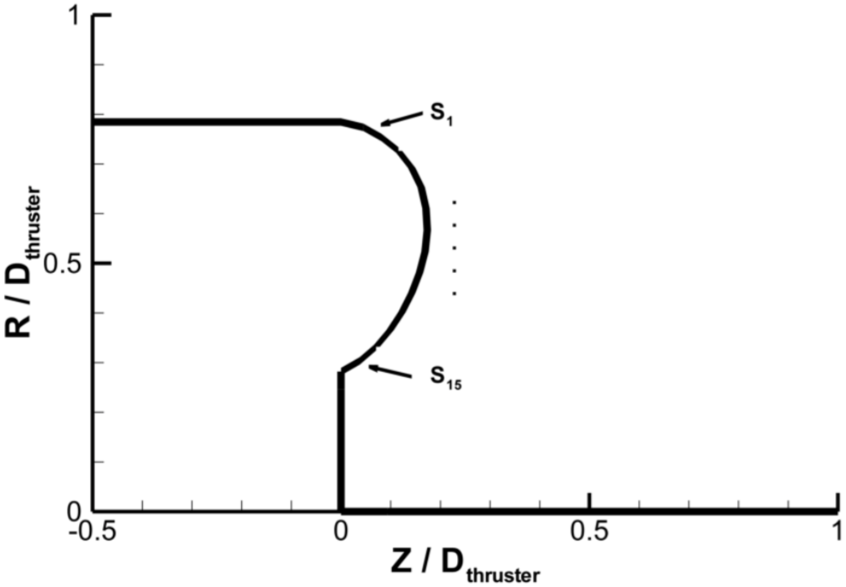

Figure 4.5: Proposed discharge channel inlet ("effective inlet") boundary by Huismann [7]. The boundary is constituted by 15 line secments, S_1-S_{15}

Table 4.1: Xe neutral parameters extracted from HPHall at the B-field shape inflow geometry [7]

Location	$u(m/s)$	$v(m/s)$	$T(K)$	$n(m^{-3})$
S_1	27.0	-33.0	400	2.88×10^{17}
S_2	23.0	-31.0	450	2.81×10^{17}
S_3	34.0	-9	650	2.91×10^{17}
S_4	165	56.0	1500	3.89×10^{17}
S_5	281	63.0	3100	4.40×10^{17}
S_6	309	27.0	5400	3.94×10^{17}
S_7	384	2.00	8250	3.58×10^{17}
S_8	660	-6.00	10100	3.38×10^{17}
S_9	449	-12.0	9700	3.44×10^{17}
S_{10}	430	-25.0	7700	3.80×10^{17}
S_{11}	411	-62.0	5450	4.47×10^{17}
S_{12}	352	-104	3150	4.58×10^{17}
S_{13}	67.0	-12.0	1250	2.39×10^{17}
S_{14}	47.0	17.0	680	2.45×10^{17}
S_{15}	59.0	23.0	550	2.71×10^{17}

Table 4.2: Xe^{+} parameters extracted from HPHall at the B-field shape inflow geometry [7]

Location	$u(m/s)$	$v(m/s)$	$T(K)$	$n(m^{-3})$
S_1	-1310	4250	7.17×10^4	4.46×10^{15}
S_2	830	6020	1.62×10^5	6.48×10^{15}
S_3	4620	7100	2.57×10^5	1.17×10^{16}
S_4	9480	6510	2.84×10^5	2.21×10^{16}
S_5	14200	4440	2.16×10^5	5.35×10^{16}
S_6	16400	1930	1.46×10^5	1.33×10^{17}
S_7	17300	160	1.22×10^5	2.58×10^{17}
S_8	18000	-660	8.58×10^4	3.27×10^{17}
S_9	17900	-1080	8.74×10^4	3.39×10^{17}
S_{10}	17000	-1730	1.19×10^5	2.99×10^{17}
S_{11}	15800	-3330	1.70×10^5	1.51×10^{17}
S_{12}	12200	-5520	2.51×10^5	6.30×10^{17}
S_{13}	6980	-7420	2.56×10^5	2.47×10^{17}
S_{14}	530	-5810	8.79×10^4	1.06×10^{17}
S_{15}	-1940	-4340	2.10×10^4	7.35×10^{17}

Table 4.3: Xe^{2+} parameters extracted from HPHall at the B-field shape inflow geometry [7]

Location	$u(m/s)$	$v(m/s)$	$T(K)$	$n(m^{-3})$
S_1	-1790	8340	1.10×10^5	3.76×10^{14}
S_2	1030	9980	1.90×10^5	5.62×10^{14}
S_3	5240	10330	3.02×10^5	9.47×10^{14}
S_4	11200	9300	4.22×10^5	1.87×10^{15}
S_5	17200	6440	4.47×10^5	4.59×10^{15}
S_6	21200	2950	3.46×10^5	1.29×10^{16}
S_7	22900	300	2.73×10^5	3.14×10^{16}
S_8	23700	-930	2.17×10^5	4.82×10^{16}
S_9	23500	-1660	2.23×10^5	4.87×10^{16}
S_{10}	22000	-2630	3.12×10^5	6.40×10^{16}
S_{11}	19300	-4640	4.24×10^5	1.43×10^{16}
S_{12}	14000	-7610	4.92×10^5	5.47×10^{15}
S_{13}	6780	-9670	3.87×10^5	2.34×10^{15}
S_{14}	470	-8800	2.17×10^5	1.25×10^{15}
S_{15}	-2960	-6810	1.40×10^5	9.10×10^{14}

The same conditions for both the heavy species model and the electron model are required at the cathode inflow boundary. The discharge plasma from the cathode is

Table 4.4: Electron parameters extracted from HPHall at the B-field shape inflow geometry [7]

Location	$\phi(V)$	$\nabla\psi(m^{-2}s^{-1})$	$T_e(eV)$
S_1	5.10	-4.11×10^{20}	6.05
S_2	6.10	-8.43×10^{20}	6.12
S_3	8.50	-1.82×10^{21}	6.08
S_4	12.3	-1.82×10^{21}	6.07
S_5	17.6	-2.79×10^{21}	6.08
S_6	23.3	-2.72×10^{20}	6.04
S_7	27.3	5.55×10^{21}	6.09
S_8	29.1	1.49×10^{22}	6.04
S_9	29.5	1.01×10^{22}	6.13
S_{10}	27.5	6.26×10^{21}	6.21
S_{11}	23.5	9.09×10^{19}	6.11
S_{12}	18.2	-1.64×10^{21}	6.04
S_{13}	13.2	-1.01×10^{21}	6.01
S_{14}	8.10	-7.93×10^{20}	6.07
S_{15}	6.20	-3.15×10^{20}	5.94

coupled to the plume simulation at the exit plane of the cathode keeper shown in Fig. 4.6. using OrCa2D [23]. OrCa2D is a full-fluid cathode code developed at JPL, which solves conservation laws for partially-ionized plasma in the cathode. Figure 4.6 shows a contour plot of the plasma potential calculated by OrCa2D. The computation region includes the emitter, orifice, keeper, and plume of the cathode. The simulation

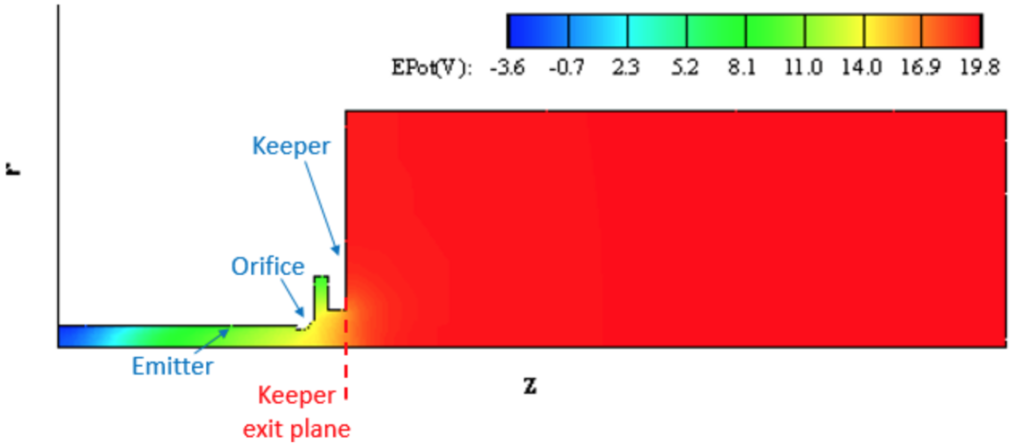

Figure 4.6: Contour plots of the plasma potential calculated by OrCa2D.

was performed at 20 A of discharge current with a slight off-nominal condition for the cathode mass flow fraction of 5% anode flow; whereas the nominal operating condition of the H6 Hall thruster is 20 A with the cathode mass flow fraction of 7% anode flow. Magnetic field effect was neglected in this particular simulation.

Figure 4.7 shows profiles of the electron model, plasma potential, electron temperature, and electron current density ($\nabla\psi = -j_e/e$) extracted at the keeper exit plane from OrCa2D. OrCa2D calculates the plasma potential with respect to the cathode potential, so the cathode to ground voltage (V_{cg} = -13 V) is accounted for when using the value for MPIC and the experimental measurement. For heavy species conditions, the velocity, temperature, and number density of each species are extracted.

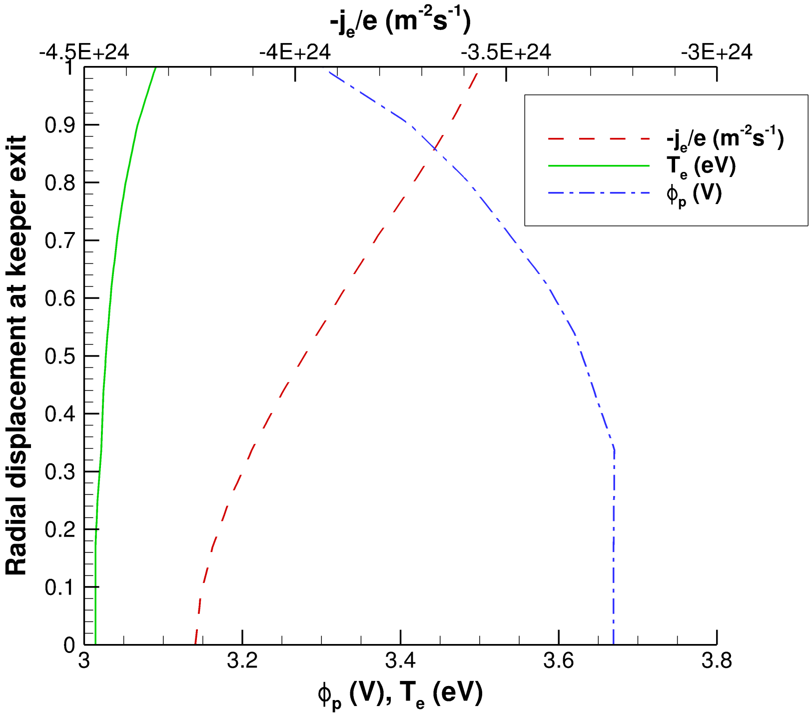

Figure 4.7: Profiles of the plasma potential (ϕ), electron temperature (T_e), and electron stream function (-j_e/e) calculated by OrCa2D along the keeper exit plane for the inlet conditions in MPIC.

In MPIC, the keeper exit plane is divided into two equal-length cells (i.e., K_1 and K_2) to represent radial variation of inflow properties, which is shown in Fig. 4.8.

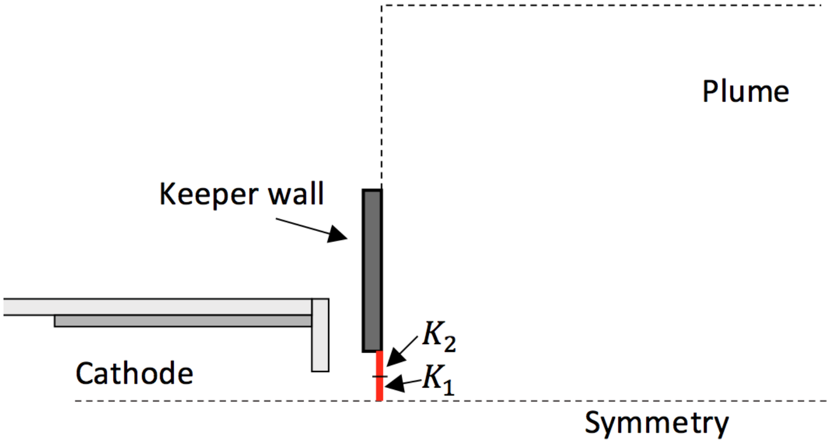

Figure 4.8: Schematic of cathode inflow boundary that consists of 2 equal-length cells K_1 and K_2.

These properties are averaged across each cell. The heavy species parameters at the keeper exit are summarized in Table 4.5, and the electron parameters are summarized in Table 4.6.

Table 4.5: Heavy species parameters extracted from OrCa2D [23] at the cathode keeper exit plane

Species	Location	$u(m/s)$	$v(m/s)$	$T(K)$	$n(m^{-3})$
Xe	K_1	282	35.5	935	3.52×10^{20}
	K_2	363	32.3	1070	3.40×10^{20}
Xe^+	K_1	1260	1200	935	1.76×10^{19}
	K_2	1320	667	1070	2.28×10^{19}

Table 4.6: Plasma parameters extracted from OrCa2D at the discharge channel exit plane [23]

Species	Location	$\phi(V)$	$\nabla\psi(m^{-2}s^{-1})$	$T_e(eV)$
e^-	K_1	3.42	-3.70×10^{24}	3.06
	K_2	3.65	-4.13×10^{24}	3.03

4.1.2.2 Discharge Channel Exit Inflow Domain when Including the Magnetic Field Effects

For the simulation of the new model with the applied magnetic field, the discharge channel exit is used as an inflow boundary to couple the plasma flow from the anode to the plume simulation. A schematic of the 2-D axisymmetric simulation domain of the H6 Hall thruster plume is shown in Fig. 4.9. Four main types of boundaries are labeled in the figure: 1) inflows from the cathode and channel, 2) outflow, 3) symmetry axis, and 3) walls (thruster and keeper).

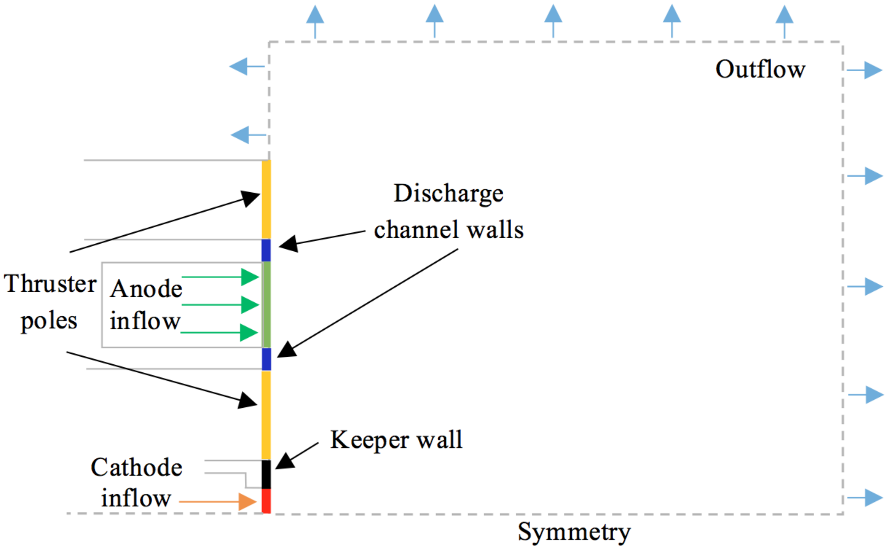

Figure 4.9: Schematic of the computational domain of the Hall thruster plume using the discharge channel exit as an inflow boundary.

At the discharge channel exit boundary, the plasma potential values provided by Huismann [7] were approximately 70 V higher than the actual measurement that is used for comparisons in the current study. Therefore, the H6 simulation was re-run using HPHall, and the inflow boundary conditions were extracted at 0.5 mm upstream of the actual thruster exit plane in order to match the same plasma potential value to the experimental data measured by Sekerak [47]. The discharge channel inflow boundary is constituted by ten equal-length segments to allow radial variation. The new inflow conditions at the discharge channel exit plane are summarized in Tables 4.7 and 4.9.

Table 4.7: Xe parameters extracted from HPHall at 0.5 mm upstream of the discharge channel exit as an inflow boundary.

Location	$u(m/s)$	$v(m/s)$	$T(K)$	$n(m^{-3})$
S_1	266	66.0	472	4.06×10^{18}
S_2	279	128	546	2.20×10^{18}
S_3	286	156	619	1.16×10^{18}
S_4	289	137	753	6.62×10^{17}
S_5	288	49.0	883	4.53×10^{17}
S_6	292	-76	864	4.69×10^{17}
S_7	294	-146	726	6.93×10^{17}
S_8	287	-155	622	1.23×10^{18}
S_9	277	-119	559	2.29×10^{18}
S_{10}	261	-54.0	508	4.20×10^{18}

Table 4.8: Xe^+ parameters extracted from HPHall at 0.5 mm upstream of the discharge channel exit as an inflow boundary.

Location	$u(m/s)$	$v(m/s)$	$T(K)$	$n(m^{-3})$
S_1	12368	-2263	68000	1.64×10^{17}
S_2	13723	-279	43148	2.91×10^{17}
S_3	14575	4.00	28822	3.77×10^{17}
S_4	15128	-139	17530	4.26×10^{17}
S_5	15210	-309	12421	4.62×10^{17}
S_6	14935	-515	32186	4.57×10^{17}
S_7	14139	-578	19068	4.29×10^{17}
S_8	12976	-419	27694	3.80×10^{17}
S_9	11579	288	41536	2.98×10^{17}
S_{10}	10055	2477	59646	1.62×10^{17}

The same cathode conditions are applied as for the effective inlet simulations (Tables 4.5 and 4.6).

Table 4.9: Xe^{2+} parameters extracted from HPHall at 0.5 mm upstream of the discharge channel exit as an inflow boundary.

Location	$u(m/s)$	$v(m/s)$	$T(K)$	$n(m^{-3})$
S_1	14426	-2393	129764	8.52×10^{15}
S_2	17097	-144	115005	1.64×10^{16}
S_3	18347	146	104483	2.87×10^{16}
S_4	19076	-148	87235	4.12×10^{16}
S_5	19131	-427	76155	5.06×10^{16}
S_6	18755	-759	95419	4.92×10^{16}
S_7	17621	-896	86492	3.99×10^{16}
S_8	15974	-740	94358	2.76×10^{16}
S_9	13921	135	107717	1.60×10^{16}
S_{10}	11347	2673	112883	7.70×10^{15}

4.2 Comparison of the Prior and New Models Without the Magnetic Field Effect

In this section, the simulation results from the new model without the applied magnetic field are compared with the results from the prior model using the effective inlet. The purpose of these comparisons are to examine the differences between the prior and the new model when there is no applied magnetic field. As described in Section 3.2, the left-hand side of the momentum conservation equation in the prior model and the new model are equivalent when the applied magnetic field is zero (Eq. 3.16). In this section, comparisons between the two models are made through examining the following macroscopic plasma properties: plasma potential, electron temperature, electron number density, and ion current density.

4.2.1 Plasma Potential

The contour plots of the plasma potential in the plume calculated by both models are compared in Fig. 4.10. While the plasma potential variation in the plume is about 26 V for both models, the new and the existing models predict slightly different structure. In the new model, the plasma potential is highest in the region just downstream of the discharge channel and decreases relatively quickly in the axial direction to the far-field plume potential of approximately 22.5 V. In comparison, the prior model predicts very gradually decreasing plasma potential from the discharge channel exit to the far-field plume. This difference appears to be more clear from the axial plasma potential profiles along the channel in Fig. 4.11. While the new model shows the negative gradient in potential at the very near-field plume ($Z/D_{th} < 0.5$), the prior model predicts very low gradient in the plasma potential.

Figure 4.12 shows the plasma potential profiles along the axis of symmetry, or the cathode centerline ($R/D_{th} = 0$). The plasma potential calculated by the prior model increases more rapidly than the new model, reaching its peak potential at $Z/D_{th} = 2$. As the axial displacement increases, the new model reaches nearly-constant far-field potential value, while the potential calculated by the prior model gradually decreases until the far-end of the computational domain ($Z/D_{th} = 10$).

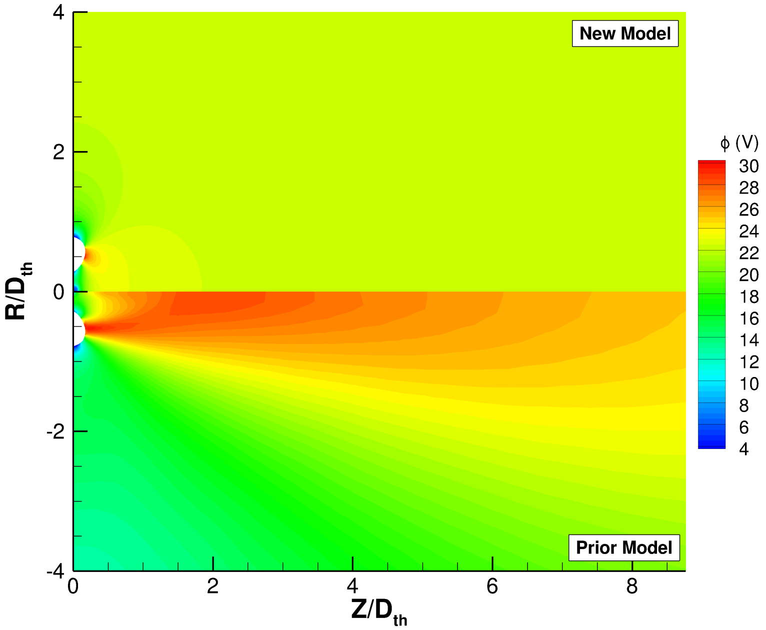

Figure 4.10: Contour plots of the plasma potential: new electron model (top) and prior model (bottom). The magnetic field effect is neglected.

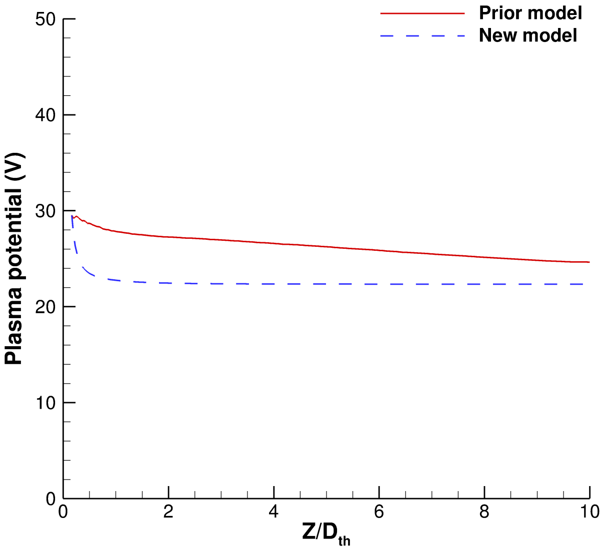

Figure 4.11: Axial plasma potential profiles along the cathode CL ($Z/D_{th} = 0$) and the discharge channel CL ($Z/D_{th} = 0.5$), comparing the prior and new model when the magnetic field is neglected.

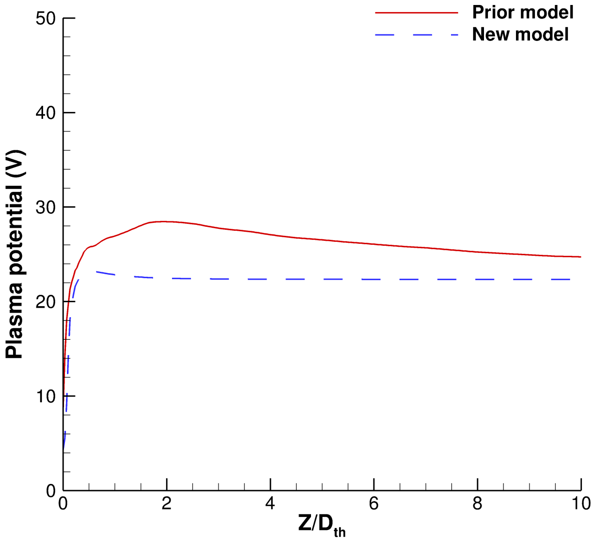

Figure 4.12: Axial plasma potential profiles along the cathode CL ($Z/D_{th} = 0$) and the discharge channel CL ($Z/D_{th} = 0.5$), comparing the prior and new model when the magnetic field is neglected.

4.2.2 Electron Temperature

The contour plots of the electron temperature in the plume are compared in Fig. 4.13 in the case of zero magnetic field. Both models predict almost the same electron temperature fields in the entire domain.

The magnetic field affects the plasma potential, which then affects the electric field. When the magnetic field effect is neglected, however, this effect on the electric field is very small because the plasma potential gradient in the plume is small. Both models show that the electron temperature decreases smoothly in all directions. The temperature variation in the plume is about 4 eV. The electron temperature in the cathode plume starts at a lower value and then increases rapidly, with the maximum temperature occurring at $Z/D_{th} = 0.15$.

Figure 4.14 shows the axial profiles of the electron temperature along the discharge channel centerline. Both models predict monotonically decreasing electron

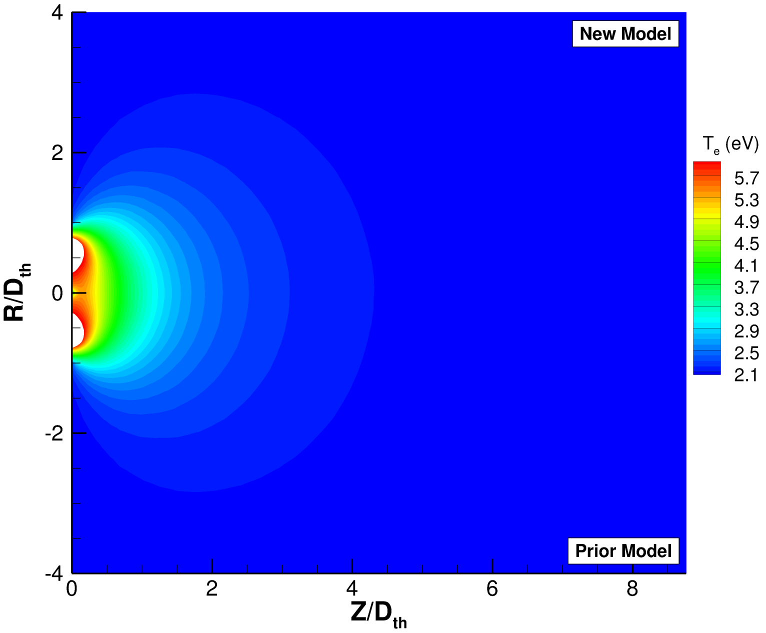

Figure 4.13: Contour plots of the electron temperature: new electron model (top) and prior model (bottom). The magnetic field is neglected.

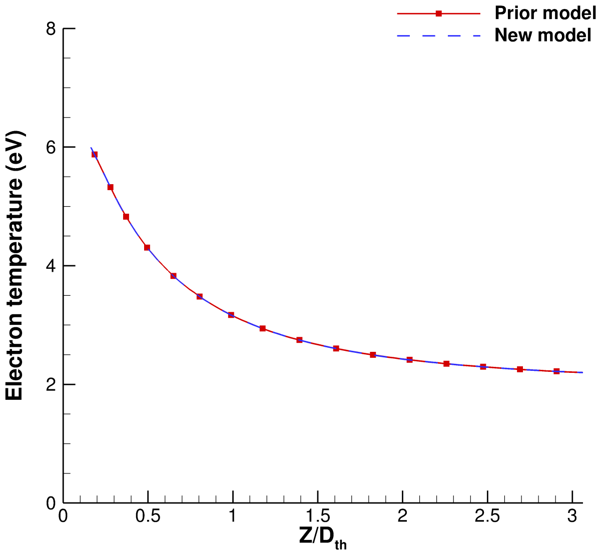

Figure 4.14: Axial electron temperature profiles along the discharge channel centerline, comparing the prior and new model when the magnetic field is neglected.

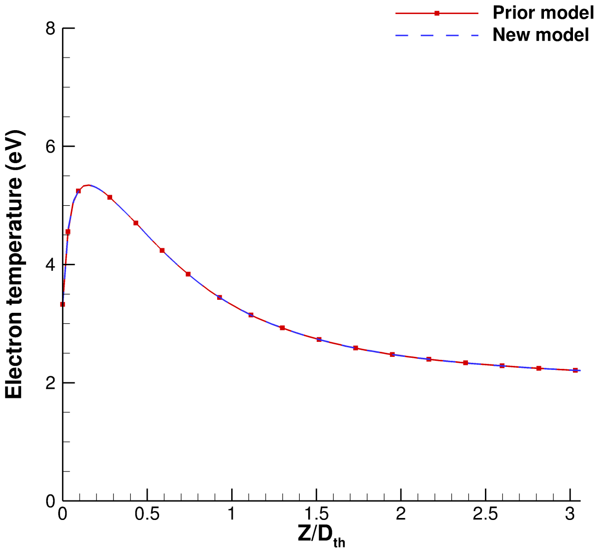

Figure 4.15: Axial electron temperature profiles along the cathode centerline, comparing the prior and new model when the magnetic field is neglected.

temperature along the discharge channel centerline. Figure 4.15 shows the electron temperature profiles along the cathode centerline. The electron temperature increases rapidly as the flow expands out from the cathode inflow, and then decreases monotonically in the increasing axial displacement. The electron temperature profiles along the the cathode centerline reach the same value as the axial displacement increases.

4.2.3 Electron Number Density

Figure 4.16 compares the electron number density contours calculated by both models. These models show very similar contours throughout the entire domain except small difference in the cathode plume. The highest electron density is shown at the cathode plume (on the order of 10^{19} m^{-3}). The density at the cathode plume decreases very quickly as the flow diffuses into the plume; the density decreases about two orders of magnitudes in $Z/D_{th} = 0.1$. In comparison, the density drop along the discharge channel centerline is not as rapid as the cathode centerline because the effective inlet shape neglects the region closest to the thruster exit plane.

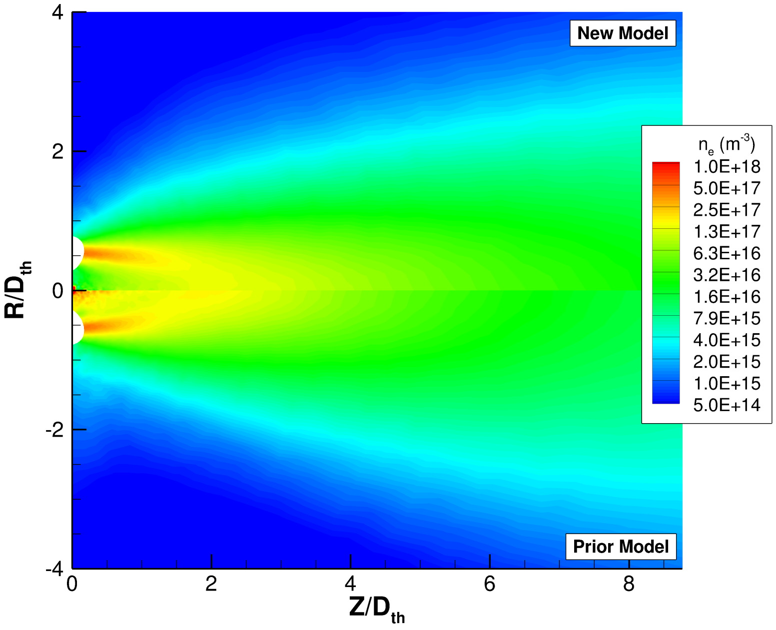

Figure 4.16: Contour plots of the electron number density: new electron model (top) and existing model (bottom)

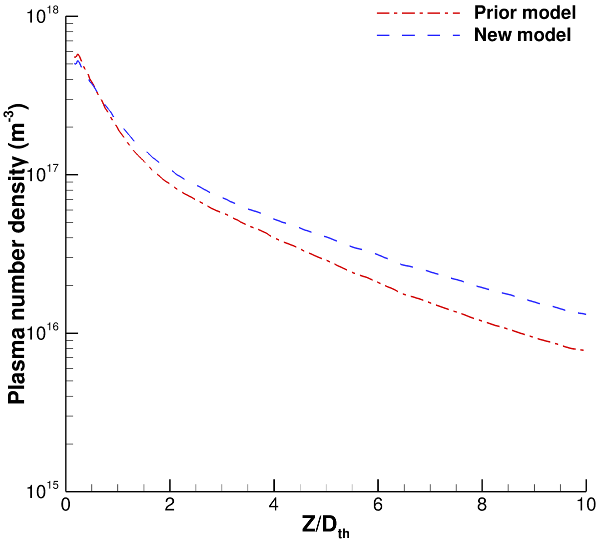

Figure 4.17: Axial electron number density profiles along the discharge channel centerline.

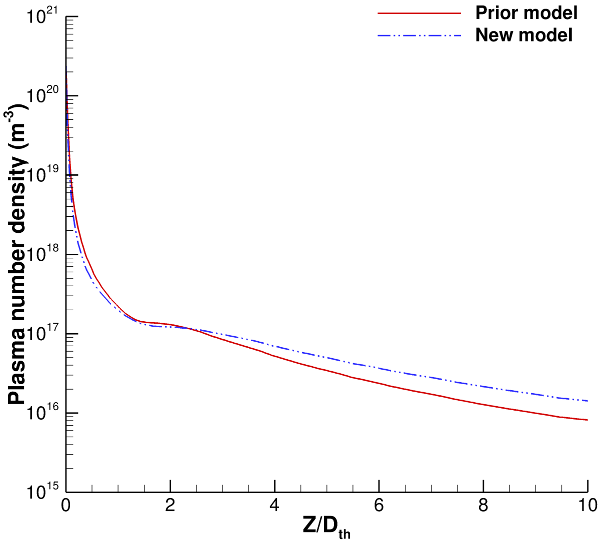

Figure 4.18: Axial electron number density profiles along the cathode centerline.

The axial profiles of the electron density along the cathode and discharge channel centerlines are shown in Fig. 4.18. The new model shows slightly larger gradient in the very near-field of the cathode than the existing model. As the axial displacement increases, the electron density along the cathode centerline increases slowly as the cathode flow meets with the ion beam from the discharge channel at about 1 thruster diameter downstream. Both models predict very similar electron density at the discharge channel centerline.

4.2.4 Ion Current Density

Figure 4.19 shows contours of ion current density calculated by both the new and prior models. Similar to the electron number density, the highest ion current density occurs at the cathode exit and near the center of discharge channel inlet. The ion current from cathode and channel meet at the cathode centerline at approximately 1 to 2 thruster diameter downstream (i.e., $Z/D_{th} = 1$ to 2). At this location, the existing model predicts slightly higher ion current density than the new model does.

Figure 4.21 shows the axial ion current density profiles at the cathode centerline.

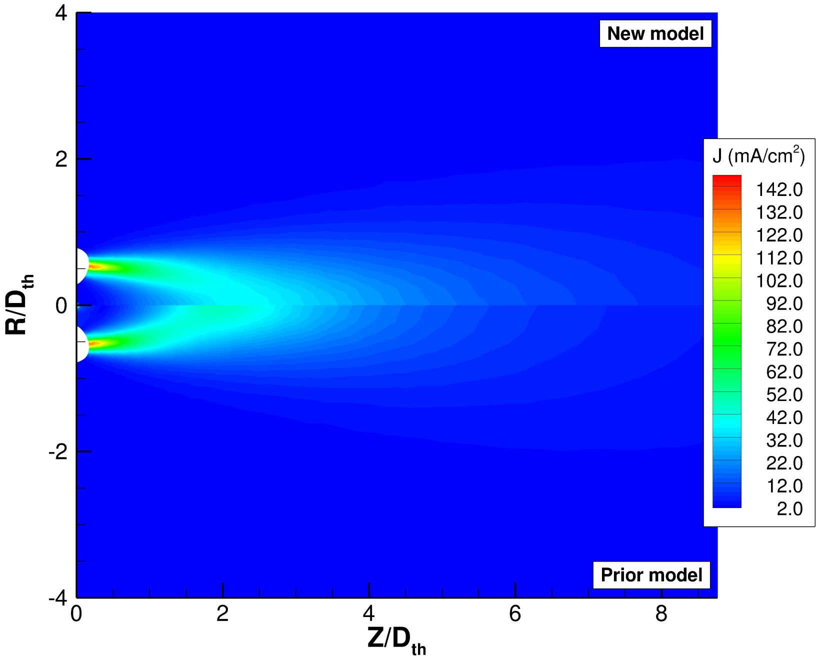

Figure 4.19: Contour plots of the ion current density: new electron model (top) and existing model (bottom).

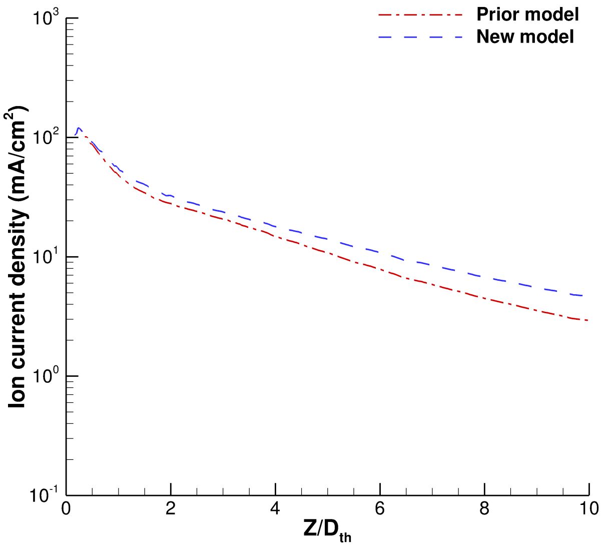

Figure 4.20: Axial ion current density profiles along the discharge channel CL, comparing the prior model and the new model.

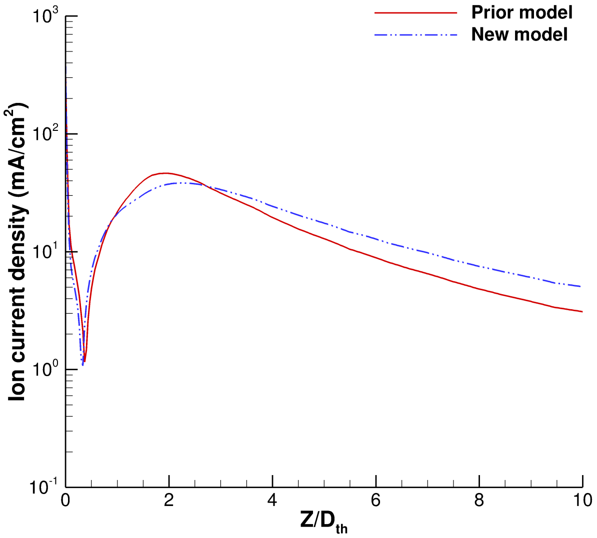

Figure 4.21: Axial ion current density profiles along the cathode CL, comparing the prior model and the new model.

As the flow expands out from the cathode, the ion current density along the cathode centerline rapidly decreases, with the lowest current density at about $Z/D_{th} = 0.2$ for the new model and $Z/D_{th} = 0.4$ the existing model. Downstream of these locations, the ion current densities increase back as the axial displacement increases. Despite the location of the lowest ion current density, the overall profiles look very similar. The profile along the channel centerline decreases gradually, varying approximately 90 mA/cm^2 from Z/D_{th} =0 to 3. Both models also predict similar profiles of the ion current densities along the channel centerline (Fig. 4.20). The ion current density calculated by the new model is slightly higher than the prior model.

4.2.5 Discussion

Although the new and the prior models solve the same LHS of the governing equation when the applied magnetic field is zero, the plasma potential structure are moderately different due to different numerical schemes used in both models. The new model puts the governing equation directly into a weak form and discretize using the continuous Galerkin method. In comparison, the prior model estimates derivatives of the source terms and add them to result in the linear forcing function, which is then discretized by the continuous Galerkin method. Numerical errors can truncate by using the least-squares method to estimate the derivatives to determine $f(x, y)$ in Eq. 2.22.

For qualitative comparisons with experimental measurement, the axial profiles of the plasma potential are compared with experimental measurement by Sekerak [47] in Figs. 4.22 and 4.23. Along the discharge channel centerline (4.22), a large plasma potential gradient is observed from the experimental measurement. While the new model can capture the gradient in plasma potential at the very near-field plume of the channel, the existing model cannot capture the gradient. In Fig. 4.23, as the axial displacement increases, the plasma potential data also increases rapidly in the very near-field plume of the cathode. The potential then reaches the far-field potential that is nearly constant. The overall profile shapes are similar between the models and the measurement. However, the new model shows more constant plasma potential value than the existing model. Both models does not well capture the location where the depressed cathode potential starts increasing near the cathode exit.

While the new model and the existing model predict a slightly different structure of the plasma potential in the plume, the remaining properties are not affected by much. The slightly large plasma potential gradient at the very near-field plume of the discharge channel is not sufficient to affect the electron number density and the ion current density. The existing model shows slightly elevated ion current density along the cathode centerline at about $Z/D_{th} = 2$, and this is due to the slightly increase plasma potential at this location that decreases further downstream, accelerating ions at this location.

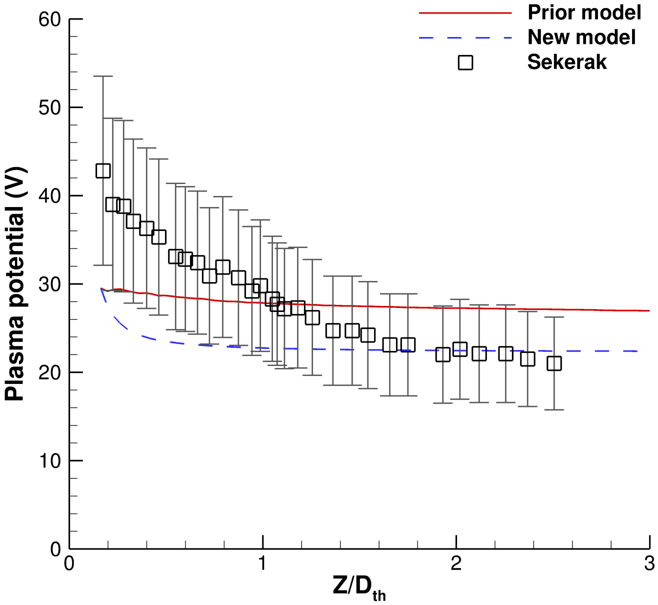

Figure 4.22: Axial plasma potential profiles along the discharge channel centerline, comparing the prior and the new models with the experimental data from Sekerak [47].

The new model without the applied magnetic field using the effective inlet provides good agreement with measured plasma potential. In addition, adding the magnetic

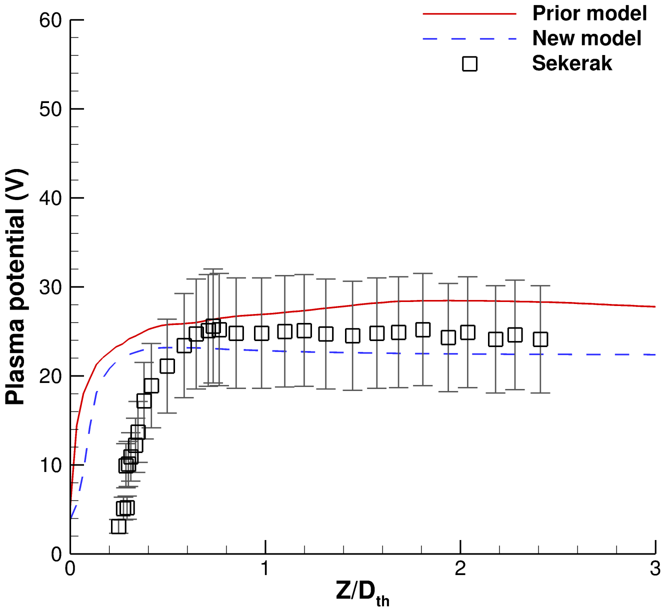

Figure 4.23: Axial plasma potential profiles along the cathode centerline, comparing the prior and the new models with the experimental data from Sekerak [47].

field effects in the new model does not require additional computational time, because the new model does not use the least-squares method to calculate derivatives, which requires additional computational time for the prior model.

4.3 Electron Mobility Modeling

This section presents simulation results using the new electron model with magnetic field effects. Including magnetic field effects requires modeling of the cross-field, or "anomalous" electron mobility. First, background on anomalous electron mobility modeling is provided. Then, a parametric study of the anomalous mobility coefficient is presented.

4.3.1 Background on Anomalous Electron Mobility Modeling in Hall Thrusters

The transport of electrons across magnetic field lines in a Hall thruster is partially controlled by the collisions with heavy species, known as the "classical" mechanism of transport. However, diffusion through classical collisions alone is not sufficient to reproduce the cross-field mobility of electrons observed experimentally. The cross-field diffusion of electrons is known to be enhanced by plasma turbulence and instability [49], which is a mechanism described as the "anomalous" transport. Since the anomalous electron transport is still not well-understood, the electron mobility is modeled using an anomalous Bohm collision frequency, defined as the classical Bohm collision frequency with a coefficient α_e:

$$\nu_B = \frac{\alpha_e}{16}\omega_g \tag{4.1}$$

where α_e is the anomalous Bohm coefficient used as a free parameter to match experimental data, and ω_g is the electron gyro-frequency. For the classical Bohm diffusion case, $\alpha_e = 1$.

Although a constant anomalous Bohm coefficient can be used throughout the entire computational domain, multiple-region mobility modeling has been developed over time [50, 51, 22, 52], to account for spatial variation in the anomalous mobility coefficient. In the case of the state-of-the-art Hall thruster code, HPHall, the first version of the code developed by Fife [20] used a single mobility coefficient over the entire computational domain. Then, two-region mobility modeling was implemented by Hagelaar [50] and Koo [51], and eventually three-region mobility was implemented by Hofer [22] to increase the fidelity of the model. Hofer [22] shows that there are at least three distinct regions from the anode to the near-field plume of Hall thrusters, labeled in I, II, and III in Fig. 4.24. These regions are divided according to the shape and magnitudes of the measured plasma potential profile and the calculated Hall parameters along the centerline of the discharge channel. The current version of HPHall, thus, uses a three-region mobility model, divided into the near-anode region, thruster exit region, and very near-field plume region. Although these three regions clearly show different behaviors from Fig. 4.24, it is still unclear how the anomalous mobility coefficient actually changes spatially. Moreover, the computational domain of HPHall includes only up to the near-field plume with zero-mobility coefficient beyond a near-cathode magnetic field line, which is only couple centimeters away from the thruster exit plane. Therefore, it is not clear what the coefficient should be beyond the very near-field plume (closed to the thruster exit) and the cathode plume region.

For the electron mobility modeling of the H6 thruster, Hofer [22] used high Bohm values of $\alpha_e = 1$ and 10 in the plume using HPHall, whereas Mikellides [53] used lower values of $\alpha_e = 0.15$ and 0.075 using Hall2De—a full-fluid code developed at JPL. Since all models simulate different computational domains with different physical and numerical models, different values are used in different models. In the remainder of this section, a parametric study of the anomalous Bohm mobility coefficient is presented.

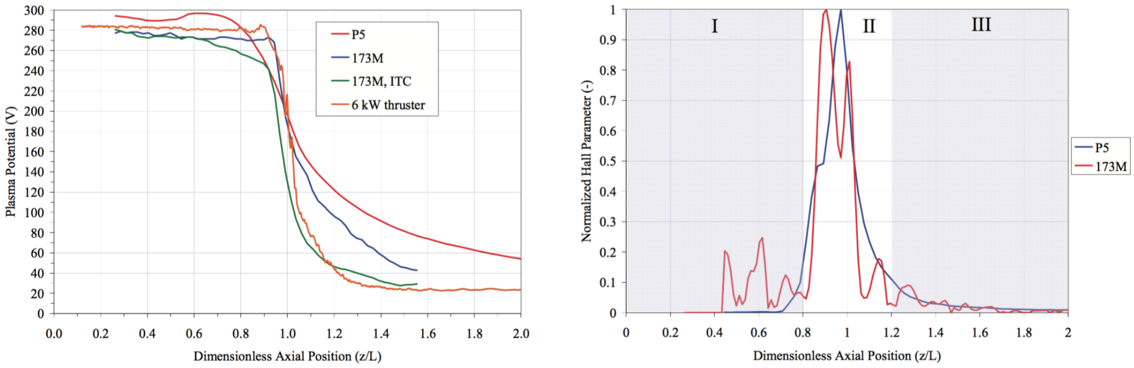

Figure 4.24: Figures taken from Ref. [22] to show three distinct regions for electron mobility modeling. Left: Experimental data showing the axial variation of the plasma potential on the discharge channel centerline of the P5, NASA-173M, NASA-173M with internal trim coil (ITC), and a 6 kW laboratory thruster. Right: Axial variation of the Hall parameter computed from experimentally measured plasma properties, normalized to its maximum value, on the discharge channel centerline of the P5 and the NASA-173M.

4.3.2 Effect of the Anomalous Bohm Coefficient on Plasma Properties

To study the effect of the anomalous Bohm coefficient on plasma properties in the plume, the following values are simulated: $\alpha_e = 10, 5, 1, 0.5, 0.2, 0.1,$ 0.05, 0.01, and 0.001. The present study uses a constant value of α_e throughout the entire computational domain.

Figure 4.25 shows the axial profile of anomalous Bohm collision frequencies along the centerline of the discharge channel. The Bohm collision frequency has its highest value near the thruster exit plane (Z/D_{th}) and decreases exponentially downstream, because the strength of the magnetic field also decreases downstream in the same manner. As the value of α_e decreases, the magnitudes of the Bohm collision frequency profiles also decrease monotonically. This trend is expected since the Bohm frequency is linearly proportional to α_e according to Eq. (4.1). A similar trend is observed in the axial profile of the Bohm collision frequencies along the cathode centerline in Fig. 4.26. A sudden decrease and subsequent increase in ν_B is observed at about

$Z/D_{th} = 2.35$, which is caused by the magnetic field separatrix occurring at this location along the cathode centerline (Fig. 3.3). The small bumps shown in the ν_{ei} and ν_{en} curves are likely due to numerical errors in the particle weighting schemes.

The values chosen for α_e determines the different collision mechanisms (i.e., classical vs. Bohm) that dominate the electron physics. To demonstrate this, relatively high ($\alpha_e = 5.0$) and low ($\alpha_e = 0.01$) Bohm coefficients are chosen, and their Bohm collision frequencies are compared with the classical collision frequencies in Figs. 4.27 and 4.28. Classical collision frequencies include electron-neutral (ν_{en}) and electron-ion (ν_{ei}) collisions. Figure 4.27 shows that the total collision frequency in the entire domain is dominated by the anomalous Bohm frequency when using $\alpha_e = 5.0$. In the case of small Bohm coefficient (Fig. 4.28), the Bohm frequency is still dominant in the very near-field plume region, while the electron-ion collision frequency dominates downstream of $Z/D_{th} = 0.85$.

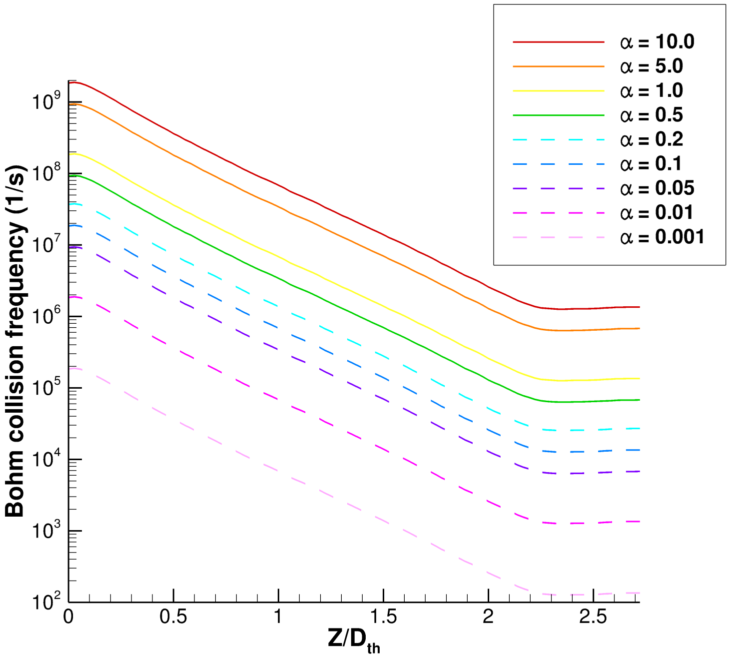

Figure 4.25: Axial profiles of anomalous Bohm collision frequency along the discharge channel centerline using various mobility coefficients α_e.

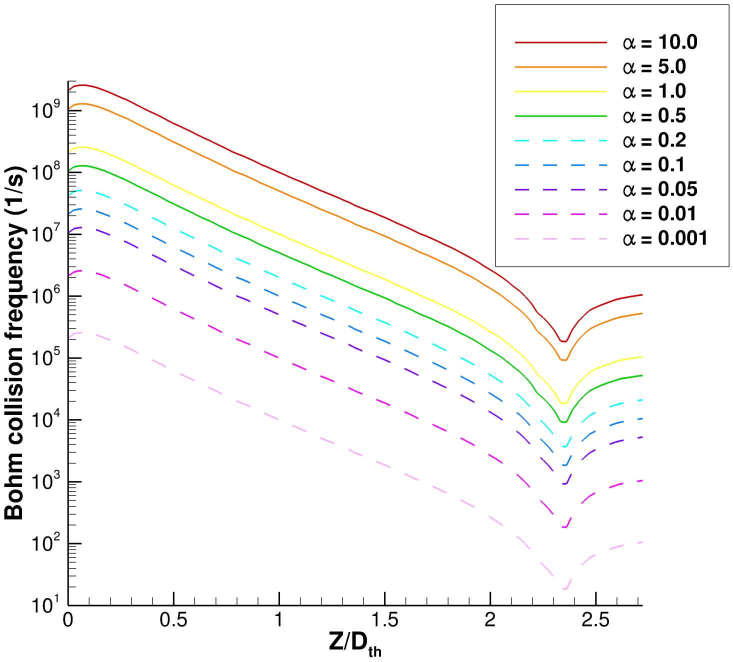

Figure 4.26: Axial profiles of anomalous Bohm collision frequency along the discharge channel centerline using various mobility coefficients α_e.

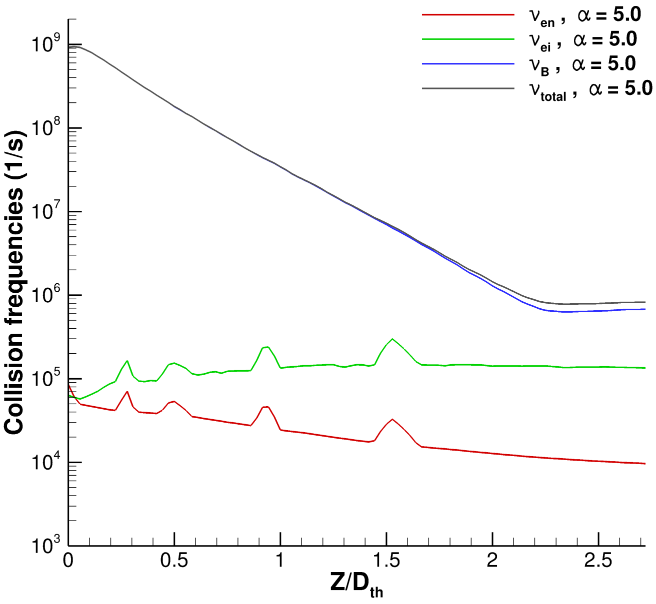

Figure 4.27: Axial profiles of electron collision frequencies along the discharge channel centerline using a high Bohm coefficient ($\alpha_e = 5.0$).

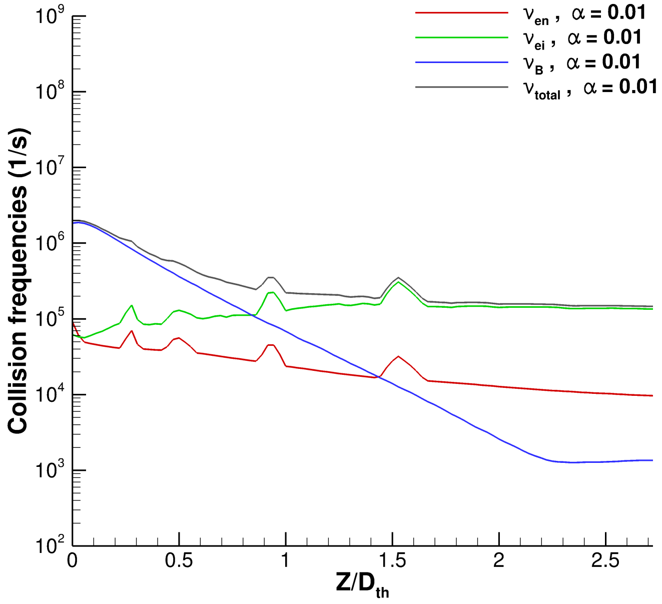

Figure 4.28: Axial profiles of electron collision frequencies along the discharge channel centerline using a low Bohm coefficient ($\alpha_e = 0.01$) .

The total electron collision frequency influences the shape and magnitude of electron mobility. The electron mobility calculated along the centerlines of the discharge channel and the cathode using various Bohm coefficients are shown in Figs. 4.29 and 4.30, respectively. The magnitude of the electron mobility is much smaller when α_e is larger, because the Bohm collision frequency is inversely proportional to the electron mobility ($\mu_e \propto 1/\nu_B$) for small to intermediate values of the magnetic field. In Fig. 4.29, the mobility is suppressed along the discharge channel centerline due to relatively high Bohm collision frequency. For instance when $\alpha_e = 5.0$, the electron mobility is very low from $Z/D_{th} = 0$ to 1.0, and then increases gradually downstream. For smaller values of α_e, the electron mobility increases throughout the domain. Especially for $\alpha_e < 0.1$, the shape of the mobility profiles in the very near-field plume becomes different than those at higher values of α_e. For example, when $\alpha_e = 0.01$, the electron mobility shows a noticeable peak near $Z/D_{th} \approx 0.85$, which is the location where classical collision starts to dominate the total electron collision as previously shown in Fig. 4.28. Along the cathode centerline shown in Fig. 4.30, the electron mobility in the very near-field plume is still relatively low even with the smallest Bohm coefficient used in this study ($\alpha_e = 0.001$), because the magnetic field is stronger in the near-field plume than the far-field plume.

Figure 4.31 shows the plasma potential profiles along the discharge channel centerline using various α_e values. The main differences among these profiles are the slopes of the plasma potential drop in the very near-field plume region ($Z/D_{th} < 0.2$) and the far-field plume potential value at an increasing Z/D_{th}. For moderate to high Bohm coefficients ($\alpha_e = 0.2$ to 10, shown in solid lines), the decreasing value of α_e increases the plasma potential gradient in the near-field plume and decreases the values of the far-field plume potential. For smaller coefficients ($\alpha_e = 0.01$ to $\alpha_e = 0.1$, shown in dashed lines), decreasing the value of α_e results in a decreased plasma potential

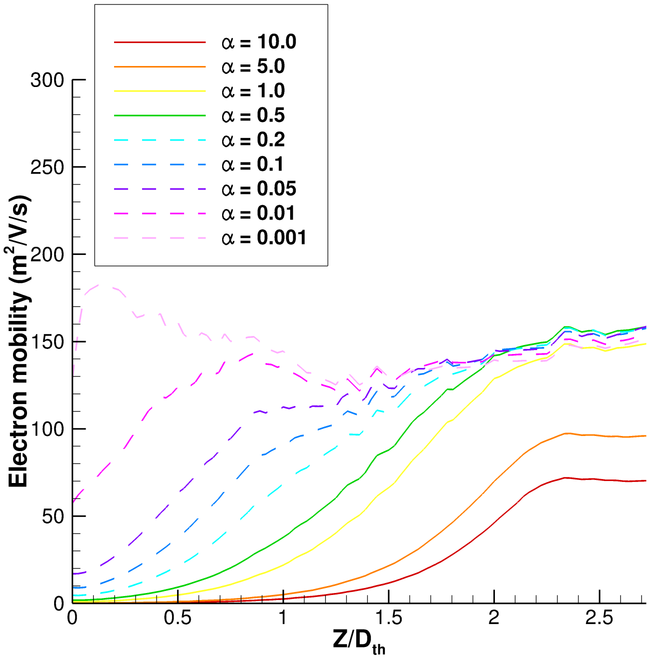

Figure 4.29: Axial profiles of the electron mobility along the discharge channel centerline using various mobility coefficients.

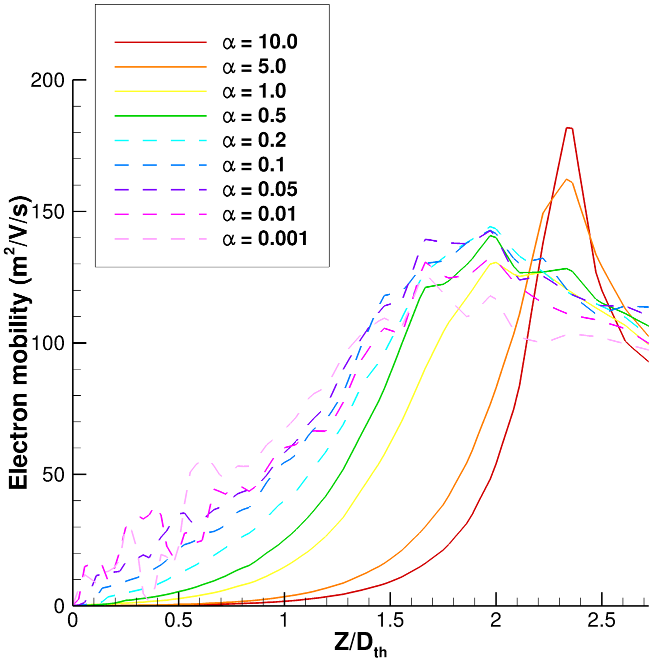

Figure 4.30: Axial profiles of the electron mobility along the cathode centerline using various mobility coefficients.

gradient in the near-field plume and an increased value for the far-field plume potential. Thus, the overall magnitude of plasma potential profiles do not show a linear trend with the values of α_e in the plume. This non-monotonic trend may be due to the 2-D magnetic field effects in the plume. Unlike the inside of the discharge channel and near the channel exit—where the magnetic field is almost purely radial—the plume has a highly curved, two-dimensional magnetic field topology. The curvature and varying strengths of axial and radial magnetic fields in different regions of the plume may contribute to the non-monotonic trend between the mobility coefficient and the plasma potential.

Similar trends are shown along the cathode centerline (Fig. 4.32). As α_e decreases from 10.0 to 0.5, the far-field potential value monotonically decreases, and for smaller α_e, the far-field potential value increases. Because of the 2-D magnetic field effect, there may be one or more alternative α_e values that can produce similar profiles of the

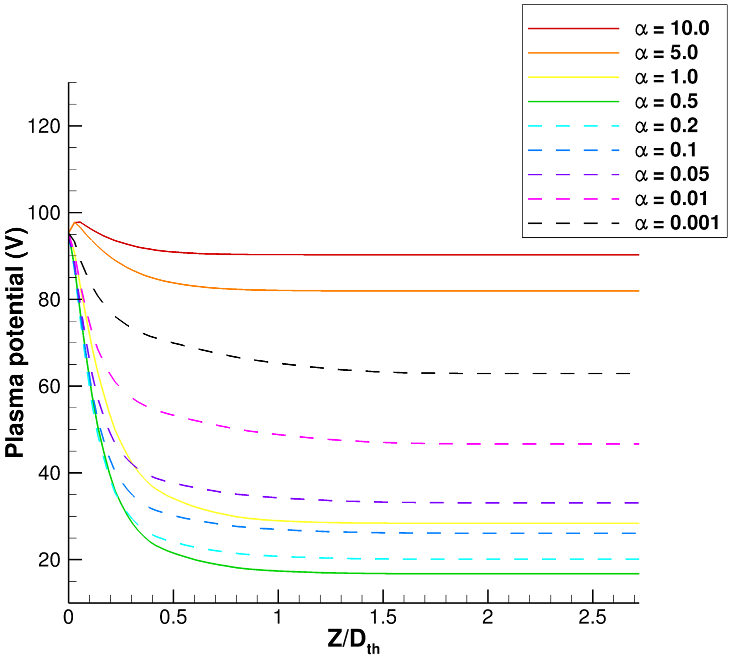

Figure 4.31: Axial profiles of plasma potential along the discharge channel centerline using various mobility coefficients.

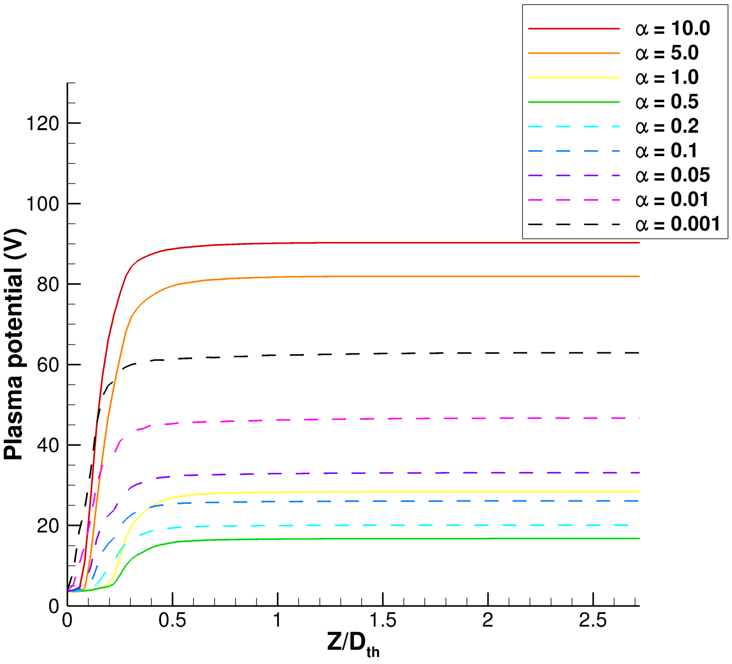

Figure 4.32: Axial profiles of plasma potential along the cathode centerline using various mobility coefficients.

plasma potential in the plume. For instance, the far-field plasma potential values are very similar for $\alpha_e = 1.0$ and 0.1. However, the profiles show slightly different behavior in the plasma potential in the very near-field plume for both the discharge channel and the cathode. Along the discharge channel centerline in Fig. 4.31, $\alpha_e = 0.1$ shows a steeper potential gradient than $\alpha_e = 1.0$. In Fig. 4.32, the plasma potential is more suppressed in the near-field cathode plume when using $\alpha_e = 1.0$ than $\alpha_e = 0.1$. To determine a value of α_e that results in a more accurate overall shape and magnitude, the simulation results need to be compared with experimental data.

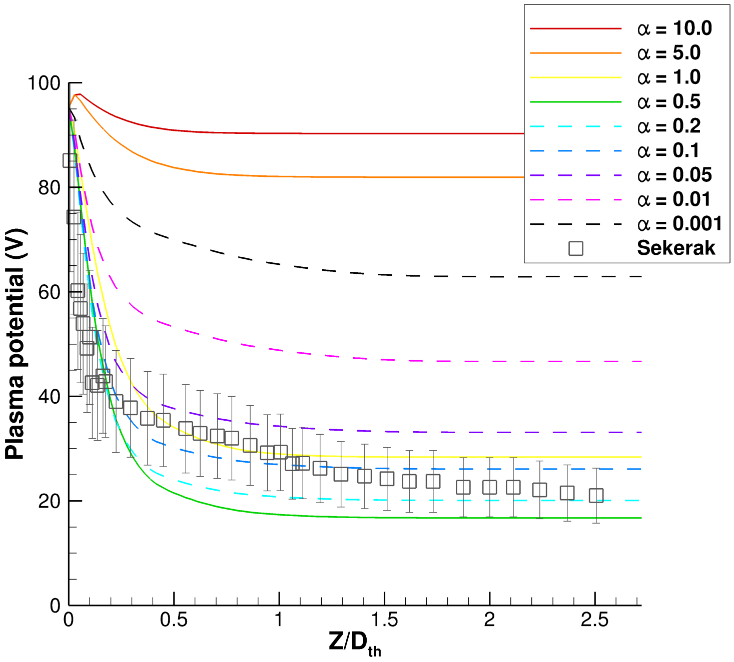

Figure 4.33: Axial profiles of plasma potential along the discharge channel centerline using various mobility coefficients, compared with experimental data [47].

In Fig. 4.33, axial profiles of the plasma potential along the discharge channel centerline are compared with experimental measurement by Sekerak [47]. When $\alpha_e = 5.0$ and 10.0, the plasma potential increases slightly in the very-near field plume of the discharge channel exit ($Z/D_{th} \approx 0$) before it drops slightly to the far-field plume potential downstream. These profiles are not similar to the experimental data, in which a steep negative gradient in the potential is observed in very near-field plume ($0 < Z/D_{th} < 0.2$). The potential gradient in this region is an extension of the potential gradient in the discharge channel produced by the localized transverse magnetic field. This steep potential drop causes an increased axial electric field that accelerates ions. In contrast to the high Bohm cases, the plasma potential drop in the very near-field plume is well captured by $\alpha_e = 0.1$ to 1. The far-field potential predicted using these values are about within the error bars of the measurement.

Figure 4.34 compares the axial profiles of plasma potential along the cathode centerline with experimental data. While the suppressed potential profile at the axial displacement of $Z/D_{th} < 0.5$ is well captured by using $\alpha_e = 0.5$, the far-field plume potential is slightly under-estimated. When using $\alpha_e = 0.1$ and 0.2, the plasma potential agrees well with the measured data, except in the very near-field plume of the cathode ($Z/D_{th} < 0.3$).

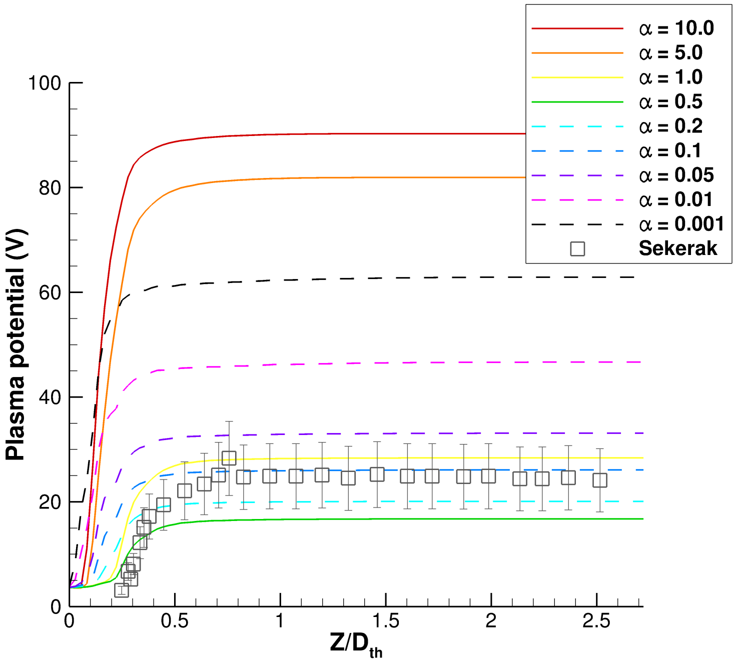

Figure 4.34: Axial profiles of plasma potential along the cathode centerline using various mobility coefficients, compared with experimental data [47].

While these trends do not offer an explanation of the underlying physics of the anomalous electron mobility, they show that the plasma potential profiles do not increase or decrease monotonically according to the anomalous Bohm coefficient in the plume due to the effects of 2-D magnetic field. Moreover, because of the completely different magnetic field topologies in the cathode plume and the near-field plume of the discharge channel, it is possible that different transport mechanisms may be dominant in different regions of the plume, which may indicate that multi-region mobility modeling is required. Since more than one α_e value can result in a similar value of the plasma potential, it is difficult to determine which value should be used. Therefore, other parameters should also be compared with experimental data in the future to determine the α_e value(s) that gives the best agreement with various experimental data. In this study, however, the mobility coefficients between 0.1 to 1 agree reasonably well with experimental data.

4.3.3 Multi-Region Mobility Modeling

Although the single-region mobility model gives an ability to better match experimentally-measured plasma properties, it is possible to further improve the agreement using a multiple-region mobility model. Multi-region models have been used by many studies [50, 51, 22], but they mainly focus on the plasma inside the discharge channel and the very near-field plume. This study does not attempt to solve the anomalous electron mobility problem. Rather, multi-region mobility modeling is performed to examine whether using spatially-varying mobility can further improve the agreement with experimental data. Typically, the mobility coefficient is varied only in the axial direction, which is a good assumption along the discharge channel centerline. This is the approach taken in the present work. However, capturing the electron transport in the cathode plume will require radially-varying mobility coefficients because the magnetic field is mainly axial.

Figure 4.31 from the previous section shows that the negative slope of the potential drop predicted by the current model is slightly lower than the experimental data just downstream of the discharge channel ($Z/D_{th} < 0.1$). This steep potential gradient is extended from the discharge channel potential gradient produced by the localized transverse magnetic field. Since this potential gradient causes an acceleration on ions, we want to obtain as accurate potential gradient profile as possible. In attempt to best match these features observed in the experimental data, the mobility calculation algorithm in the current model was slightly modified to use spatially-varying α_e values in three regions, as shown in Fig. 4.35. Each regions have a linear transition region that is determined by the following formula from Ref. [22]:

$$\alpha_e = \begin{cases} \alpha_1, & Z/D_{th} < Z_1 \\ \alpha_1 f_1 + \alpha_2 f_2, & Z_1 < Z/D_{th} < Z_2 \\ \alpha_2, & Z_2 < Z/D_{th} < Z_3 \\ \alpha_2 f_2 + \alpha_3 f_3, & Z_3 < Z/D_{th} < Z_p \\ \alpha_3, & Z/D_{th} > Z_p \end{cases} \tag{4.2}$$

where

$$f_1 = 1 - f_2$$

$$f_2 = \frac{Z/D_{th} - Z_1}{Z_2 - Z_1}$$

$$f_3 = 1 - f_4$$

$$f_4 = \frac{Z/D_{th} - Z_2}{Z_3 - Z_2}$$

Table 4.10: The Bohm coefficient (α_e) and the axial displacement (Z) used in the multi-region model. Z is normalized by thruster diameter D_{th}.

α_1	α_2	α_3	Z_1	Z_2	Z_3	Z_p
0.2	0.01	0.1	0.003	0.13	0.44	0.56

The axial profiles of the single-region and multi-region electron mobility for $\alpha_e =$ 0.01, 0,1, and 0.2 are shown in Fig. 4.36. Three distinct values of mobility is shown

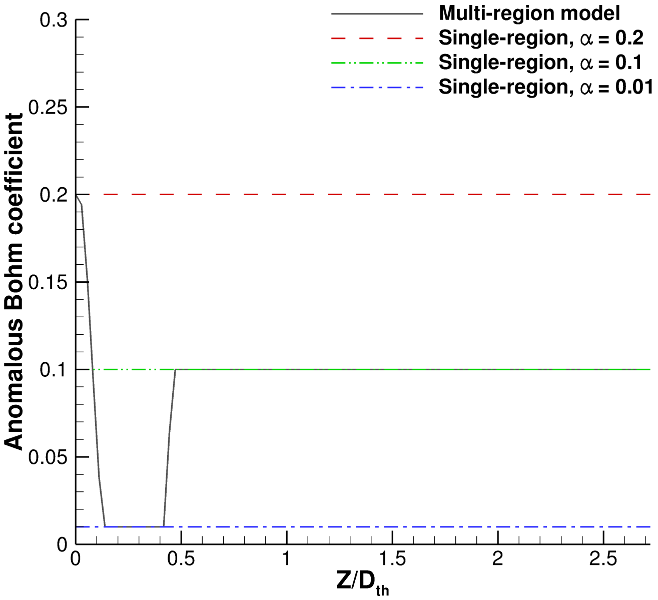

Figure 4.35: Axial profiles of single-region and multi-region mobility coefficients.

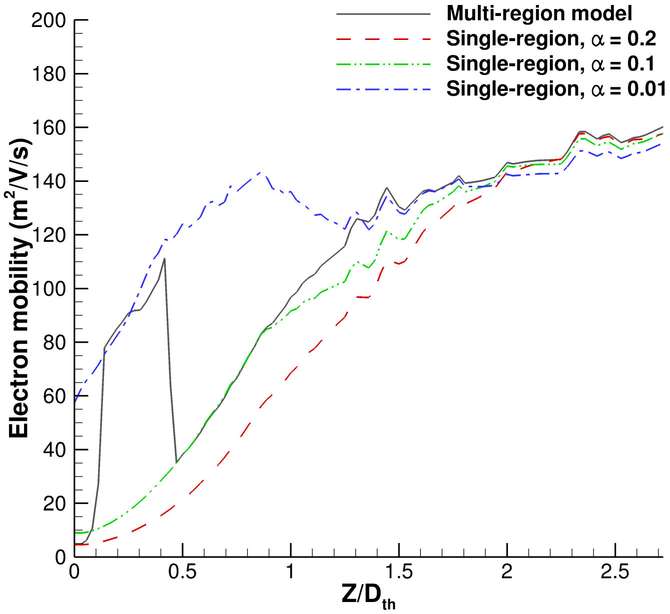

Figure 4.36: Axial profiles of single-region and multi-region electron mobility.

from the multi-region model. The electron mobility in the first region calculated using the multi-region model is identical to the mobility calculated using the single-region model with $\alpha_e = 0.2$. Similarly, the second and the third regions show the same profiles as the corresponding single mobility region.

The plasma potential profile calculated using the multi-region model is compared with the single-region model and experimental data in Fig. 4.37. The error-bars are removed to make the trends more clearly visible. While the single mobility coefficient cases show reasonably good agreement with experimental data, mixing the three mobility coefficients (i.e., $\alpha_e = 0.2$, 0.1, and 0.01) results in an excellent agreement with the experimental data. Especially, the multi-region mobility model successfully captures both the steep gradient in the very near-field plume of the discharge channel and the gradually-decreasing potential profile downstream.

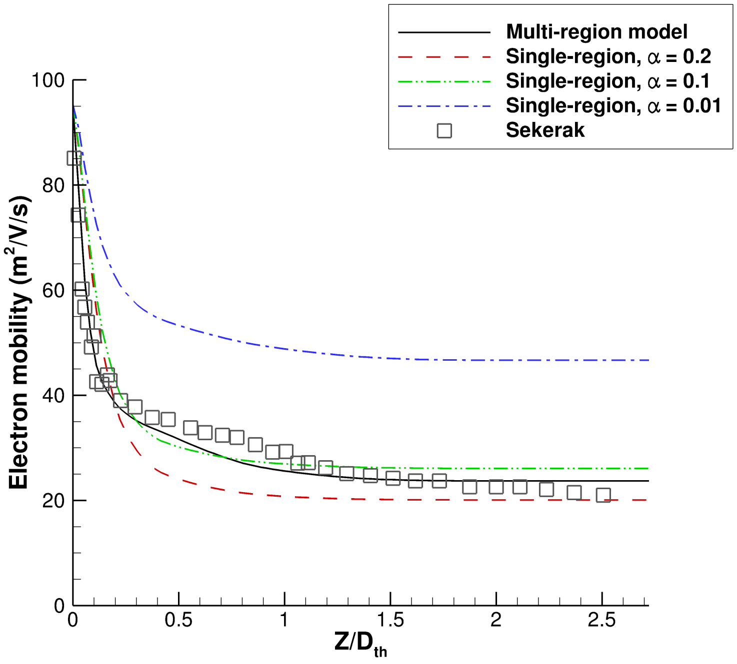

Figure 4.37: Axial profiles of plasma potential along the discharge channel centerline using a single-region and multi-region mobility model, compared with experimental data [47].

4.3.4 Discussion

The cross-field mobility of electrons is defined as:

$$\mu_\perp = \frac{e}{m_e \nu_e}\left(\frac{1}{1+\frac{\omega_g^2}{\nu_e^2}}\right) \tag{4.3}$$

In the limit of a large Hall parameter, the cross-field electron mobility is proportional to ν_e, which is true inside the discharge channel or near the channel exit of a Hall thruster, where the magnetic field is strong. Therefore, a large α_e would enhance the anomalous electron transport in this region, such as the very near-field plume of HPHall domain as shown in Ref. [22]. For small to intermediate values of the Hall parameter, the mobility is inversely proportional to α_e, which is true in the plume where the magnetic field strength decays quickly. In the plume, larger α_e reduces the mobility because having a large α_e coefficient would be equivalent to having a strong magnetic field that limits the transport of electrons. Therefore, there may be a turning point in the behavior of the mobility in the plume.

Although the multi-region model can successfully reproduce the potential profile along the discharge channel centerline, there could be more sets of α_e values that can produce a similar or better results. Moreover, the cross-field mobility modeling in the cathode plume may require radially-varying α_e coefficient. Therefore, more fundamental work on understanding the physics of anomalous electron transport is necessary for the future.

4.4 Comparison of the New Electron Model With and Without the Magnetic field

In this section, a series of simulation results using the new model with and without magnetic field effects is compared in order to study the effects of magnetic field on the plume properties. The following macroscopic plasma properties are examined: plasma potential, electron temperature, and ion current density. The standard discharge channel exit plane is used as the inflow boundary to couple the flow from the anode to the plume simulation. From the previous section, the constant mobility coefficient with $\alpha_e = 1$ and 0.01 and the multi-region coefficients ($\alpha_e = 0.2, 0.01$, and 0.1) showed the best results.

4.4.1 Plasma Potential

The contour plots of the plasma potential calculated without and with the magnetic field are compared in Fig. 4.38. Because the results using constant coefficients of $\alpha_e = 1$ and 0.01 and the multi-coefficients are similar, only $\alpha_e = 1$ is plotted to represent the model with the applied magnetic field. This figure shows very different overall shapes of the two models; while the model with the magnetic field has an equipotential shape that matches the magnetic field lines (Fig. 3.3), the model without the applied magnetic field does not. The far-field plasma potential is also different by about 70 V. At the near-field plume of the cathode, the plasma potential calculated by the model with the magnetic field is suppressed at lower potential. In comparison, the potential using the model without the applied magnetic field predicts a rapidly increasing plasma potential.

For a qualitative comparison, the axial profiles of the plasma potential along the centerlines of the discharge channel and the cathode are compared in Figs. 4.39 and 4.40. In the new model with the magnetic field, the plasma potential along the channel centerline is highest at the thruster exit plane ($Z/D_{th} = 0$) and decreases relatively quickly in the axial direction to the far-field plume potential of 24-28 V. In comparison, the plasma potential profile calculated by the model without the magnetic field increases slightly from $Z/D_{th} = 0$ to $Z/D_{th} = 0.1$ and then becomes almost constant to the far-field plume. The negative plasma potential gradient at the

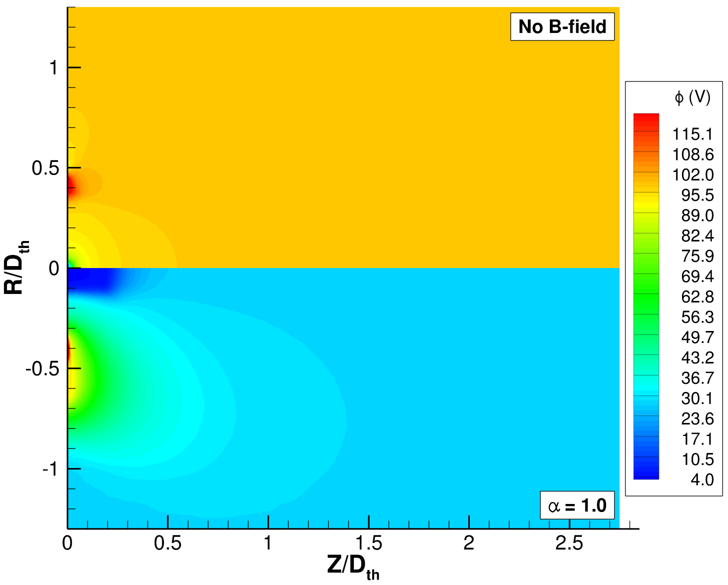

Figure 4.38: Contour plots of the plasma potential using the new electron model without the magnetic field (top) and with the magnetic field (bottom).

very near-field plume ($Z/D_{th} < 0.2$) is largest when multi-region model is used.

Figure 4.40 shows the axial profiles of the plasma potential along the cathode centerline. When the magnetic field is not included, the plasma potential increases very quickly in the axial direction to a large far-field plume potential (98 V). This potential profile reaches the far-field plume potential at about $Z/D_{th} = 0.2$ When the magnetic field is included, the profiles show similar far-field potential values ranging between 24-28 V. For $\alpha_e = 1$, the plasma potential is suppressed from the cathode exit ($Z/D_{th} = 0$) to $Z/D_{th} = 0.2$, and then gradually increases to the far-field plume potential. For $\alpha_e = 0.1$ and multi-region model, the "suppression" of the potential in the cathode plume becomes smaller.

4.4.2 Electron Temperature

For the same reason mentioned in Section 4.4.1, the model with the applied magnetic field with $\alpha_e = 1$ is compared to the model without the magnetic field in the contour plot shown in Fig 4.41. While the overall magnitudes are similar between the two cases, the shapes of the electron temperature profiles are different. The T_e predicted by the model without the magnetic field monotonically decreases from the near-field plume of the discharge channel exit to the far-field plume with an arc shape profile. In comparison, the model with the magnetic field does not predict a monotonically decreasing profile in the radial direction; the electron temperature is slightly elevated at approximately $R/D_{th} = 0.6$ and $R/D_{th} = 0.8$. The elevated temperature at these locations are likely caused by the large negative axial magnetic field occurring at theses locations. At the near-field plume of the cathode, the electron temperature calculated by the model with the magnetic field is lower than the model without the

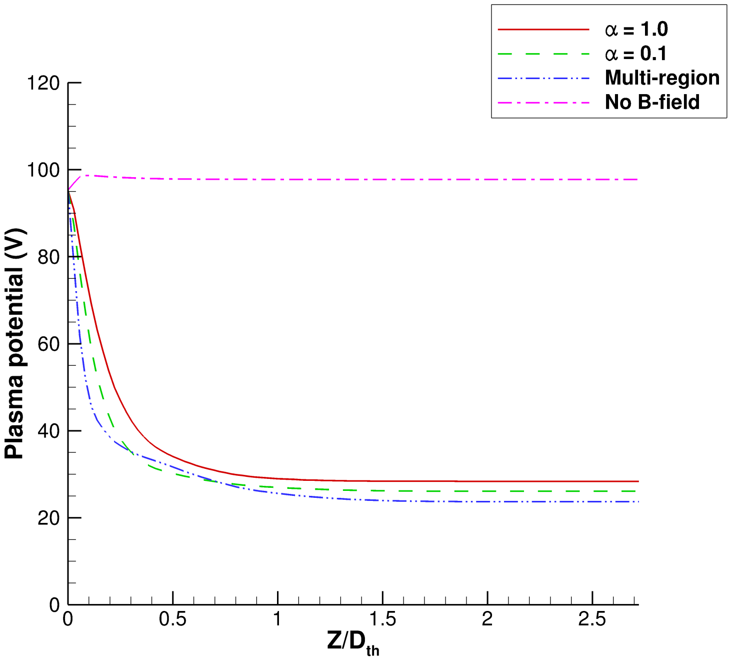

Figure 4.39: Axial plasma potential profiles along the discharge channel CL, comparing simulation results with and without magnetic field effects.

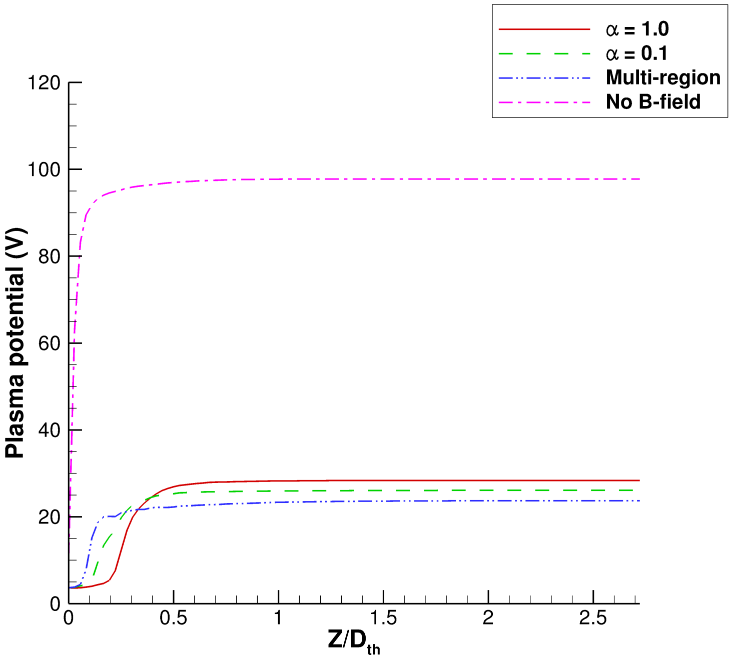

Figure 4.40: Axial plasma potential profiles along the cathode CL, comparing simulation results with and without magnetic field effects.

magnetic field.

The axial profiles of the electron temperature along the discharge channel centerline is shown in Fig. 4.42. The electron temperatures calculated without and with the magnetic field show similar profiles; the profiles monotonically decrease from the very near-field plume of the discharge channel exit (Z/D_{th}=0) to the far-field plume, which is also observed from the contour plot above.

Figure 4.43 shows the axial profiles of the electron temperature along the cathode centerline. The model without the magnetic field shows that the T$_e$ increases from the cathode exit ($Z/D_{th} = 0$) to its maximum value at about $Z/D_{th} = 0.15$, and then decreases monotonically downstream. Similar trend is predicted by the model with the magnetic field using multi-region mobility coefficients. The models with single-region mobility ($\alpha_e = 1.0$ and 0.1) predict that the T$_e$ increases rapidly from the cathode exit to $Z/D_{th} = 0.05$, reaches almost a constant value from $Z/D_{th} = 0.05$ to $Z/D_{th} = 0.5$, and decreases monotonically downstream.

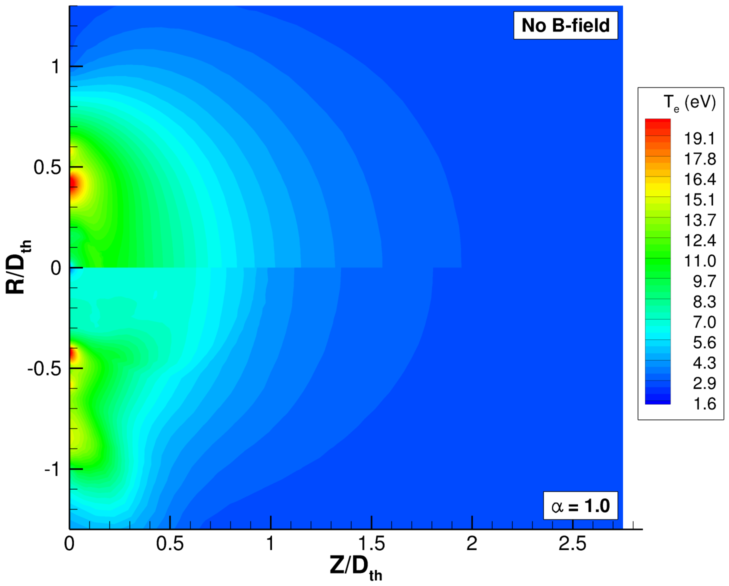

Figure 4.41: Contour plots of the electron temperature using the new electron model without the magnetic field (top) and with the magnetic field with $\alpha_e = 1.0$ (bottom).

4.4.3 Ion Current Density

The contour plots of the ion current density calculated without and with the magnetic field ($\alpha_e = 1.0$) are compared with the experimental measurement by Reid [48] in Fig. 4.44. They show similar contour profiles with slight differences in the cathode plume and the far-field plume. The ion current density in the cathode plume is higher when the magnetic field is neglected than included. Without the magnetic field, the ion current density shows a collimated beam structure across all axial displacements. With the magnetic field, the ion current density merges to the axis of symmetry at the far-field plume and is slightly higher in magnitudes than without the magnetic field.

Figure 4.45 shows the axial ion current density profiles along the discharge channel centerline. All models predict very similar ion current density profiles; the ion current density is the highest in the region just downstream of the discharge channel and

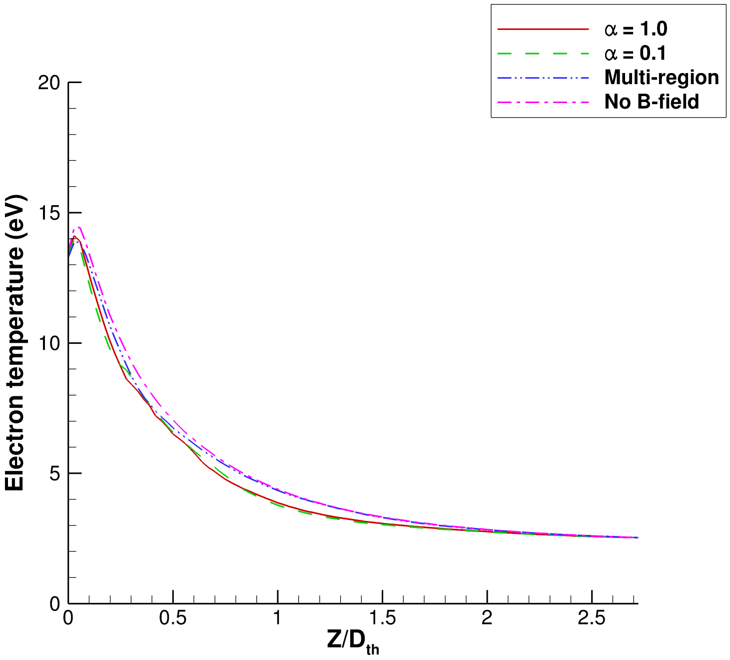

Figure 4.42: Axial electron temperature profiles along the discharge channel CL, comparing simulation results with and without magnetic field effects.

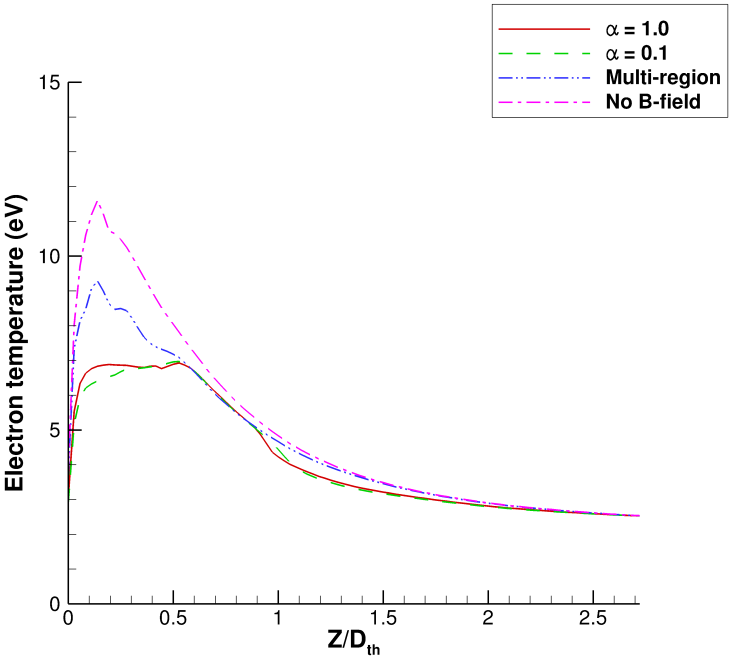

Figure 4.43: Axial electron temperature profiles along the cathode CL, comparing simulation results with and without magnetic field effects.

decreases gradually in the axial direction.

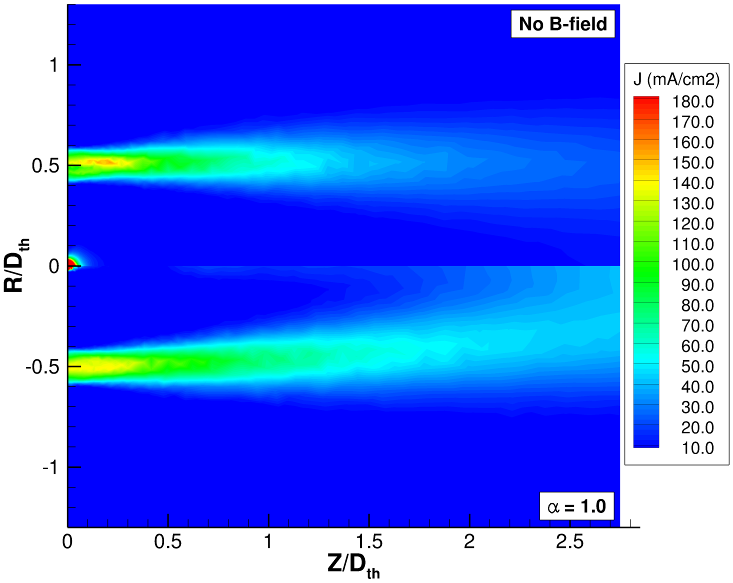

Figure 4.44: Contour plots of the ion current density using the new electron model without the magnetic field (top) and with the magnetic field with $\alpha_e = 1.0$ (bottom).

Figure 4.45 shows the ion current density profile along the cathode centerline. The magnitude of the ion current density is highest in the region just downstream of the cathode and decreases quickly in the axial direction to its lowest value between $Z/D_{th} = 0.3$ and $Z/D_{th} = 0.6$, and increases gradually downstream. The minimum ion current densities occurring in these regions are likely to be cause by the insufficient kinetic energy of ions to overcome the steep increase in the plasma potential, resulting in the negative axial velocity of ions at $Z/D_{th} < 0.3$. The model without the magnetic field effect shows lower magnitude of the overall ion current density profile along the cathode centerline.

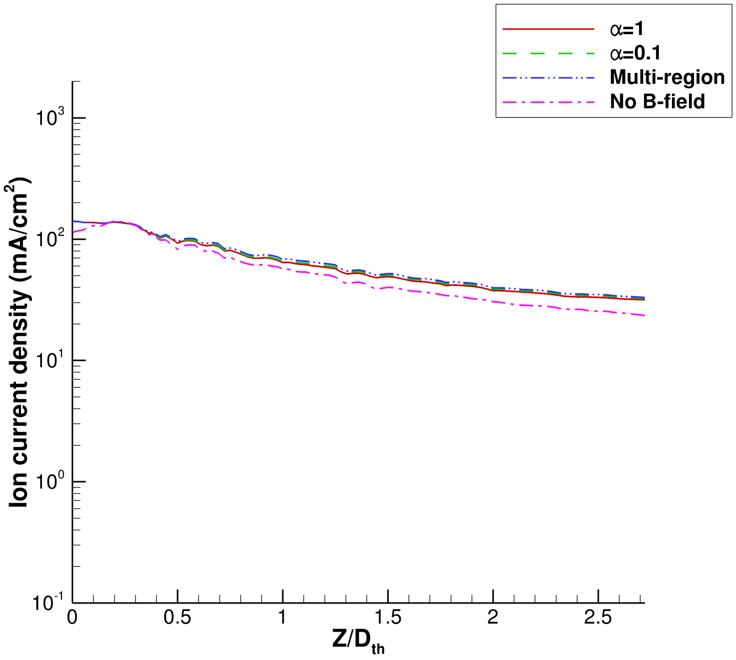

Figure 4.45: Axial ion current density profiles along the discharge channel CL, comparing simulation results with and without magnetic field effects.

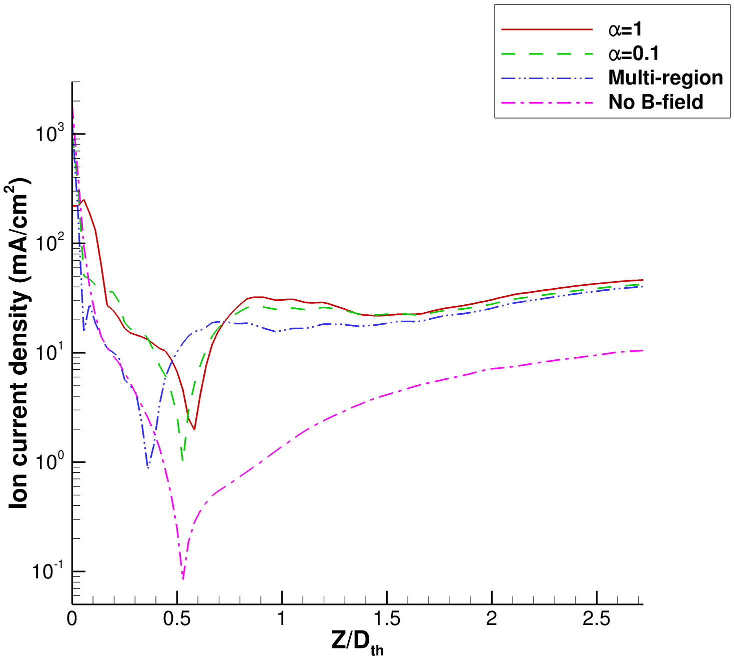

Figure 4.46: Axial ion current density profiles along the cathode CL, comparing simulation results with and without magnetic field effects.

4.5 Comparison of the New Electron Model and Experimental Data

In this section, a series of simulation results using the new model with and without the magnetic field effects is compared in order to validate the new model and study the effects of magnetic field on the plume properties. The following macroscopic plasma properties are examined: plasma potential, electron temperature, and ion current density. The standard discharge channel exit plane is used as the inflow boundary to couple the flow from the anode to the plume simulation. From the previous section, the constant mobility coefficient with $\alpha_e = 1$ and 0.01 and the multi-region coefficients ($\alpha_e = 0.2, 0.01$, and 0.1) showed the best results.

4.5.1 Plasma Potential

The axial profiles of the plasma potential calculated without and with the magnetic field are compared to experimental data [47] in Fig. 4.47. The experimental data shows a steep potential gradient in the very near-field plume ($0 < Z/D_{th} < 0.1$), which is an extension of the negative potential gradient from the acceleration channel. When the magnetic field is included, the new model predicts the steep potential gradient in the very near-field plume that is observed from the experimental data. The model with the multi-region electron mobility model shows excellent agreement with the experimental data. The model with the magnetic field using $\alpha_e = 1.0$ and 0.1 show reasonable agreement to the measurement by predicting a similar negative plasma potential gradient in the near-field plume and the far-field plume potential. In contrast, the model without the magnetic field does not predict the negative potential gradient in the near-field plume, and over-estimates the far-field plume potential by over 100 V.

Figure 4.48 shows the plasma potential profiles along the cathode centerline. The

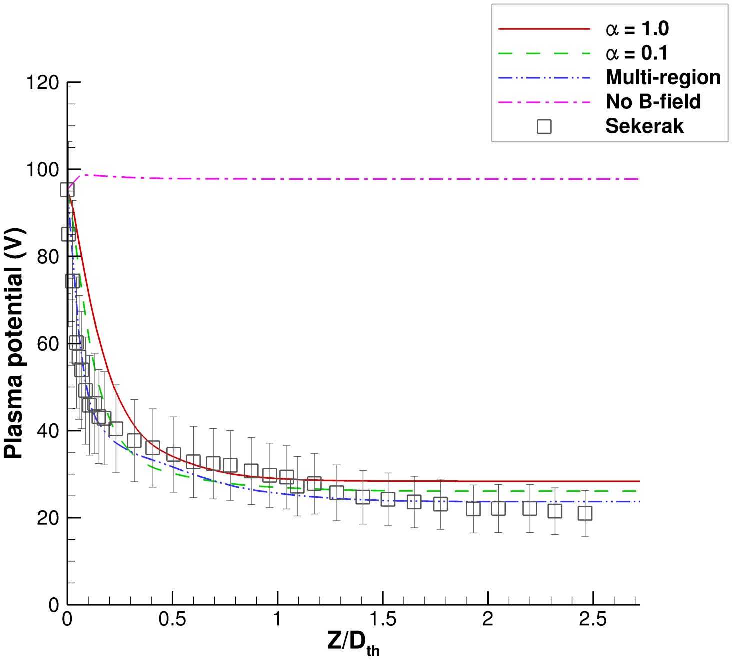

Figure 4.47: Axial plasma potential profiles along the discharge channel CL, comparing simulation results with and without magnetic field effects.

model without the magnetic field shows a steep increase in the potential, whereas the model with B-field shows a more gradually increasing potential. The model without the applied magnetic field over-predicts the entire plasma potential profile by about 70 V. When the magnetic field is applied, the overall magnitudes of plasma potential profiles agree with the experimental data. The near-field plume potential predicted using $\alpha_e = 1$ predicts the suppressed plasma potential that agrees well with the experimental data.

Figure 4.40 shows the axial profiles of the plasma potential along the cathode centerline. When the magnetic field is not included, the plasma potential increases very quickly in the axial direction to a large far-field plume potential (98 V). This potential profile reaches the far-field plume potential at about $Z/D_{th} = 0.2$ When the magnetic field is included, the profiles show similar far-field potential values ranging between 24-28 V. For $\alpha_e = 1$, the plasma potential is suppressed from the cathode

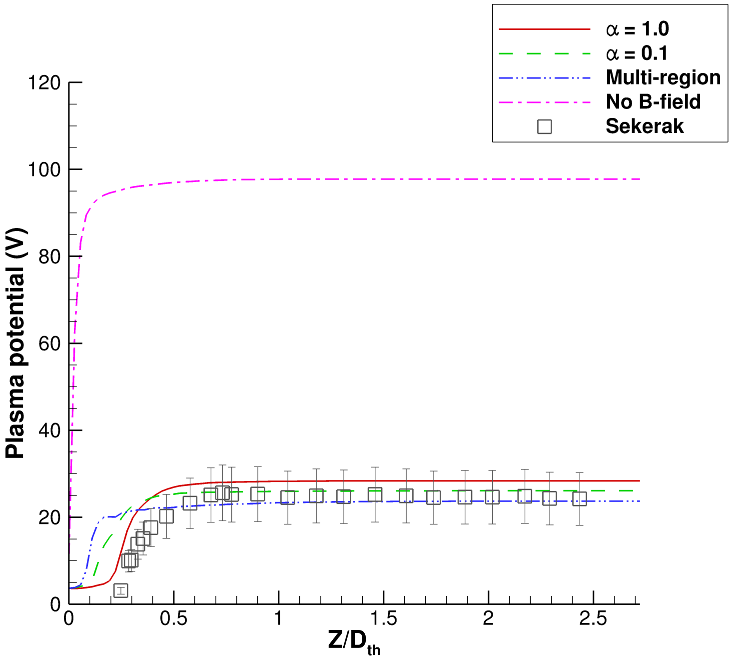

Figure 4.48: Axial plasma potential profiles along the cathode CL, comparing simulation results with and without magnetic field effects.

exit ($Z/D_{th} = 0$) to $Z/D_{th} = 0.2$, and then gradually increases to the far-field plume potential. For $\alpha_e = 0.1$ and multi-region model, the "suppression" of the potential in the cathode plume becomes smaller.

4.5.2 Electron Temperature

The electron temperatures calculated using the new model without and with the applied magnetic field are compared with the experimental data. Figure 4.49 shows the axial profiles of the electron temperature along the discharge channel centerline. Both the new models with and without the magnetic field effect show similar profiles; they reach their peaks at $Z/D_{th} = 0.05$ and monotonically decrease downstream. While the overall magnitudes of the profiles are similar to the experimental data, the data shows a steeper gradient of the electron temperature in the near-field plume than all the simulation results.

Figure 4.50 shows the axial profiles of the electron temperature along the cath-

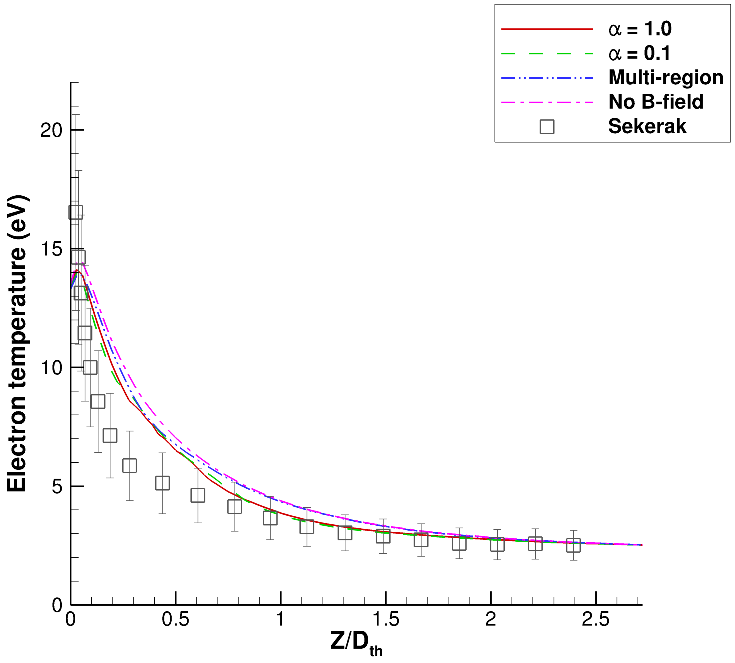

Figure 4.49: Axial electron temperature profiles along the discharge channel CL, comparing simulation results with and without magnetic field effects.

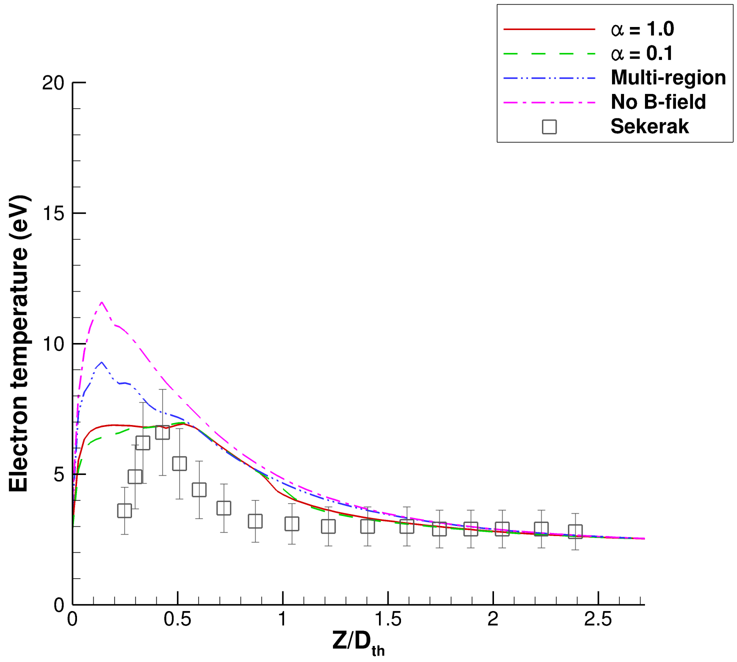

Figure 4.50: Axial electron temperature profiles along the cathode CL, comparing simulation results with and without magnetic field effects.

ode centerline. The experimental data shows a peak electron temperature at about $Z/D_{th} = 0.4$, which decreases monotonically downstream to a far-field plume temperature of about 3 eV. The model without the magnetic field and the model with multi-region mobility coefficients show similar trend, except that their peaks appear at the location of $Z/D_{th} = 0.15$. In comparison, the models with single-region mobility model ($\alpha_e = 1.0$ and 0.1) show almost constant values of electron temperature from $Z/D_{th} = 0.05$ to $Z/D_{th} = 0.5$, and decreases monotonically downstream.

4.5.3 Ion Current Density

Figure 4.51 shows the axial ion current density profiles along the discharge channel centerline. Both the models with and without the applied magnetic field show reasonably good agreement with experimental data. The model with the magnetic field slightly over-estimates the ion current density at the far-field plume. This is due

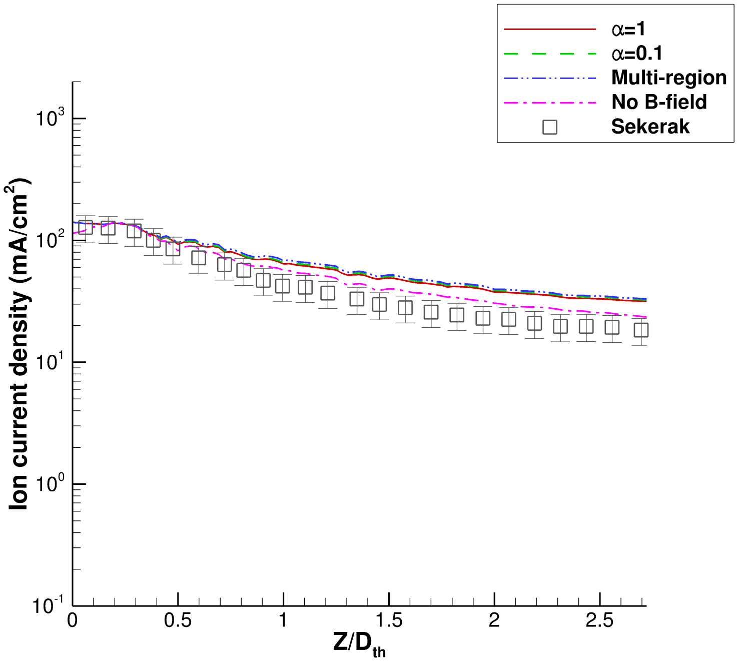

Figure 4.51: Axial ion current density profiles along the discharge channel CL, comparing simulation results with and without magnetic field effects.

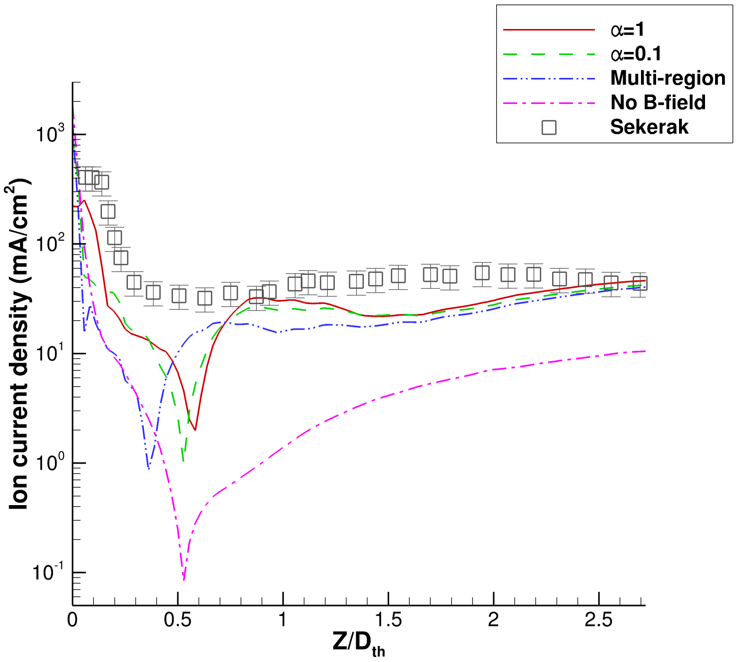

Figure 4.52: Axial ion current density profiles along the cathode CL, comparing simulation results with and without magnetic field effects.

to the magnetic field causing slightly more acceleration on the ions, through larger negative potential gradient along the channel centerline.

Along the cathode centerline in Fig. 4.51, the near-field profiles are not well captured by either simulations. While the experimental data shows almost a constant ion current density profile downstream of $Z/D_{th} = 0.3$, the calculated ion current densities are much lower. The decrease in the ion current density at $Z/D_{th} = 0.2$ to 0.4 is likely being insufficient to overcome the steep increase in the plasma potential that is previous observed in Fig. 4.51.

4.5.4 Discussion

Including the magnetic field effects results in much better agreement in the plasma potential with the experimental data. The model with the magnetic field effects successfully reproduces the large negative potential gradient in the near-field plume of the discharge channel. Especially, using the multi-region mobility model results in excellent agreement with the experimental data along the discharge channel centerline. In the cathode plume, the plasma potential profile along the cathode centerline is suppressed in the near-field plume and gradually increases to the far-field plume potential downstream. In order to further improve agreement in the plasma potential along the cathode centerline, the mobility model may need to be varied radially to capture the cross-field electron mobility in the radial direction since the magnetic field is mainly axial in the cathode plume.

The magnetic field also affects the electron temperature profiles. In the cathode plume, including the magnetic field effects lowers the magnitude of the electron temperature in the very near-field plume. However, both the models with and without the magnetic field do not capture the detailed profiles correctly. The rapid increase in the electron temperature in the near-field plume of the cathode may be improved by including more inelastic collisions, i.e., electron-impact excitation of neutrals and ions. Because the only inelastic collision implemented in the current model is the ionization of neutrals, there may not enough inelastic collisional losses for the electrons, which may cause the electron temperature to increase rapidly.

While good agreement is shown in the ion current density along the discharge channel centerline, large discrepancy is shown in the cathode plume. The steep increase in the plasma potential in the cathode plume pushes Xe^+ ions back towards the cathode, resulting in the negative velocity in the very near-field cathode plume. This results in the decreased ion current density in the cathode plume. This may be improved by applying more correct ion velocity conditions at the cathode boundary. The current cathode flow is slightly lower than the nominal H6 operating condition; the cathode flow rate used in OrCa2D simulation is 5% of the anode flow, whereas the nominal condition is 7% of the anode flow.

CHAPTER V

Modeling Erosion of the Cathode Keeper

A Hall thruster plume contains ions of various energies. Charge-exchanged ions and the energetic beam ions at large divergence angles from the thruster centerline can bombard surfaces of the thruster or components of the host spacecraft. If the bombarding ion has sufficient energy that is greater than the binding energy of the surface, one or more atoms can be ejected from the surface, which is a process known as sputtering. Sputtering on spacecraft components can reduce the life of the satellite or mission. Furthermore, sputtered materials can re-deposit onto other surfaces of the spacecraft (such as solar panel and optics) that can interfere with a mission. Modeling sputtering phenomena is, therefore, an essential capability in Hall thruster plume simulations from the perspective of spacecraft integration. A sputter model can be used to predict the sputter or erosion rates, and even the lifetime of the thruster or any other components. Furthermore, the simulation can be used to determine the positions of different components of the satellite and the design of the solar arrays.

In this chapter, a sputter model that is implemented into MPIC is described. The sputtering model is used to simulate the steady-state erosion behavior of the cathode keeper in the H6 Hall thruster. Then, the simulation results from the sputtering model are reported.

5.1 Sputter Model

A sputtering model is implemented in MPIC to calculate erosion rates of solid surfaces due to ion bombardment. Sputter yield is primarily a function of target material, incident species, incident energy, and incident angle. The total sputter yield is the product of the energy-dependent yield at normal incidence angle, $Y(E)$, and the angle-dependent yield, $Y(\theta)$:

$$Y = Y(E)Y(\theta) \tag{5.1}$$

In the current sputter model, the sputter yield, Y, is determined by using fitting functions for $Y(E)$ and $Y(\theta)$.

The energy-dependent yield for the ions impacting a wall at normal incidence can be calculated using the following formula [54, 55]:

$$Y(E) = A\sqrt{E}\left(1 - \sqrt{\frac{E_{th}}{E}}\right)^{B} \tag{5.2}$$

where E is the total energy of the projectile atom impacting the wall, E_{th} is the threshold energy below which sputtering does not occur, and A and B are fitting coefficients for experimental data. Traditionally, $B = 2.5$ for a carbon target, but here we are using it as a free parameter to best fit the experimental data.

Before striking the surface, ions must transverse a sheath. Although the plasma sheath at surfaces is not resolved in the current plume model, the total energy of an ion is calculated as the sum of its direct kinetic energy and the sheath potential energy—the drop in potential across the sheath. Assuming there is no secondary electron emission, the sheath potential is:

$$\phi_s = \frac{k_B T_e}{e} \ln\left(\frac{M}{2\pi m_e}\right)^{1/2} \tag{5.3}$$

where M is the mass of the ion and m_e is the electron mass.

The keeper of the $\mathrm{LaB_6}$ cathode in the H6 thruster is made of graphite [56]. Most published theoretical works [54, 57] predict a threshold energy higher than 130 eV for xenon ions bombarding a carbon target, but more recent experiments [58, 59] show that sputtering does occur at or below 50 eV. Although there is no exact threshold energy data for graphite, Ref. [60] reports that modeling results are in better agreement with experimental data if the accumulation of xenon in graphite is accounted for. This means that some fraction of the projectiles are carbon and some fraction of the target atoms are xenon. Including this effect, the threshold energy for sputtering on graphite surface can be calculated as 36.5 eV using the equation below [60]:

$$\frac{E_{th}}{U_s} = \frac{1 + 5.7\left(\frac{M_1}{M_2}\right)}{\gamma} M_1 M_2 \tag{5.4}$$

where U_s is the surface binding energy of the target solid in eV, γ is an energy transfer factor in the elastic collision, and M_1 and M_2 are the masses of the projectile and target atom, respectively. The threshold energy of 36.5 eV is used in the current sputtering model in MPIC, since it is in good agreement with the experimental results [58, 59].

Experimental measurements of the sputter yields of various forms of carbon and graphite from xenon ion bombardment at normal incidence [58, 59, 61, 62, 63] are plotted in Fig. 5.1. Based on these data, coefficients to the fitting function in Eq. 5.2 are determined as $A = 0.013$ and $B = 3$.

The angle-dependent yield is defined as [55]:

$$Y(\theta) = 1 + c_0[1 - \cos(c_1\theta)]^{c_2} \tag{5.5}$$

where θ is the angle relative to the wall normal and c_0, c_1, and c_2 are the fitting coefficients for experimental data. Experimental measurement of sputter yields at

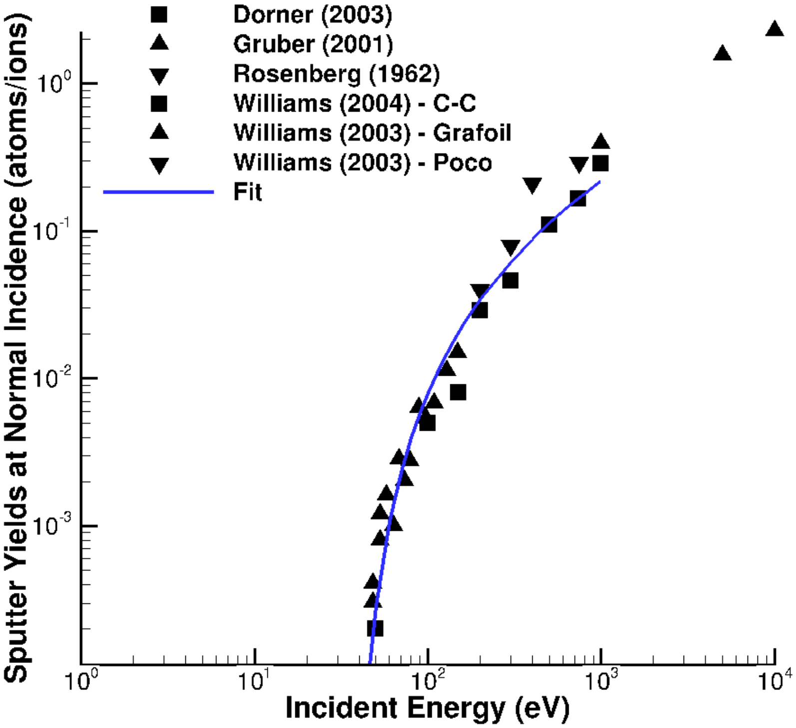

Figure 5.1: Experimental data and fitting functions of the sputter yield at normal angle incidence [58, 59, 61, 62, 63] using fitting coefficients of $A = 0.013$ and $B = 3$, and the threshold energy of $E_{th} = 36.5$ eV for Eq.5.2.

various incidence angles [64] are normalized and shown in Fig. 5.2 with the fitting function. The coefficients for Eq. 5.5 are determined as $c_0 = 0.91$, $c_1 = 2.5614$, and $c_2 = 1.91$.

The sputtering model is activated when the simulation starts sampling for macroscopic parameters after steady state has been reached, given that the incident energy of the particle is greater than the threshold energy of the surface. During the sampling period, the energies and fluxes of incident particles onto the wall surfaces are recorded whenever particles cross the wall boundary, using the particle-in-cell algorithm described in Section 2.1.2. At each timestep, the erosion rate is calculated as the product of incident flux on a target surface and the sputter yield calculated using Eq. 5.1. The erosion rate at each timestep is totaled during the entire sampling pe-

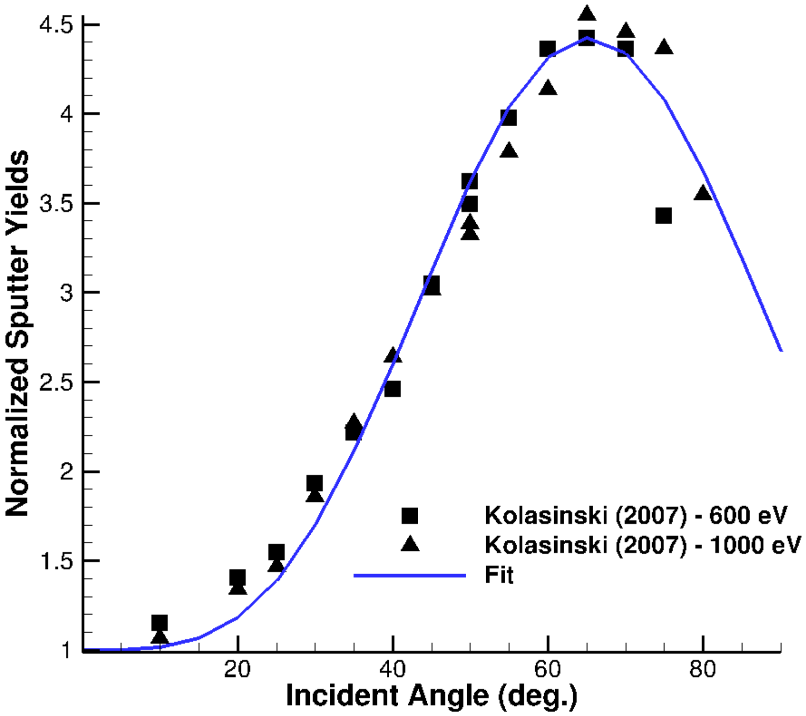

Figure 5.2: Experimental data and fitting functions of normalized sputter yield at various incident angles with incident ion energy of 600 eV and 1000 eV [64] using coefficients $c_0 = 0.91, c_1 = 2.5614$, and $c_2 = 1.91$ to Eq. 5.5.

riod, and is divided by the number of sampling timesteps at the end of the simulation to determine the mean erosion rate. The resulting mean erosion rate is reported as a function of position along the surface.

5.2 Modeling Erosion of the Keeper Surface

For long-duration missions using Hall-effect thrusters, the thrusters need to operate at high efficiency and for a long lifetime. The lifetime currently required by NASA may exceed 80,000 hours for long-duration missions [35]. One of the main life-limiting factor in conventional Hall thrusters has been the erosion process of the discharge channel walls due to ion bombardment. However, the erosion of the discharge channel walls in the state-of-the art magnetically shielded thrusters has effectively been eliminated as a failure mechanism. Magnetic-shielding is associated with shaping magnetic field lines such that the discharge channel walls are shielded from ion bombardment by achieving ideal equipotentialization of the lines of force near the walls [65][66]. The next potential failure mode in a magnetically shielded Hall thruster is now the erosions of the cathode and surface of the magnetic-field pole-pieces [56][67]. Modeling the sputtering of these surfaces is necessary to predict the erosion mechanism and rates, and eventually improve the limited lifetime of these components in a Hall thruster.

In the present study, the sputter model described above is applied to simulate the sputtering process of the LaB_6 cathode keeper in the H6 Hall thruster. The mean erosion rate is calculated and presented below that can be used to determine cathode erosion as a potential life-limiting factors of the thruster. The sputtering model can also be used to simulate the erosion profile on any surfaces, such as the thruster pole-pieces in magnetically shielded thrusters or any components of host spacecraft in the future.

5.3 Results for Estimating Keeper Erosion Rate

The sputter model described in this chapter is used to simulate the erosion behavior on the exit plane of the keeper wall as shown in Fig. 5.3. The keeper wall consists of four computational cells, and the results are shown with normalized radial displacements from 0 to 1. When a particle hits the keeper surface, its energy and incident flux are recorded on each surface element to calculate the sputter yield and erosion rate as a function of position. In this section, the energy distributions and fluxes of incident particles, and the erosion rate due to these particles are discussed. The simulation is performed using the new model described in Chapter III without applied magnetic field in the effective inlet domain, because this model showed very good agreement with experimental data for the H6 thruster plume (Chapter IV).

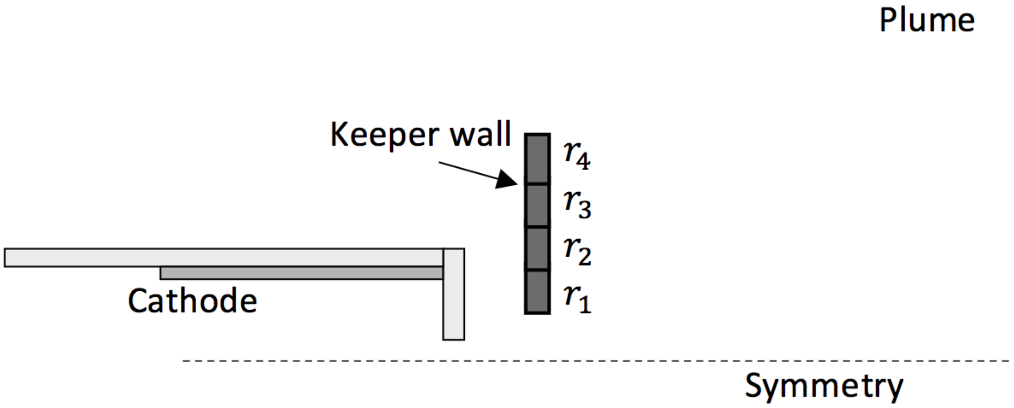

Figure 5.3: A schematic of cathode keeper wall for calculating sputter yields and erosion rates.

5.3.1 Incident Energy Distributions of Heavy Species

In Figs. 5.4 to 5.7, the incident energy distributions of xenon neutrals and ions are plotted. Cell 1 corresponds to the radially inner-most cell and cell 4 corresponds to the cell located farthest away from the cathode centerline. The vertical axes have arbitrary units. Figure 5.4 shows the Xe neutral energy distributions. The majority of the neutrals have very low energy (<5 eV), and only very few of them have high-enough energy (>36.5 eV) to contribute to the sputtering of the wall. The neutrals hit the keeper uniformly on each cell.

The energy distributions of Xe^+ ions on the keeper walls are shown in Fig. 5.5, where two distinct peaks are observed. Not all Xe^+ ions have energy greater than the threshold energy of 36.5 eV. According to the small shifts observed in the peaks in the lower energy range (<30 eV), the ions hitting the cells located at smaller radii have lower energies than the ions hitting the cells at larger radii. The second peaks in the slightly greater energy-range (>30 eV) show that the number of ions hitting the surface with this energy range increases as the radial displacement increases.

A similar trend is observed for double-charged ions in Fig. 5.6. The energy peak for the lower energy range is shifted slightly to the right for cells at larger radii, and

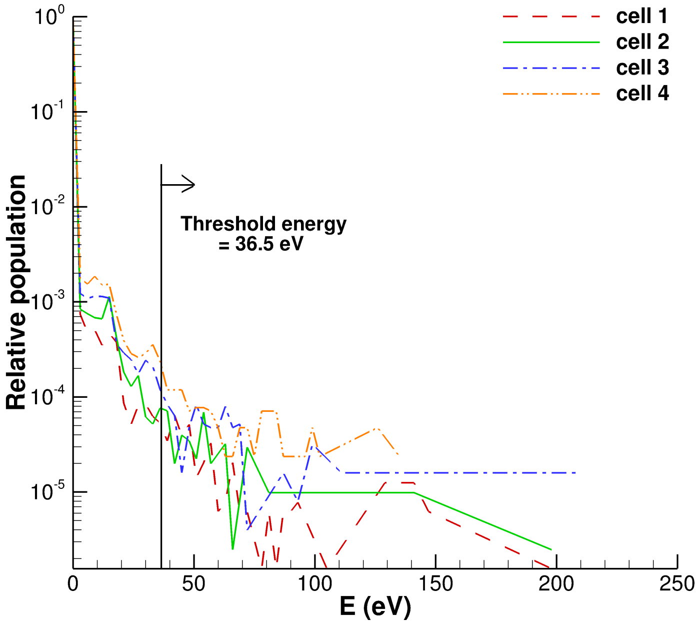

Figure 5.4: Incident Xe species energy distributions on the keeper wall.

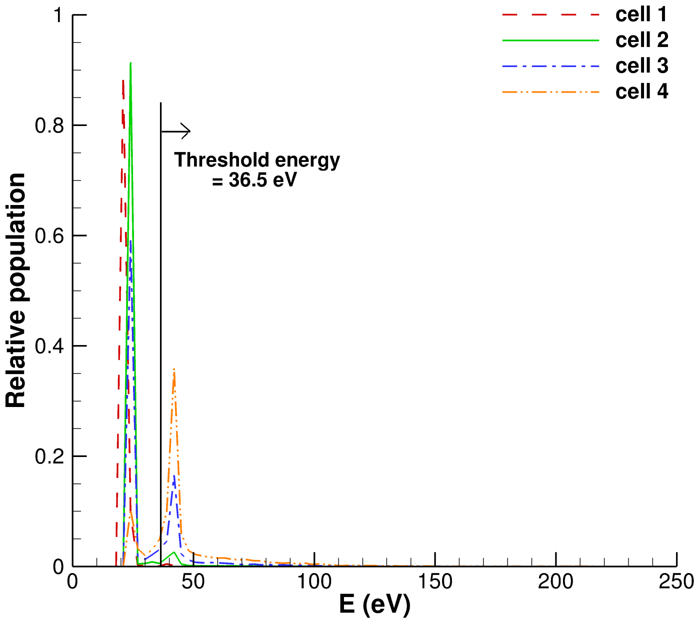

Figure 5.5: Incident Xe^+ species energy distributions on the keeper wall.

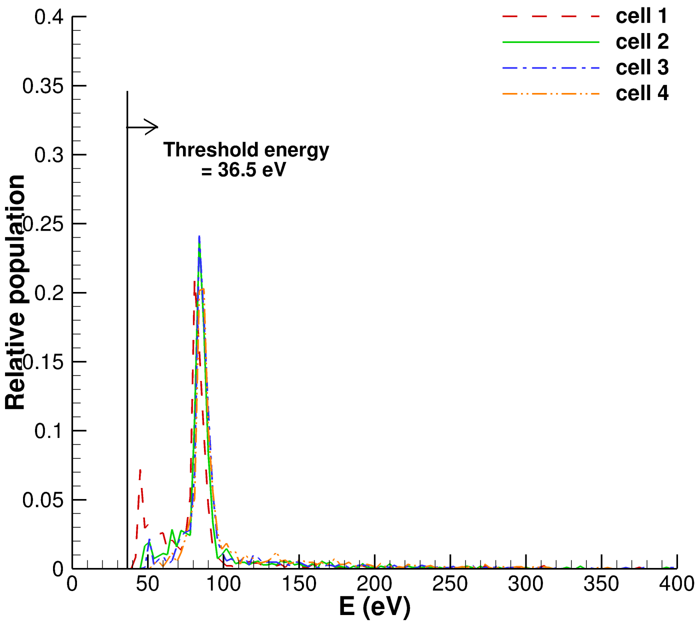

Figure 5.6: Incident Xe^{2+} species energy distributions on the keeper wall.

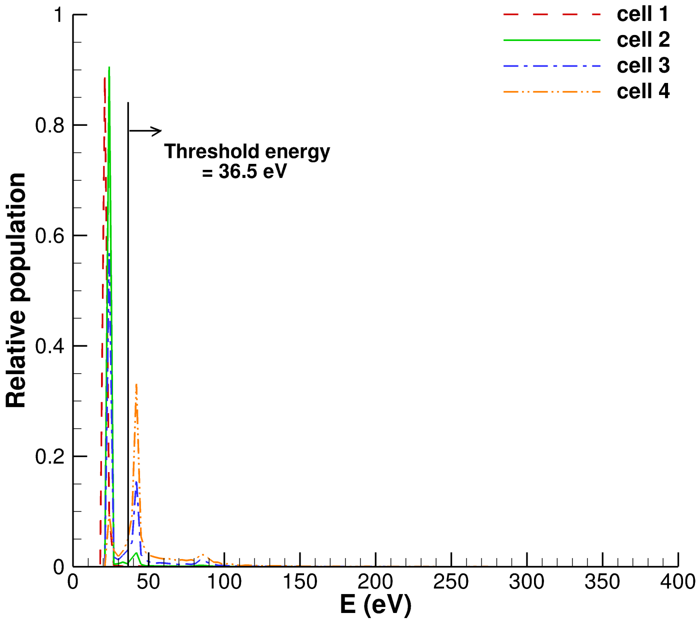

Figure 5.7: Incident total ion energy distributions on the keeper wall.

cell 4 experiences more ions with higher energy than cell 1 does. Almost all of the Xe^{2+} ions hitting the keeper can contribute to sputtering of the surface since their energy is greater than 36.5 eV.

The total ion energy distributions (i.e., Xe^+ and Xe^{2+}) are shown in Fig. 5.7, where two distinct peaks below 50 eV and one very small peak around 90 eV are observed. While almost all Xe^{2+} have sufficient energy to sputter the keeper, only a fraction of Xe^+ have enough energy to sputter.

Ions are accelerated through the decrease in the plasma potential, and gain energy through the sheath potential that is proportional to electron temperature, as in Eq. 5.3. According to the electron temperature profile on the wall shown in Fig. 5.8, ions accelerate through a slightly greater sheath potential for cells at larger radii (i.e., cell4) than the cells at smaller radii because T_e is slightly greater at larger radii (i.e., cell 1).

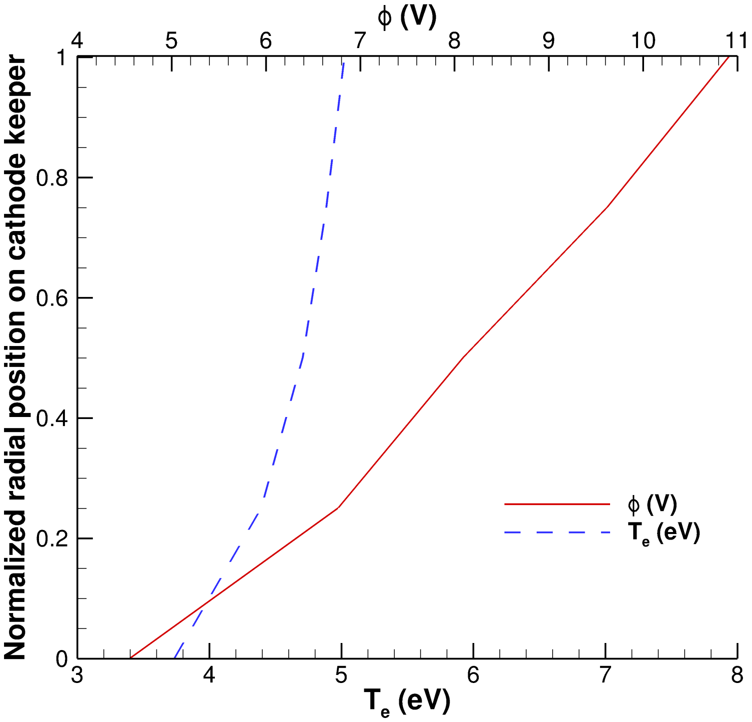

Figure 5.8: The plasma potential ($\phi(V)$) and electron temperature ($T_e(V)$) profiles along the keeper wall boundary. Sheath potential is not shown.

5.3.2 Incident Fluxes of Heavy Species

Figure 5.9 shows the fluxes of each species on the keeper surface as a function of normalized radial displacement. The neutral flux on the keeper is up to about one order of magnitude higher than Xe^+ and two orders of magnitude higher than Xe^{2+}. While flux of Xe is almost constant along the keeper, the fluxes of ions are the highest on cell 1 which is the lowest radial displacement on this plot. The fluxes of ions hitting cell 1 are the highest because the number density is the highest and the plasma potential is the lowest at this location than other cells (Fig. 5.8). As a result, the total flux of all heavy species is as shown in Fig. 5.9.

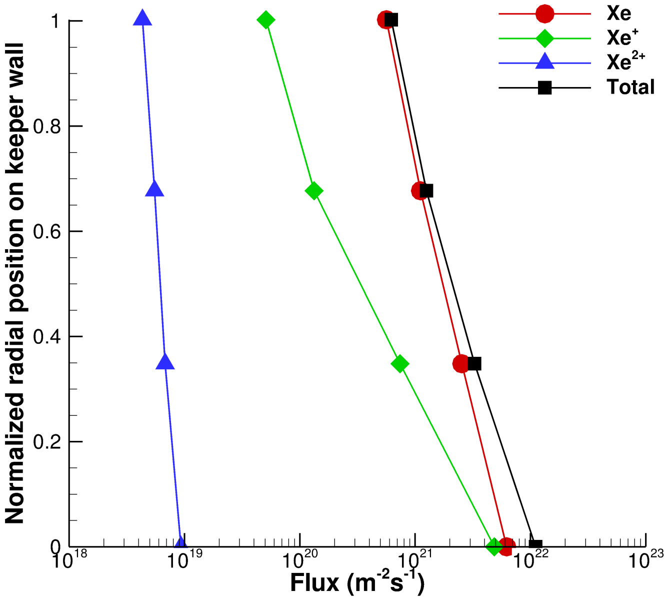

Figure 5.9: Incident fluxes of Xe, Xe^+, Xe^{2+}, and total species on the keeper wall.

5.3.3 Prediction of Mean Erosion Rate

Figure 5.10 shows the mean erosion rates as a function of normalized radial displacement of the keeper for all species. The erosion of the keeper is mainly caused by Xe^{2+} ions and partially by Xe^+ ions. Although the flux of Xe^{2+} is much lower than Xe neutrals and Xe^+ (Fig. 5.9), their incident energies are much greater than the threshold energy (Fig. 5.6), unlike most of the neutrals and single-charged ions. The mean erosion rate calculated by all heavy species is approximately 0.014 μm/h.

Although no keeper erosion measurements for the H6 thruster are available, the calculated mean erosion rate is compared with the published erosion rate of the discharge channel wall, also known as the insulator ring, from Ref. [66], in Table 5.1. The estimated mean erosion rate of the keeper wall is approximately 0.014 $\mu m/h$, which is of the same order of the measured erosion rate of the inner channel wall of the magnetically shielded (H6MS) thruster, and more than three orders of magnitude lower than the erosion rates of both the inner and outer rings of the unshielded (H6US) thruster.

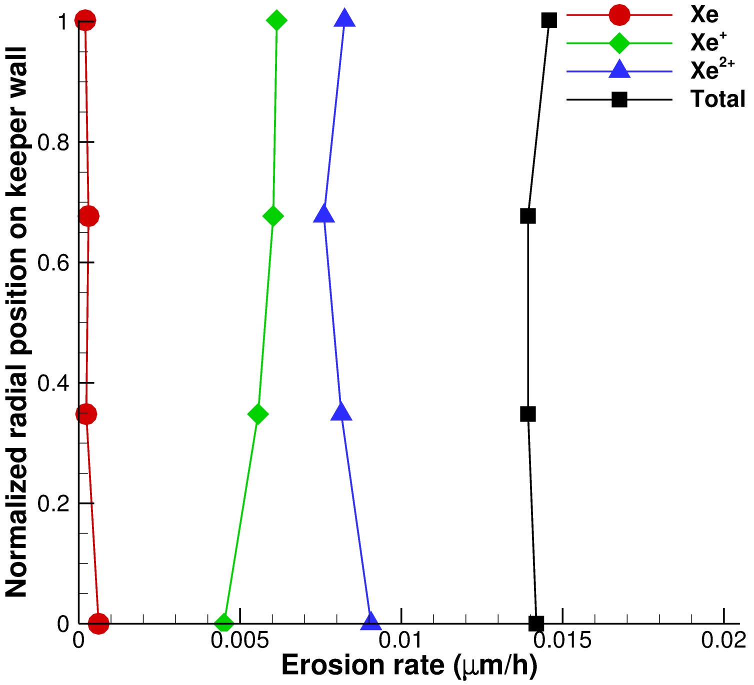

Figure 5.10: Steady-state mean erosion rate as a function of radial displacement on the keeper by all heavy species.

Table 5.1: Summary of measured erosion rates of the discharge channel walls of the H6US and H6MS thrusters [66].

	Axial Position ($Z/L_{channel}$)	Erosion Rate (μm/h)
Unshielded - outer ring	0.973	15.0
Unshielded - inner ring	0.973	19.7
Magnetically shielded - outer ring	0.947	0.00
Magnetically shielded - inner ring	0.947	0.02

5.4 Summary

A sputter model is implemented in MPIC to extend the capability of the plume model. Semi-empirical fits for the energy- and angle-dependent sputter yields are found using available data for Xe bombarding graphite surface. The H6 thruster plume with the effective inflow domain is simulated using the new model without magnetic field. The sputter model is applied to estimate the erosion rates along the cathode keeper wall.

The energy distributions and fluxes of all heavy species are calculated. While the flux of Xe neutrals is the highest, their energy is not sufficiently high enough to cause much sputtering. The keeper erosion is mainly contributed by Xe^{2+} ions and partially by Xe^{+}. Since double ionization is not allowed in the current model and no Xe^{2+} ions are injected from the cathode inlet, these ions are migrated from the discharge channel. The resulting erosion rate of the graphite keeper wall is 0.014 μm/h which is comparable with the erosion rate of the inner ring in the H6MS thruster.

CHAPTER VI

Conclusions

In this chapter, the major conclusions from and contributions of this dissertation are summarized, and suggested approaches to further improving Hall thruster plume simulations are discussed.

6.1 Summary

There were four main objectives of this dissertation: 1) to develop an accurate physics-based model to simulate a Hall thruster plume by including magnetic field effects; 2) to improve the accuracy of the plume simulation by refining the cathode boundary condition; 3) to assess the accuracy of the new model through comparisons with available experimental data; and 4) to extend the capability of the plume model by implementing a sputter model.

To simulate the plasma plume generated by the H6 Hall thruster, the 2-D axisymmetric hybrid particle-fluid model (MPIC) was used. This model uses the particle-based kinetic approach, known as the DSMC-PIC method, to describe the heavy species (i.e., neutral and ion), while an electron fluid model solves the continuity, momentum, and energy conservation equations of the electrons at steady state. In order to achieve the first objective of the dissertation, a new electron fluid model that includes magnetic field effects was developed, tested, and incorporated into MPIC.

The new governing equation for this model was derived in a 3-D cylindrical coordinate system without loss of generality (Chapter III). The new electron model is capable of simulating 2-D axisymmetric magnetic field effects, which enables the simulation of any shape of magnetic field topology. By including the magnetic field, the new governing equation now consists of a tensor form of electron mobility coefficient.

In order to solve the new governing equation with a tensor coefficient, the continuous Galerkin finite element model was developed. The prior model had a single general Poisson equation solver that uses the least-squares method to estimate derivative terms in order to calculate a linear forcing term. In contrast, the new continuous Galerkin finite element model solves the governing equation directly. Moreover, a quadrature rule was used to integrate the weak form, and the biconjugate gradient method was used to efficiently solve the linear system. Including the magnetic field does not require additional computational time, because the least-squares method is not used.

To confirm the order of accuracy of the new continuous Galerkin finite element method, a grid-convergence study with the method of manufactured solutions has been performed using various analytic solutions, including polynomial, sinusoidal, and exponential solutions. As a result, 2^{nd} order accuracy was confirmed. Another verification of the new electron model was performed by simulating a Hall-thruster-like test case. The simulation results of the model was compared with a new 2-D axisymmetric finite difference model developed by Dragnea [46]. The 2^{nd} order accuracy was confirmed again through a grid convergence study.

The second objective of improving the accuracy of the plume simulation was achieved by coupling internal plasma simulations to the current model to provide physically accurate boundary conditions at the discharge channel and cathode inflows. The prior work by Huismann [7] coupled the discharge channel exit as an inflow in order to use the plasma conditions simulated by HPHall as inflow conditions for the plume model. The present study used the same conditions as this prior work at the discharge channel exit. Since the prior work made a strong assumption about the composition of the cathode mass flow. The refinement of the boundary condition at the cathode inflow was achieved by using plasma conditions simulated by OrCa2D [23]. These conditions were coupled with the plume simulation at the exit plane of the cathode keeper. All simulations in this dissertation were performed with the improved cathode inflow conditions.

First, the effect of electron models is studied by comparing the new model without the magnetic field and the prior model. Simulations were performed using the "effective" inlet proposed by the prior work [7]. Although the left hand side of the governing equation of the new model reduces to the prior model when applied magnetic field is zero, the plasma potential structure were slightly different because different numerical schemes are used with different assumptions in the two models. The new model puts the governing equation directly into a weak form and discretize using the continuous Galerkin method. In comparison, the prior model estimates derivatives of the source terms and add them to form a linear forcing function, which is then discretized by using the continuous Galerkin method. A number of assumption (e.g., using the least squares method and assuming $\nabla(1/n_e)$ is negligible) that goes into the formulation of the prior model results in a slightly different plasma potential profile in the plume. The order of accuracy of the prior model can be calculated using the method of manufactured solution.

Next, in order to study the effect of the magnetic field, the new model with the magnetic field effect was compared with the new model without the magnetic field effect using the standard discharge channel inflow domain. A single-region and multi-region mobility models were used to simulate the cross-field electron transport. A parametric study was performed to examine the effect of anomalous mobility coefficient (α_e) in plume properties. The effect of the anomalous Bohm coefficient was found to follow a non-monotonic relationship with the plasma potential because of the 2-D magnetic field effect; there was a turning point in the behavior of the mobility. In the plume, larger α_e reduces the mobility because having a large α_e coefficient would be equivalent to having a strong magnetic field that limits the transport of electrons. Although the multi-region model can successfully reproduce the potential profile along the discharge channel centerline, there could be one or more sets of α_e values that can produce a similar potential profile. Moreover, the cross-field mobility modeling in the cathode plume may require radially-varying α_e coefficient. Therefore, more fundamental work on understanding the physics of anomalous electron transport is necessary for the future.

In the presence of the magnetic field, the plasma potential gradient in the near-field plume of the discharge channel is captured by the model. In the cathode plume, where the axial magnetic field is relatively strong, the model with the magnetic field resulted in a suppressed plasma potential in the near-field plume, compared to the model without the magnetic field. Both the new models with and without the magnetic field effect showed very similar ion current densities along the centerline of the discharge channel, which agreed with experimental data. The magnetic field increased the plasma potential gradient from the channel exit to the near-field plume, decreasing the far-field plasma potential.

The assessment of the accuracy of the new model was performed by comparing the simulation results with experimental data. The new model with the magnetic field successfully reproduced the detailed structure in the near-field plume of the cathode by including the magnetic field effect. Although the new model with the magnetic field provides results more accurate than without the magnetic field, significant differences still remain between the simulations and measurements regarding the overall magnitude of the electron temperature, which implies that the electron energy equation needs to be improved.

The last objective of this dissertation was achieved by implementing a sputter model to calculate steady-state erosion rates. A semi-empirical fit for sputter yield data was found for Xe bombarding graphite. The sputter model was applied to estimate the erosion rates along the cathode keeper wall in the H6 thruster operating at the nominal conditions. The mean erosion rate of the graphite keeper wall was calculated to be 0.014 $\mu m/h$, which is on the same order of the erosion rate of the discharge channel walls in the magnetically-shielded H6 Hall thruster.

6.2 Contributions

The present study represents several contributions to the field of Hall thruster plasma plume modeling as follows:

1. Development of the new electron model. A new electron model that includes full 2-D axisymmetric magnetic field effects is developed. The new electron model has the ability to simulate electron transport across a complex magnetic field topology in the plume. The magnetic field in the plume includes a purely axial component along the cathode centerline axis, a purely radial component near the discharge channel exit of the thruster, and a magnetic field separatrix.

2. Improvement of the numerical methods. The numerical algorithm for solving the electron model has been improved by using a new continuous Galerkin finite element method. The discretized equation with the electron transport tensor coefficient is integrated using the Dunavant quadrature rules. Quadrature points up to 14^{th} order are implemented, which can be used to integrate higher order polynomial basis functions in the future.

3. Incorporation of a full plasma condition at the cathode boundary. The present work represents the first application of a more physically-accurate cathode condition including ion flows, which was calculated by OrCa2D [23].

4. Implementation of a sputter model. A sputter model to calculate the steady state erosion rate is implemented in a full-scale plume simulation. The present sputter model computes the flux and energy distributions of incident species to any solid surface, and a sputtering yield function based on an empirical curve fit of xenon-graphite data. The capability of the sputtering model is not limited to Hall thruster components, but can also be applied to other surfaces of spacecraft.

5. Estimation of the steady-state erosion rates of a LaB_6 keeper in the H6 Hall thruster at the nominal operating condition.

6.3 Recommendations for Future Work

In the process of completing this research, several areas have been identified that can lead to further improving the accuracy of Hall thruster plume simulation.

6.3.1 New Electron Energy Equation Solver

As shown by the comparisons of a simulated electron temperature with experimental data, the axial and radial profiles of the electron temperature were not able to reproduce the detailed shape of the measurements. In order to capture the detailed electron physics, the current energy equation must be improved.

The energy equation in MPIC is currently formulated as a Poisson equation where the forcing function also contains the electron temperature:

$$\nabla^2 T_e = f(T_e) \tag{6.1}$$

Instead of discretizing all terms, the forcing function is calculated using the value of T_e from the previous time step and estimating all derivatives using the least-squares method. A more mathematically correct way to solve this equation is to discretize all terms.

The electron model can be further improved by applying the continuous Galerkin finite element formulation to the governing equation without putting it in the Poisson equation form:

$$\frac{D}{Dt}\left(n_e\frac{3}{2}k_BT_e\right)=-p_e\nabla\cdot\mathbf{v}_e-\nabla\cdot\kappa_e\nabla T_e+\mathbf{J}_e\cdot\mathbf{E}-\sum\left[\frac{2m_e}{m_h}\bar{\nu}_{eh}n_e\frac{3}{2}k_B\left(T_e-T_h\right)\right]-\dot{N} \tag{6.2}$$

Solving this equation directly will more accurately describe the detailed electron physics. However, discretization and solving the system will be challenging. We recommend that the steady state should be assumed first. Once the steady-state form of this equation can be solved successfully, the unsteady energy conservation equation needs to be solved to capture time-dependent phenomena.

6.3.2 Higher Order Finite Element Solver

The current new model uses piecewise linear basis functions on triangular elements and thus has 2^{nd} order accuracy. Since the mesh size is small near the thruster and the cathode but is large at the far-field plume, having a higher order method can produce more accurate results. If the mesh size is too fine, because the same grids are used for the heavy species model, ensuring 20 or more particles per cell will require significant amounts of computational time. Therefore, using a higher-order finite element method will result in a more accurate solution.

6.3.3 Wall Boundary Conditions

In Hall thrusters, two types of walls exist: floating and grounded walls. The physics occurring at the boundary of the floating and grounded walls are different and thus should be treated appropriately.

6.3.4 Magnetic-Field-Aligned Mesh

In consideration of applied magnetic fields, the plasma potential contour showed numerical diffusion along the magnetic field line. This diffusion was probably caused by the large disparity of the transport coefficients parallel and perpendicular to the magnetic field. One way to approach this problem would be to use a computational mesh that is aligned with the applied magnetic field lines.

BIBLIOGRAPHY

BIBLIOGRAPHY

[1] F. R. Chang-Diaz. Plasma propulsion for space flight, 2007.

[2] D. M. Goebel and I. Katz. *Fundamentals of Electric Propulsion: Ion and Hall Thrusters*, volume 1. Wiley, 2008.

[3] D. M. Goebel, I. Katz, J. Ziemer, J. R. Brophy, J. E. Polk, and Johnson L. Electric propulsion research and development at jpl. In *41st AIAA Joint Propulsion Conference and Exhibit*, 2005.

[4] J. R. Brophy and et. al. The dawn ion propulsion system getting to launch. In *30th International Electric Propulsion Conference*, 2007.

[5] D. Y. Oh, D. E. Hastings, C. M. Marrese, J. M. Haas, and A. D. Gallimore. Modeling of stationary plasma thruster-100 thruster plumes and implications for satellite design. *Journal of Propulsion and Power*, 15(2), 1999.

[6] M. T. Domonkos, A. D. Gallimore, C. M. Marrese, and J. M. Haas. Very-near-field plume investigation of the anode layer thruster. *Journal of Propulsion and Power*, 16(1), 2000.

[7] T. D. Huismann. *Improving Hall thruster plume simulation through refined characterization of near-field plasma properties.* PhD thesis, University of Michigan Ann Arbor, 2011.

[8] J. M. Haas, R. R. Hofer, D. L. Brown, B. M. Reid, , and A. D. Gallimore. Design of the h6 hall thruster for high thrust/power investigation. In *54th JANNAF Propulsion Meeting*, 2007.

[9] D. M. Goebel, R. M. Watkins, and K. K. Jameson. Lab$_6$ hollow cathodes for ion and hall thrusters. *Journal of Propulsion and Power*, 23(3), 2007.

[10] I. D. Boyd. Review of hall thruster plume modeling. *Journal of Spacecraft and Rockets*, 38(3):381–387, 2001.

[11] I. D Boyd. Simulation of electric propulsion thrusters. Technical report, DTIC Document, 2011.

[12] D. Y. Oh and D. E. Hastings. Axisymmetric pic-dsmc simulations of spt plumes. In *24th International Electric Propulsion Conference*, 1996.

[13] K. Kannenberg. *Computational Methods for the Direct Simulation Monte Carlo Technique with Application to Plume Impingement*. PhD thesis, Cornell University, 1998.

[14] D.B. VanGilder, I.D. Boyd, and M. Keidar. Particle simulations of a hall thruster plume. *Journal of Spacecraft and Rockets*, 37(1):129–136, 2000.

[15] I. D. Boyd and R. A. Dressler. Far field modeling of the plasma plume of a hall thruster. *journal of applied physics*, 92(4):1764–1774, 2002.

[16] C. Cai. *Theoretical and numerical studies of plume flows in vacuum chambers*. PhD thesis, University of Michigan Ann Arbor, 2005.

[17] C. Niemela, L. Brieda, M. Nakles, J. Ekholm, and W. Hargus. Comparison of hall thruster plume expansion model with experimental data. In *42nd AIAA/ASME/SAE/ASEE Joint Propulsion Conference*, 2006.

[18] G. A. Bird. *Molecular gas dynamics and the direct simulation of gas flows*. Clarendon Press, 1994.

[19] C.K. Birdsall and A.B. Langdon. *Plasma Physics Via Computer Simulation*. Institute of Physics, 1991.

[20] J. M. Fife. *Hybrid-PIC Modeling and Electrostatic Probe Survey of Hall Thrusters*. PhD thesis, Massachusetts Institute of Technology, 1998.

[21] F. I. Parra, E. Ahedo, J. M. Fife, and M. Martinez-Sanchez. A two-dimensional hybrid model of the hall thruster discharge. *Journal of Applied Physics*, 100(2), 2006.

[22] R. R. Hofer, I. Katz, I. G. Mikellides, D. M. Goebel, and K. K. Jameson. Efficacy of electron mobility models in hybrid-pic hall thruster simulations. In *44th AIAA Joint Propulsion Conference and Exhibit*, 2008.

[23] I. G. Mikellides, I. Katz, D. M. Goebel, and J. E. Polk. Theoretical model of a hollow cathode plasma for the assessment of insert and keeper lifetimes. In *41 st AIAA/ASME/SAE/ASEE Joint Propulsion Conference & Exhibit*, pages 1–24, 2005.

[24] T. Huismann and I. D. Boyd. Simulation of hall thruster plumes in a vacuum chamber using a hybrid method. In *44th AIAA/ASME/SAE/ASEE Joint Propulsion Conference*, 2008.

[25] Y. Choi. *Modeling an Anode Layer Hall Thruster and Its Plume*. PhD thesis, University of Michigan Ann Arbor, 2008.

[26] P. N. Giuliano. *Modeling fundamental plasma transport and particle-induced emission in a simplified Test Cell*. PhD thesis, University of Michigan, Ann Arbor, MI, 2013.

[27] K. Hara. *Development of Grid-Based Direct Kinetic Method and Hybrid Kinetic-Continuum Modeling of Hall Thruster Discharge Plasmas.* PhD thesis, University of Michigan Ann Arbor, 2015.

[28] C. Galitzine. *On the Accuracy and Efficiency of the Direct Simulation Monte Carlo Method.* PhD thesis, University of Michigan, Ann Arbor, MI, 2014.

[29] I. D. Boyd and M. W. Crofton. Modeling the plasma plume of a hollow cathode. *Journal of Applied Physics*, 95(7):3285–3296, 2004.

[30] J. M Dawson. Particle simulation of plasmas. *Reviews of modern physics*, 55(2):403, 1983.

[31] S.A. Araki and R.E. Wirz. Cell-centered particle weighting algorithm for pic simulations in a non-uniform 2d axisymmetric mesh. *Journal of Computational Physics*, 272:218–226, 2014.

[32] G. A. Bird. Monte-carlo simulation in an engineering context. *Progress in Astronautics and Aeronautics*, 74:239–255, 1981.

[33] J. S. Miller, S. H. Pullins, D. J. Levandier, Y. Chiu, and R. A Dressler. Xenon charge exchange cross sections for electrostatic thruster models. *Journal of Applied Physics*, 91(3):984–991, 2002.

[34] R. R. Hofer, P. Y Peterson, and Gallimore A. D. Characterizing vacuum facility backpressure effects on the performance of a hall thruster. In *The 27th International Electric Propulsion Conference*, 2001.

[35] I. G. Mikellides, I. Katz, D. M. Goebel, and J. E. Polk. Hollow cathode theory and experiment. ii. a two-dimensional theoretical model of the emitter region. *Journal of applied physics*, 98(11):113303–113303, 2005.

[36] R. R. Hofer. *Development and characterization of high-efficiency, high-specific impulse xenon Hall thrusters.* PhD thesis, University of Michigan Ann Arbor, 2004.

[37] I. D. Boyd and J. T. Yim. Modeling of the near field plume of a hall thruster. *Journal of Applied Physics*, 95(9), 2004.

[38] E. Ahedo, P. Martnez-Cerezo, and M. Martnez-Sanchez. One-dimensional model of the plasma flow in a hall thruster. *Physics of Plasmas*, 8(6):3058–3068, 2001.

[39] M. Mitcher and C. H. Kruger. *Partially Ionized Gases.* Wiley, 1973.

[40] Robert Vichnevetsky. *Computer methods for partial differential equations.* Prentice-Hall, Inc., 1981.

[41] Y. Choi, M. Keidar, and I.D. Boyd. Particle simulation of plume flows from an anode-layer hall thruster. *Journal of Propulsion and Power*, 24(3), 2008.

[42] M. Choi and I. D. Boyd. Numerical simulation of the cathode plume of a hall thruster. In *50th AIAA/ASME/SAE/ASEE Joint Propulsion Conference*, 2014.

[43] K. K. Jameson. *Investigation of hollow cathode effects on total thruster efficiency in a 6 kW Hall thruster*. PhD thesis, University of California Los Angeles, 2008.

[44] D. A. Dunavant. High degree efficient symmetrical gaussian quadrature rules for the triangle. *International Journal of Numerical Methods in Engineering*, 21:1129–1148, 1985.

[45] W. H. Press, S. A. Teukolsky, W. T. Vetterling, and B. P. Flannery. *Numerical Recipes in C*. Cambridge University Press, 1992.

[46] H. C. Dragnea, Hara K., and I. D. Boyd. A fully 2d electron fluid model for hall thrusters. In *8th Annual Gaseous Electronics Conference/9th International Conference on Reactive Plasmas/33rd Symposium on Plasma Processing*, 2015.

[47] M. Sekerak, M. McDonald, R.R. Hofer, and A. Gallimore. Hall thruster plume measurements from high-speed dual langmuir probes with ion saturation reference. In *In Aerospace Conference, 2013 IEEE*, 2013.

[48] B. M. Reid. *The Influence of Neutral Flow Rate in the Operation of Hall Thrusters*. PhD thesis, The University of Michigan, Ann Arbor, MI, 2009.

[49] Michael Sean McDonald. *Electron transport in Hall thrusters*. PhD thesis, The University of Michigan, 2012.

[50] G. J. M. Hagelaar, J. Bareilles, L. Garrigues, and J. P. Bouef. Role of anomalous electron transport in a stationary plasma thruster simulation. 93(1):67–75, 2003.

[51] J. W. Koo and I. D. Boyd. Modeling of anomalous electron mobility in hall thrusters. *Physics of Plasmas*, 13:033501, 2006.

[52] Richard R. Hofer and et al. Wall sheath and electron mobility modeling in hybrid-pic hall thruster simulations. In *43rd AIAA/ASME/SAE/ASEE Joint Propulsion Conference and Exhibit*, 2007.

[53] I. G. Mikellides, I. Katz, R. R. Hofer, and D. M. Goebel. Hall-effect thruster simulations with 2-d electron transport and hydrodynamic ions. *IEPC Paper*, (09-114), 2009.

[54] Y. Yamamura and H. Tawara. Energy dependence of ion-induced sputtering yields from monatomic solids at normal incidence. 62(2):149–253, 1996.

[55] E. J. Pencil, T. Randolph, and D. H. Manzella. End-of-life stationary plasma thruster far-field plume characterization. In *32nd AIAA/ASME/SAE/ASEE Joint Propulsion Conference and Exhibit*, 1996.

[56] R. R. Hofer, B. A. Jorns, J. E. Polk, I. G. Mikellides, and J. S. Snyder. Wear test of a magnetically shielded hall thruster at 3000 seconds specific impulse. In *Presented at 33rd International Electric Propulsion Conference*, 2013.

[57] W. Eckstein, C. Garcia-Rosales, and J. Roth. Threshold energy for sputtering and its dependence on angle of incidence. *Nuclear Instruments and Methods in Physics Research B*, 83:95–109, 1993.

[58] J. R. Gruber. Low-energy sputter erosion of various materials in a t5 ion thruster. In *Presented at 27th International Electric Propulsion Conference*, 2001.

[59] R. P. Doerner, D. G. Whyte, and D. M. Goebel. Sputtering yield measurements during low energy xenon plasma bombardment. *Journal of Applied Physics*, 93(9):5816–5823, 2003.

[60] T. Kenmotsu, M. Wada, T. Hyakutake, T. Muramoto, and M. Nishida. Enhanced sputtering yields of carbon due to accumulation of low-energy xe ions. *Nuclear Instruments and Methods in Physics Research Section B: Beam Interactions with Materials and Atoms*, 267(8):1717–1720, 2009.

[61] D. Rosenberg and G. K. Wehner. Sputtering yields for low energy he^+-, kr^+-, and xe^+-ion bombardment. *Journal of Applied Physics*, 33(5):1842–1845, 1962.

[62] J.D Williams, M.M. Gardner, M. Johnson, and P.J. Wilbur. Xenon sputter yield measurements for ion thruster materials. *National Aeronautics and Space Administration, NASA/CR-2003-212306*, 2003.

[63] J.D. Williams, M.L. Johnson, and D.D. Williams. Differential sputtering behavior of pyrolytic graphite and carbon-carbon composite under xenon bombardment. In *40th AIAA/ASME/SAE/ASEE Joint Propulsion Conference*, 2004.

[64] R.D. Kolasinski, J.E. Polk, D. Goebel, and L.K. Johnson. Carbon sputtering yield measurements at grazing incidence. *Applied Surface Science*, 254(8):2506–2515, 2008.

[65] I. D. Mikellides, I. Katz, R. Hofer, and D. Goebel. Magnetic shielding of the channel walls in a hall plasma accelerator. *Physics of Plasmas*, 18:033501, 2011.

[66] R. R. Hofer, D. M. Goebel, I. G. Mikellides, and I. Katz. Design of a laboratory hall thruster with magnetically shielded channel walls, phase ii: Experiments. In *48th AIAA Joint Propulsion Conference, AIAA-2012-3789, Atlanta, GA, July*, 2012.

[67] D. M. Goebel, B. A. Jorns, R. R. Hofer, I. G. Mikellides, and I. Katz. Polepiece interactions with the plasma in a magnetically shielded hall thruster. In *AIAA/ASME/SAE/ASEE Joint Propulsion Conference*, 2014.

ABSTRACT

Improved Hall Thruster Plume Simulation by Including Magnetic Field Effects

by

Maria Choi

Chair: Iain D. Boyd

Hall-effect thrusters (HETs) are affordable and efficient electric propulsion devices for space exploration, with higher specific impulse than conventional chemical propulsion and higher thrust at a given power compared to ion thrusters. A detailed understanding and an accurate characterization of the physical processes occurring in HET plume are critical from both the thruster performance and spacecraft integration perspectives. Therefore, a new electron model that includes full 2-D axisymmetric magnetic field effects is developed and incorporated within the framework of a 2-D axisymmetric hybrid particle-fluid code. The governing equation of this new electron model consists of an electron mobility coefficient tensor. The new electron model can simulate any shape magnetic fields.

The accuracy of the model is first assessed using the method of manufactured solutions and a Hall thruster test case to confirm 2nd order accuracy. Then, the simulation results of a 6-kW laboratory Hall thruster are directly compared with experimental measurements to validate the model. By including the magnetic field, modeling of the anomalous electron mobility is required. Since the anomalous electron mobility is still not yet well-understood, it is modeled using the Bohm coefficient. A parametric study of the Bohm coefficient is performed to examine its effect on plasma properties. Due to the concave shape of magnetic field lines, the plasma potential

in the plume does not show a linear trend with the anomalous collision frequency. Comparisons with experimental data show that the new model with the magnetic field captures the detailed physics than without the magnetic field. In particular, the plasma potential profile agrees well with data by accurately capturing the strong negative gradient near the discharge channel exit of the thruster.

In order to extend the capability of the plume simulation, a sputter model is also implemented. The sputter model is applied to simulate the sputtering process of xenon propellants bombarding the surface of the "keeper" for the cathode, which can be an important failure mechanism in Hall thrusters. The steady-state mean erosion rate suggests that keeper erosion is as low as the erosion rate of the discharge channel walls in magnetically-shielded Hall thrusters.